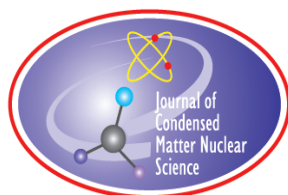


JOURNAL OF CONDENSED MATTER NUCLEAR SCIENCE

Experiments and Methods in Cold Fusion

**Proceedings of the first French Symposium
RNBE-2016 on Condensed Matter Nuclear
Science (Réactions Nucléaires à Basse Énergie),
March 18–20, 2016**

VOLUME 21, November 2016



JOURNAL OF CONDENSED MATTER NUCLEAR SCIENCE

Experiments and Methods in Cold Fusion

Editor-in-Chief

Jean-Paul Biberian
Marseille, France

Editorial Board

Peter Hagelstein
MIT, USA

Xing Zhong Li
Tsinghua University, China

Edmund Storms
KivaLabs, LLC, USA

George Miley
*Fusion Studies Laboratory,
University of Illinois, USA*

Michael McKubre
SRI International, USA

JOURNAL OF CONDENSED MATTER NUCLEAR SCIENCE

Volume 21, November 2016

© 2016 ISCMNS. All rights reserved. ISSN 2227-3123

This journal and the individual contributions contained in it are protected under copyright by ISCMNS and the following terms and conditions apply.

Electronic usage or storage of data

JCMNS is an open-access scientific journal and no special permissions or fees are required to download for personal non-commercial use or for teaching purposes in an educational institution.

All other uses including printing, copying, distribution require the written consent of ISCMNS.

Permission of the ISCMNS and payment of a fee are required for photocopying, including multiple or systematic copying, copying for advertising or promotional purposes, resale, and all forms of document delivery.

Permissions may be sought directly from ISCMNS, E-mail: CMNSEditor@iscmns.org. For further details you may also visit our web site: <http://www.iscmns.org/CMNS/>

Members of ISCMNS may reproduce the table of contents or prepare lists of articles for internal circulation within their institutions.

Orders, claims, author inquiries and journal inquiries

Please contact the Editor in Chief, CMNSEditor@iscmns.org or webmaster@iscmns.org



JOURNAL OF CONDENSED MATTER NUCLEAR SCIENCE

Volume 21

2016

CONTENTS

PREFACE

RESEARCH ARTICLES

- | | |
|--|----|
| A Tribute to Georges Lonchamppt
<i>Jean-Paul Biberian</i> | 1 |
| An Historical Experiment of Neutron Detection Near an Electrolytic Cell
<i>Michel Buxerolle and Jacques Kurkdjian</i> | 7 |
| Characterization of Energy Fluxes in LENR Reactors –Excess Heat, Coefficient of Performance and Conditions for Self-sustained Operation
<i>Jacques Ruer</i> | 13 |
| Proton Conductors: Nanometric Cavities, H ₂ Precipitates under Pressure, and Rydberg Matter Formation
<i>François de Guerville</i> | 26 |
| Relativity and Electron Deep Orbits of the Hydrogen Atom
<i>J.L. Paillet and A. Meulenberg</i> | 40 |
| The Dark side of Gravity and LENR
<i>Frederic Henry-Couannier</i> | 59 |
| Investigations of the Lugano HotCat Reactor
<i>Mathieu Valat, Alan Goldwater, Robert Greenyer, Robert Higgins and Ryan Hunt</i> | 81 |

Preface

It was with a profound sense of duty that our French Society for Condensed Matter Nuclear Science held its first “Symposium sur les Réactions Nucléaires à Basse Énergie” during the weekend of March 18–20, 2016, in Avignon, France. After 27 years of sustained research in the field of CMNS, this was the first time a conference was held for the French speaking community.

Numerous subjects were presented and discussed within a group of 50 attendees. It was a great opportunity for unreleased work done in France to finally follow the path of publication. This volume is composed of seven papers written in English in order to reach a wider audience.

Most notably, one of these research programs was done in 1989 by researchers affiliated to the French Nuclear Agency (CEA), before research was officially forbidden, never pursued again, officially at least. It bears important findings which we hope will trigger insights from the community.

Some major theoretical works on relevant and related subjects are also presented in this volume, alongside fundamental engineering analysis, aiming at a better understanding of claimed figures within our field of research.

Some new young and talented scientists have also presented their findings on this occasion regarding proton conductors and fundamental interpretation of hydride behavior.

I would like to acknowledge Jean-Paul Biberian and his wife Rachel who helped me in organizing and facilitating the venue of this conference. Anaïs Kedikian provided tremendous efforts since then. She has recorded, cut, uploaded and organized the entire conference in a playlist ^a on our YouTube channel for everyone to watch. Additional work is being processed to provide new material for the French community to spread curiosity and public interest in CMNS. Nicolas Armanet and Michel Bonnard provided inspiration and valuable advices at the very beginning of this journey to make this conference successful. Finally, I want to thank my friend, Joris van der Schot, who helped me running this humble organization behind-the-scenes.

Taking advantage of this first editorial, my journey in the CMNS so far has been fruitful because it has introduced me to some of the most brilliant human beings I have ever met. People who bear the loss of their scientific reputations, and strong opposition, are going forward to meet the challenges we face for the sake of humankind’s future. Together we will prevail! Last but not least, I want to express my profound thanks and admiration to Jed Rothwell who is dedicating so much effort in reviews, translations, verifications and publications of the community’s work on the Internet and within the JCMNS.

Happy reading :)

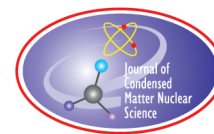
Sincerely,

Mathieu Valat

(President of the French Society on Condensed Matter Nuclear Science)

November 2016

^a<https://goo.gl/sio5o7>



Research Article

A Tribute to Georges Lonchampt

Jean-Paul Biberian*

Aix-Marseille University, France

Abstract

Georges Lonchampt was one of the few French researchers who, from day one, worked on Cold Fusion. He started performing his own experiments, and later worked with Martin Fleischmann and Stanley Pons. He successfully reproduced the two scientists' original experiment, and was the only one able to successfully replicate the boil-off experiment.

© 2016 ISCMNS. All rights reserved. ISSN 2227-3123

Keywords: Boil-off, Cold fusion, Electrolysis, Lonchampt, Solid state electrolyte

1. Introduction

Georges Lonchampt was one of the very few scientists involved in Cold Fusion research from the very beginning. Having made a career as an electrochemist engineer, he began trying to replicate Pons and Fleischmann's experiment as soon as he heard of their discovery. After initial difficulties reproducing their findings, Lonchampt contacted Pons and Fleischmann for help. The two researchers, who were located in southern France's Sophia Antipolis near Nice, gave Lonchampt their support and two of their ICARUS 2 cells. With a lot of tenacity Lonchampt managed to reproduce Pons and Fleischmann's original work. He also applied himself to other experiments, such as the Patterson beads and proton conductors.

I was lucky enough to work with Georges Lonchampt for over five years. He taught me a lot during that time.

2. Lonchampt Background

Lonchampt was born on April 2, 1935 in Bourg-en-Bresse near Switzerland. He studied in Gex, then Nantua and finally in Grenoble where he graduated as an electrochemical engineer. Later he obtained another degree in Nuclear Engineering.

During his Military Service, he spent 18 months at the French Atomic Energy Center in Miramas in the South of France. He worked on the isotopic separation of lithium-6 from natural lithium for military applications.

*E-mail: jpbiberian@yahoo.fr.

2.1. Isotopic separation of lithium

In 1962, Lonchampt joined the French Atomic Energy Center in Grenoble where he continued working on the isotopic separation of lithium-6. Li-6 is only 7% of natural lithium, whereas Li-7 is 93%. Li-6 is an important material for the fabrication of the H-bomb that France wanted to produce at that time. He was very successful that he managed to go from 24 electrolyzers to only three! He lowered the cost of the production of Li-6 by two orders of magnitude. This achievement was the beginning of his fame in the nuclear industry.

2.2. Isotopic separation of uranium

Following his success with lithium enrichment, Lonchampt was given the task of separating uranium-235 from natural uranium. The new electrochemical isotopic separation was a challenge, and at first was considered as non-proliferating. He worked from 1973 till 1985, and was very successful. He had to build a 30-meter high tower to locate his electrolyzers. Even though his pilot factory was successful, the people in Miramas were not able to reproduce his method. The project was abandoned in favor of the laser enrichment method, which actually never worked due to materials issues.

It is at that time that he hired Professor Lucien Bonnetain as an advisor, and kept excellent relationship with him until his death.

2.3. Lithium polymer batteries

As Lonchampt was an excellent electrochemist, he was then given the task of testing the new lithium-polymer battery developed by the French scientist Michel Armand. A major French corporation, Bolloré, was getting ready to commercialize this type of battery. Lonchampt collaborated with Bolloré in R&D. Today, Bolloré has commercialized the “Blue car”, a system of shared electric cars available in Paris, using the lithium-polymer batteries. In this work Lonchampt learned how to produce polymer proton conductors for the batteries. He later applied that technique to Cold Fusion.

3. Cold Fusion

Following the announcement of the discovery of Cold Fusion by Pons and Fleischmann, Lonchampt started immediately experimenting with palladium. However, Jean Teillac, the head of the French Atomic Energy Center, asked that all Cold Fusion research within the organization be halted in France. Fortunately, the director of the Grenoble Institute of Technology invited Lonchampt to set-up his own laboratory within the institute so he could continue his research. Lonchampt began juggling daytime work on batteries at the French Atomic Center and night work on Cold Fusion at the institute.

3.1. ICARUS 2 type experiments

Lonchampt's initial experiments did not show the desired results. One of the reasons was that the palladium electrodes were too large. When Pons and Fleischmann moved to France, Lonchampt contacted them, and began collaborating with them. They gave him two of their own electrolytic cells (ICARUS 2 type), and he subsequently observed excess heat, although not as much as Pons and Fleischmann had. Figure 1 shows a picture of one of the cells during electrolysis. He used a 12 mm × 2 mm palladium electrode and a platinum wire anode with 0.1 M LiOD.



Figure 1. A photograph of an ICARUS 2 cell showing the cathode and anode and the water mixing by the hydrogen and oxygen gas bubbles.

3.2. Solid-state electrolytes

In 1995, while working at the Lawrence Berkeley Laboratory in California, I sent a manuscript of my preliminary results with solid-state electrolytes to the *Journal Physics Letters A*. At that time, Jean-Pierre Vigier was the editor-in-chief, and he rightly sent my work to Lonchampt for review. As he was dubious about my results, he asked me to come to his laboratory to redo the experiment there with better instrumentation. I brought my own crude calorimeter that I had built in Berkeley, but Lonchampt did not find it satisfactory and built a much better one. This helped us to prove that there was indeed excess heat.

Figure 2 shows a schematic of the improved calorimeter. Lonchampt had a brilliant idea of measuring the power production. In this design the samples were heated by a cylindrical alumina tube heated with a tungsten wire. The heat flow was calculated by the electrical resistivity change of the tungsten wire. As the electrical resistance changes with temperature, at constant heating power, if excess heat is produced, that will change the electrical resistivity. The graph in Fig. 3 shows the temperature rise when a high voltage is applied through the solid-state electrolyte, showing excess heat and heat after death.

Since there is heat after death, instead of using a DC voltage applied to the solid-state electrolyte, we used one-second pulses every minute. This improved the Coefficient of Performance greatly. This work was published at the ICCF5 conference in Monaco. Even though Lonchampt was heavily involved in this work, he did not sign the first paper, and I was the sole author [1]. Later we published more results together at the ICCF7 conference [2]

3.3. Patterson cells

The discovery by James Patterson of a new way of producing excess heat with plastic or glass beads one millimeter in diameter covered with triple layers of nickel-palladium and nickel, greatly interested Lonchampt. He bought a demonstration kit from Patterson, including the test cells, but also a small quantity of beads. In order to save the

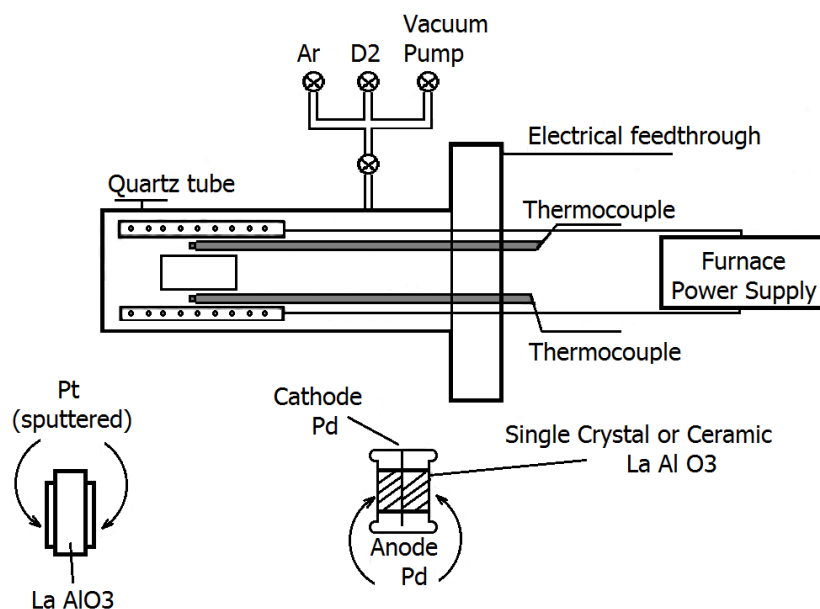


Figure 2. Schematic of the experimental set-up with two solid state electrolytes symmetrically positioned.

Patterson beads for future experiments, he had his own beads manufactured by Mecaprotec, a company located in Toulouse, France, that had a technique similar to the one of Patterson. The results of the experiments were published at ICCF7 [3].

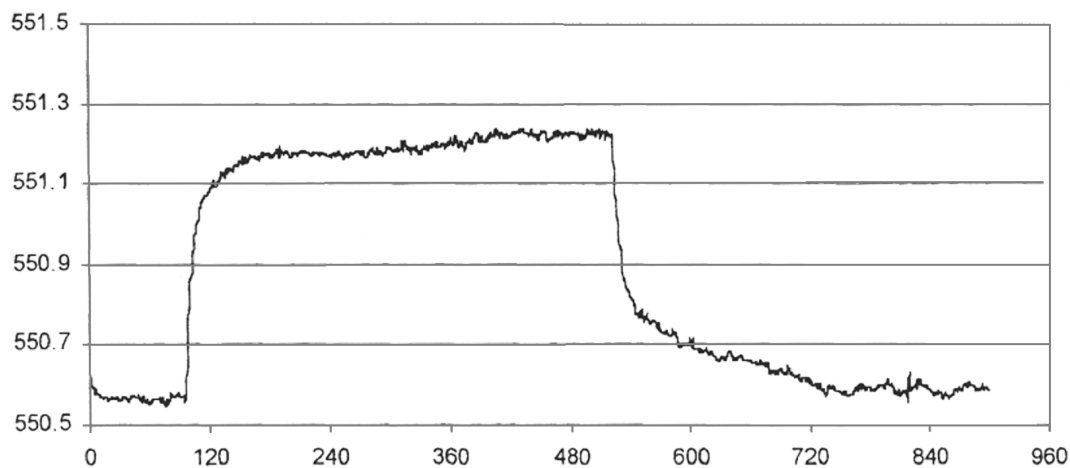


Figure 3. Temperature rise (in °C) versus time (in min) showing heat after death when excitation stopped.

Figure 4 shows the experimental results of the excess heat vs the input power. The results were not as robust as Patterson's who had large excess heat.

3.4. Boil-off experiments

Following the announcement by Fleischman and Pons of excess heat, once the electrochemical cell is not refilled and the cell is let to boil-off until it gets dry [4], Lonchampt decided to replicate the experiment. He was successful, and Table 1 shows the actual results presented at the ICCF6 conference [5]

3.5. Loading palladium with a solid-state electrolyte

Lonchampt was very concerned with the over-potential that, in electrochemistry, is equivalent to a gas pressure. The more the over-potential is high the higher the equivalent pressure of deuterium if it was in a gas phase environment. We tried a new set of experiments in deuterium gas where a palladium foil is used as a cathode and two palladium foils

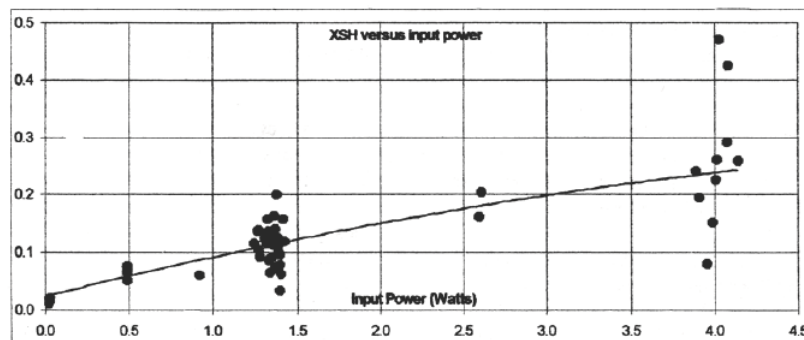


Figure 4. Excess heat (W) vs. input power (W).

Table 1. Excess heat after boil-off experiment.

Experiment	Date	Electrolyte volume (cm ³)	Enthalpy input (electrolysis) (J)	Enthalpy losses (to bath water) (J)	Available enthalpy (J)	Enthalpy used for total vaporisation (J)	Excess heat (J)	Mean relative excess heat (%)	Relative excess heat during grand final (%)
P1 Pd 1st sample	Jan. 30, 1996	84	419 100	254 700	156 876	181 499	24 623	16	153
P1 Pt	Calibration March 18, 1996	85.5	425 700	240 600	185 100	184 740	360	−0.2	No burst
N Pd 1st sample	Sept. 3, 1996	80	318 700	151 000	167 700	172 856	5156	3	IS
P3 Pd 1st sample	Sept. 14, 1996	74	221 200	72 190	149 010	159 892	10 882	7	36
n Pd 2nd sample	Sept. 30, 1996	72	308 600	178 700	129 900	155 570	25 670	20	97
P3 Pd 2nd sample	Oct. 2, 1996	78	290 700	132 800	157 900	168 535	10 635	7	29

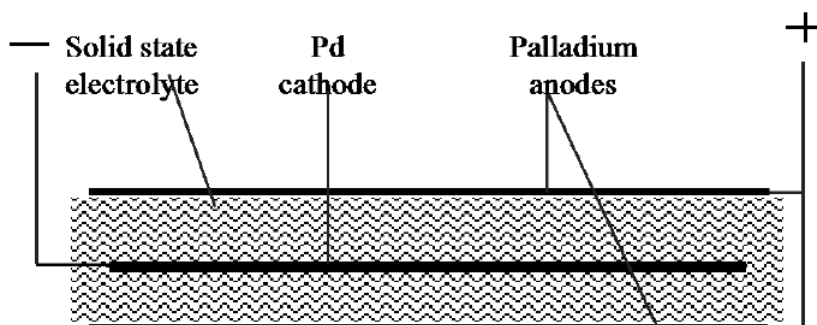


Figure 5. Experimental set-up.

as anodes. Between them an organic proton conductor is located, as shown in Fig 5. The electrolyte is Polyoxyethylene (POE) and deuterated phosphoric acid, similar to the electrolyte developed by Armand for the lithium–polymer batteries.

By this time, Lonchampt had retired, and I was back at my laboratory in Marseilles. Lonchampt transformed his garage into a high-functioning laboratory where he prepared the electrolyte layers and regularly mailed them to me. I did the calorimetry, and sent him the data by email every day. We used to talk on the phone for hours discussing the details. Unfortunately, in spite of all our attempts, we did not succeed in observing anomalous excess heat [6]

4. Conclusion

I had the great honor of working with Georges Lonchampt for over than five years. This was a very productive period of my life. Lonchampt was a very kind person, with a lot of common sense. He applied his great engineering skills to the field of Cold Fusion and made major contributions to the field. In particular, he was the only one who reproduced the boil-off experiment.

I am very sad to have lost such a good friend.

References

- [1] J.-P. Biberian, Excess heat measurement in LaAlO_3 doped with deuterium, *Proc. fifth Int Conf. on Cold Fusion*, 1995, pp. 49–56.
- [2] J.-P. Biberian G. Lonchampt, L. Bonnetain and J. Delepine, Electrolysis of LaAlO_3 single crystals and ceramics in a deuteriated atmosphere, *The Seventh Int Conf. on Cold Fusion*, Vancouver, Canada, ENECO Inc., Salt Lake City, UT, 1998, pp. 27–33.
- [3] G. Lonchampt, J.-P. Biberian, L. Bonnetain and J. Delepine, Excess heat measurement with Patterson type cels, in *The Seventh Int. Conf. on Cold Fusion*, Vancouver, Canada, ENECO Inc., Salt Lake City, UT, 1998, pp. 6–9.
- [4] M. Fleischman and S. Pons, Calorimetry of the Pd– D_2O system: from simplicity via complications to simplicity, *Phys. Lett. A* **176**(1993)118–129.
- [5] G. Lonchampt, L. Bonnetain and P. Hicter, Reproduction of Fleischmann and Pons experiments, in *Sixth Int. Conf. on Cold Fusion, Progress in New Hydrogen Energy*, Lake Toya, Hokkaido, Japan, 1996, pp. 113–120.
- [6] J.-P. Biberian and G. Lonchampt, Deuterium gas loading of palaldium using a solid-state electrolyte, *The Ninth Int Conf on Cold Fusion*, Tsinghua University, Beijing, China, 2002, pp. 17–21.

Research Article

An Historical Experiment of Neutron Detection Near an Electrolytic Cell

Michel Buxerolle *

9 rue du docteur Dargelos, 13100 Aix en Provence, France

Jacques Kurkdjian

25 rue de la Chapelle, Quartier Saint Roch, 84120 Pertuis, France

Abstract

An electrolysis experiment performed in April 1989, with a hollow palladium cathode in heavy water showed neutrons production. The results were sufficiently reliable to exclude any experimental error. Unfortunately a similar experiment has never been attempted since then. The presence of neutrons is the signature of nuclear reactions.

© 2016 ISCMNS. All rights reserved. ISSN 2227-3123

Keywords: Chain, Deuterium, Electrolysis, Neutron, Palladium, Reaction

1. Introduction

At the time of the March 23 announcement by Fleischmann and Pons [1] of possible nuclear fusion reactions at room temperature inside a palladium cathode, we were working at the Centre d'Etudes Nucleaires de Cadarache in France. Our laboratory was devoted to neutron dosimetry and we had access to suitable equipment for neutron measurements. For us, the easiest method to check the validity of Cold Fusion was to proceed with neutron measurement near an electrolytic experiment. We had several old palladium–silver tubes used to produce ultra pure deuterium gas for an ion accelerator. The palladium–silver tubes were 10 cm long, 2 mm outer diameter, 0.2 mm thick walls and closed at one end. We succeeded in detecting neutrons. In spite of this success, our work was quickly stopped by the head of the French Atomic Energy Commission, and no further experiments were possible.

2. Experimental Details

The electrolytic cell included the palladium-silver cathode (with only 5 cm of the tube immersed in the electrolyte), and a platinum coated anode located around the cathode. The electrolyte was D₂O with NaF. The neutron detector

*Corresponding author. E-mail: mich.bux@wanadoo.fr.

located 43 cm from the cathode was a helium-3 type at the center of a polyethylene sphere, 20 cm in diameter. The sensitivity was $0.43 \text{ neutron/cm}^2$, with an uncertainty of $\pm 5\%$. Calibrations were performed with 2.5 MeV neutrons, from a Van de Graaff accelerator. Before each experiment, the calibration of the measurement equipment was verified by means of a reference americium–beryllium source.

Because we lacked a valid hypothesis, we supposed that the neutron emission was in the form of very short bursts. In that case, the best method was to proceed by integration with activation detectors. Several detectors were placed near the electrolysis cell: copper, indium, sulfur and magnesium. The sphere was positioned near a section of the electrolysis cell. Measurements were accumulated for ten minutes before being recorded. To test the counter stability, the polyethylene sphere received a weak and stable high energy neutron flux, originating from two strong sources, americium–beryllium and californium-252 located inside a polythene container. With this type of protection, a very small part of the initial neutron spectrum could escape at high energy. Therefore, the background count was 0.22 pulse/s.

During the first two experiments, we did not measure any increase in the neutron flux with the helium-3 detector. The only observation was a bending of the cathode and cracks on its surface. Since only half of the palladium tube was immersed in the electrolyte, this probably provoked stress inside the section of the palladium loaded with deuterium.

The third experiment was different. Before electrolysis, the third tube was partially loaded with deuterium by placing it in an atmosphere of deuterium at about 2 bar for several days. After some trials of electrolysis current, the amperage was set to 10 mA/cm^2 overnight. During this time (about 16 h), the counts on the helium-3 detector were stable at the background level. Then, the counts showed a surprising and roughly linear increase, for about 5 h, up to a level four times larger than the background level. Unfortunately, the experiment stopped because of an electric power failure in the laboratory due to a thunderstorm. About 30 min later, with the return of the electric power, the counts were about at the same level, but they decreased rapidly to return to the background level in less than 2 h (Fig. 1).

The measurement apparatus seemed to work properly, with background level counts before and after the increase in counts. There was no possibility of parasitic neutrons sources.

Consequently, we conclude that an unexplained neutron emission was certainly observed. The largest net count was: 0.7 pulse/s. The estimate total neutron emission was: $3.8 \times 10^4 \text{ neutron/s}$ with an uncertainty of about 20%. We note that, in the initial paper of Fleischmann and Pons ([1], p. 306), the neutron emission is nearly the same: $4 \times 10^4 \text{ neutron/s}$ with a cathode 10 cm long and 4 mm in diameter.

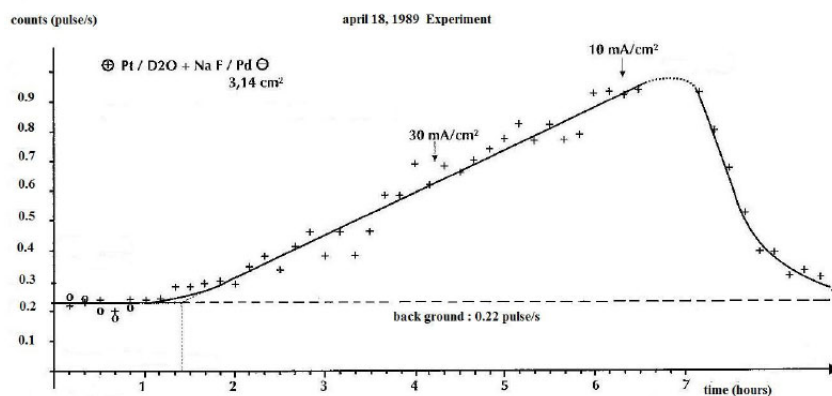


Figure 1. Neutron pulse counts (pulse/s) versus time (h).

No radioactivity was measured with the activation detectors. In order to perform new measurements, but with a reduced background, the experiment was transferred to an underground room. Nevertheless, the sensitivity to parasitic electromagnetic radiation was negligible, for the same equivalent dose, the ratio of neutron counts/gamma counts was greater than 10^4 , tested with ^{60}Co and ^{226}Ra gamma sources. Then again, the arrival of the thunderstorm, coming with a barometric depression, induced a radon release, perceptible on atmospheric controls. The possibility that high energy gammas from ^{214}Bi , daughter of ^{222}Rn , could generate photo-neutrons in the heavy water jar was considered. A similar measurement apparatus was used, in parallel, with an identical Bonner sphere near a 20 liter heavy water tank. No difference of background has been observed in the underground room. Despite numerous attempts, behavior similar to the one reported above was never observed.

If a single experiment was insufficient to understand the observed phenomena, the presence of neutrons appeared real and certified the presence of nuclear reactions.

Below, this experiment is referred to as the “April 18 experiment”

3. Discussion

Later on Biberian utilized a tube similar to the one used for the April 18 experiment in open cell electrolytic experiments. At the end of one experiment, the Dewar type Pyrex cell exploded [7]. The cell enclosed a very small quantity of deuterium and oxygen gas, not enough to cause a chemical explosion of that magnitude. Despite this dramatic event, the amount of energy was not sufficient to induce apparent damage to the palladium tube. Probably this energy was released in a very short burst leading to a production of large power and a shock wave. Incidentally, we note that the tubes have a disturbing tendency to induce nonchemical explosions [9]. More recently, the same type of palladium tube was used during another experiment and 3 W of excess energy was detected for several days [10].

Undoubtedly, the energy released is due to the same phenomenon which can evolve in a very short period of time and even become explosive, or over a time more or less long, allowing excess energy measurements. This phenomenon has characteristics similar to “criticality” in fissile materials, which hints at the possibility it might develop chain reactions under special conditions.

Therefore, we can now understand why the April 18 experiment was not successful in the underground room where the external flux of high energy neutrons was absent.

4. Conclusion

The hypothesis of chain nuclear reactions sustained by protons seems in good agreement with the data resulting from cold nuclear fusion experiments. But this is only a hypothesis, valid as long as an inconsistency is allowed. The direct evidence of cold nuclear fusion requires indubitable and reproducible experiments. Maybe the chain nuclear reactions model is capable of giving a research clue, if however the hypothesis agrees with the reality.

Our interest is to demonstrate unlimited energy resources since the deuterium is extracted from water, no radiation apart some neutrons, and no radioactive product apart from tritium in small quantity.

The development of a line of “cold nuclear fusion reactors” would produce large quantities of helium-4. It would be also possible to recover quantities of helium-3, mainly from tritium disintegration. This element is considered as essential, in the future, for the “hot fusion” reactors.

Appendix A. Neutron Detection

The neutron detector was a Bonner polythene sphere, 8 in. in diameter, with a small size helium-3 detector at its center. Before each experiment, the measurement apparatus was verified by means of a low emission neutron source (7 mCi

Am–Be). Thus, all the equipment was operational for the measurement (Fig. 1). The detector sensitivity was $0.43 \text{ pulse/n.cm}^{-2} \pm 5\%$ for 2.45 MeV neutron energy (Van de Graaff accelerator calibration). Figure 2 shows a view of the experimental environment.

Measurements were proceeded by a sequence of 10 min periods by a very short time to data transfer. To verify the apparatus stability, a high background was chosen (about 120 pulses in 10 min) by placing the experiment near a container with two strong sources, Am–Be and ^{252}Cf , behind a biological protection (polythene + boron) (Fig. 2).

Several trials confirmed the background stability, except in one case. Before electrolysis, the tube used was partially charged by pressure of about 2 bar during several days. After some trials of electrolysis current (variation $40\text{--}10 \text{ mA/cm}^2$) the amperage was set to 10 mA/cm^2 for a night. During this time, about 16 h, the counts of Bonner sphere were the stable background. Then, the counts showed (Fig. 1) a surprising and roughly linear increasing during about 5 h, up to a level four times greater than background. Unfortunately, the experiment stopped because of a shutdown of the electric power in the laboratory, due to a thunder storm. About 30 min later, with the return of electric power, the counts were about at the same level, but they decreased rapidly to return to the background level in less than 2 h. Taking into account the maximum at 0.92 pulse/s , the net count was $0.7 \pm 0.14 \text{ pulse/s}$. The center of the sphere was 43 cm far from the cathode and the estimation of neutron emission was: $Q = 3.8 \times 10^4 \pm 0.8 \times 10^4 \text{ neutron/s}$ in 4π steradian (about $\pm 20\%$, uncertainty at 3σ). In the initial paper of Fleischmann and Pons (p. 306) the neutron emission is $4 \times 10^4 \text{ neutron/s}$ with a palladium cathode: length 10 cm, diameter 4 mm.

The measurement apparatus seems quite right: stable background before and after the counts evolution, same counts before and after the electric shutdown, no possibility of parasitic neutrons sources in proximity to the laboratory.



Figure 2. Experimental set-up showing a neutron dosimeter calibration. During the 18 April experiment, the neutron sources were located inside the black cubic container about 2 m from the electrolysis cell.

Despite several trials, this experiment is unique and a single experiment is insufficient to understand the observed phenomena.

Appendix B. A Tentative Theoretical Explanation

In conclusion, the presence of neutrons, pointing out nuclear reactions, appears real. The high energy neutrons, going out of the external source container near the experiment, seem to originate according to the hypothesis developed below.

High energy neutrons can move deuterons in the palladium lattice and so create $D + D$ reactions with a proton emission. According to a process described by the Nobel laureate Julian Schwinger a proton can generate a: $p + d \rightarrow {}^3\text{He} + \text{gamma}$ (5.48 MeV) reaction. The ${}^3\text{He}$ may undergo a secondary reaction with another deuteron in the lattice, yielding ${}^5\text{Li}^*$ which is unstable against disintegration into a proton and an alpha particle. Finally, a three body: $p + d + d$ reaction occurs, hypothesis considered by Yamaguchi and Nishioka (*Proc. ICCF3*, Nagoya, 1992). With this process, the proton is not consumed and chain reactions can occur. In the experiments described here, no 5.48 MeV were observed and the photon radiation was negligible. In the $p + D$ reaction all the elements have even parity and with no change of parity electric dipole radiation is forbidden, other effects might intervene but very weakly.

With the lack of 5.48 MeV gamma, the mass energy balance is about 24 MeV per cycle, the same energy for a direct fusion $D + D$. The cross section of the initial $p + D$ is very low but presumably is increased by channeling, where the palladium lattice acts as many particle guides. With the hypothesis of chain reactions, it is necessary to have additional D (d , p) T reactions to implement the growth. The conditions are thus quite similar to the growth in a critical fissile medium with an effective multiplication factor k . This factor k is bound to the charge ratio D/Pd and to the “geometric buckling” of the palladium sample. When k is greater than 1, the growth of chain reactions is exponential. If k is just greater than 1, the growth is approximatively linear as in our experiment. If k is much greater than 1, the growth becomes explosive. This may explain why with a tube similar to the one used for our experiment, in an open cell electrolytic experiment by Biberian, the Dewar type Pyrex cell exploded.

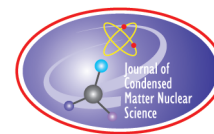
The beginning of chain reactions requires a primary proton, and external radiation is necessary: high energy neutrons in our experiment – high energy gamma ($E > 2.23$ MeV) which divides a deuteron in proton and neutron – cosmic meson, which generate a $D + D$ reaction (Sakharov fusion). Added to the development of criticality conditions (charge ratio, shape and dimensions of the palladium sample), this external intervention can explain why positive experiments are uncertain and not even possible in low background laboratories.

An electrolytic experiment in the presence of a strong source of high energy neutrons can validate the hypothesis of chain reactions, but if the result is positive the interest is only historical, just to say Fleischmann and Pons were right. The use of palladium deuterium system offers many difficulties: palladium is expensive, deuterium is a regulated material, neutron radiation and tritium are produced, and there is a potential risk of explosion. The experiments conducted with hydride of metals such as nickel or tungsten are more promising. Energy excess is observed presumably by nuclear transmutation after proton capture. The palladium is not able, by proton capture, to give transmutations to silver isotopes because of wave function parity.

References

- [1] M. Fleischmann and S. Pons, Electrochemically induced nuclear fusion of deuterium, *J. Electroanalytical Chem.* **261** (1989) 301–308.
- [2] P.H. Hagelstein, M.C.H. McKubre, D.J. Nagel, T.A. Chubb and R.J. Hekman, New physical effects in metal deuterides- condensed matter nuclear science, *Proc Eleventh Int Conf Cold Fusion*, J.P. Biberian (Ed.), World Scientific, New York, 2006.
- [3] E.Storms. Review of the “ColdFusion” effect. <http://scientificexploration.org/jse/articles/storms/7>
- [4] J. Schwinger, Cold fusion theory: a brief history of mine, *Infinite Energy Magazine*.

- <http://www.mv.com/ipusers/zeropoint/IEHTML/FEATURE/FEATR/schwinger04.html>,
<http://www.geocities.com/CapeCanaveral/Lab/4520/theory.htm>
- [5] E. Yamaguchi and T. Nishioka Direct evidence for nuclear reactions in deuterated palladium, *Proc. ICCF3*, Nagoya, 1992.
 - [6] Y. Isobe, S. Unerne, K. Yabuta, H. Mori, T. Omote, S. Ueda, K. Ochiai, H. Miyamaru, and A. Takahashi, Search for coherent deuteron fusion by beam and electrolysis experiments, *In 8th Int. Conf. on Cold Fusion*, 2000, Lerici (La Spezia), Italy: Italian Physical Society, Bologna, Italy.
 - [7] J.P. Biberian in [8], A look at experiments.
 - [8] <http://www.LENR-CANR.org>
 - [9] Zhang Xinwei, Zhang Wu-Shou, Wang Dalun, Chen Suhe, Fu Ybei, Fan Daxio and Chen Wenjiang, On the explosion in a deuterium/palladium electrolytic system *Proc. Int. Conf. Cold Fusion*, Nagoya, Japan, 1992, uploaded to [6] in June 2006.
 - [10] J.P. Biberian and N. Armanet, Excess heat during diffusion of deuterium through palladium, *ICCF 13*, Sochi, 2007.
 - [11] Cold Fusion Research A report of the Energy Research Advisory Board of the United States. Department of Energy November 1989 Internet Edition Prepared by National Capital Area Skeptics (NCAS), 1999. <http://www.ncas.org/erab/>
 - [12] M. Fleischmann, S. Pons, M.W. Anderson, Lian Jun Li and M. Hawkins, *J. Electroanal. Chem.* **287** (1990) 293–348.
 - [13] Y. Arata and Y.C Zhang, *Proc. ICCF 12*, Yokoama, A. Takahashi, Y. Iwamura and K. Ota (Eds.), World Scientific, Singapore, 2006, pp. 44–54 (and [6]).
 - [14] M. Fleischmann and S. Pons, Calorimetry of the Pd–D₂O system: from simplicity via complications to simplicity, *Phys Lett. A* **176** (1993) 118–129.



Research Article

Characterization of Energy Fluxes in LENR Reactors –Excess Heat, Coefficient of Performance and Conditions for Self-sustained Operation

Jacques Ruer*

Abstract

LENR reactors are considered as units that operate at a temperature above ambient and need an excitation provided by a supply powered by electricity. Different modes of operation are described following the characteristics of the heat and energy balance. LENR reactors may be characterized by different parameters, Coefficient of Performance (COP) or Energy Amplification factor (A). The thermal insulation plays an important role. LENR reactors that require external heating in small units may become self-sustained for large sizes. The production of electricity involves the coupling with a thermal machine. The system is able to export power if the COP and the temperature are high enough.

© 2016 ISCMNS. All rights reserved. ISSN 2227-3123

Keywords: Carnot, COP, Ericsson, Excess heat, Gain, Insulation, ORC, Self-sustained, Stirling, Thermal engine

1. Introduction

In the present paper, we consider LENR systems producing heat in such quantities that it is possible to transform the heat into mechanical energy thanks to a thermodynamic engine, and into electricity via a generator.

The LENR reactor consumes some energy to sustain its operation, but if the generator produces a larger amount of power, an excess of electricity is available for export. The ultimate goal of LENR systems will be to produce electrical energy. The purpose of this paper is to clarify the parameters that are required to make such an operation possible. Figure 1 shows the sketch of an LENR generator incorporating a reactor and a thermal engine.

2. Hypotheses

The LENR reactor generates an energy output. We suppose here that this energy is in the form of heat, delivered at a temperature T_r above the ambient environment one T_a . The LENR reactor requires some energy input to trigger and control the operation. We assume that this energy input is in the form of electricity. The electrical energy consumed as input is called “excitation”. Following the type of reactor, the excitation may include DC electricity for electrolysis, high voltage pulses, electrical resistance heating, etc. [1–6].

*E-mail: jsr.ruer@orange.fr.

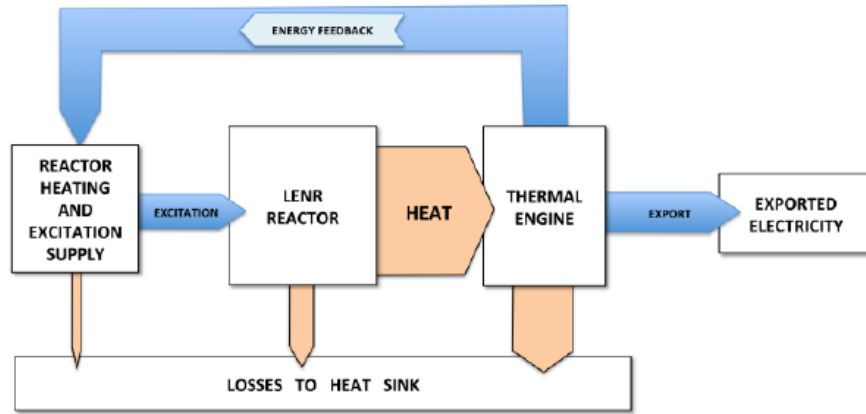


Figure 1. Sketch of an LENR generator incorporating a reactor and a thermal engine.

The reactor is a closed system in thermodynamic terms. This means that no matter enters nor leaves the reactor during operation. For example, if the reactor is an electrolysis cell, the gases are recombined within the reactor assembly.

The reactor is *thermally insulated* in order to control the losses and recover most of the heat for a useful purpose. The thermal insulation is an important feature of the system being considered. If we want to detect excess heat and harvest usable energy, the heat losses must be minimized. Figure 2 shows schematic of a simple LENR reactor.

3. Calibration

The efficiency of the insulation must be first determined via a calibration procedure. For that purpose, the reactor is brought to its working temperature by an auxiliary internal heating source. During the calibration, measures are taken to make sure that no LENR can take place. Figure 3 summarizes the calibration process. The reactor is heated by an electrical input E_1 . All that energy goes away as thermal loss via the thermal insulation. Several measures can be repeated for various input power steps. This makes it possible to draw the relationship between the reactor temperature T_r and the heat loss, equal to the input H_1 . The relationship is valid for a given ambient temperature T_a . This one must be kept constant during the whole test campaign, or the measures have to be repeated for the different values of T_a that may be encountered.

The measure of each point of the curve presupposes that the thermal equilibrium is reached after a change of the input power or the outside temperature. Otherwise the transient heat flows introduce errors. Calibration may therefore be a time consuming task, especially for large reactors.

4. Heated Reactor – MODE 1 of Operation

In some cases, the reactor works at a high temperature, and thermal losses must be compensated. If the LENR energy generation is not sufficient, additional heating must be provided to maintain the operation temperature (Fig. 4).

The corresponding energy flowchart is shown in Fig. 5. This first example gives the opportunity to introduce some definitions. The LENR reactor is supplied by two electrical inputs:

- E_e : Excitation (depending on the reactor type),

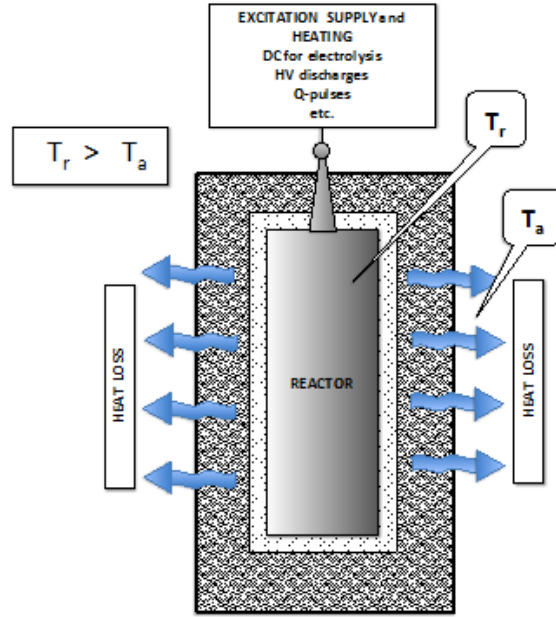


Figure 2. Schematic of a simple LENR reactor. (a) Here, the heat flux is merely lost into the environment. No use can be made of the heat in this configuration. (b) Note however the presence of the thermal insulation, a compulsory feature of the system if we want to detect that $T_r > T_a$.

- E_h : additional heating to maintain the desired reactor temperature T_r .

These two quantities correspond to the total energy injected into the reactor

$$E_1 = E_e + E_h. \quad (1)$$

The electrical energy entering the reactor does not come directly from the mains, but is processed by a dedicated power supply. For instance, in the case of an electrolytic reactor, the power supply transforms the line power into an appropriate direct current. Similarly, the heating current intensity is controlled. The power supply is not perfect, so

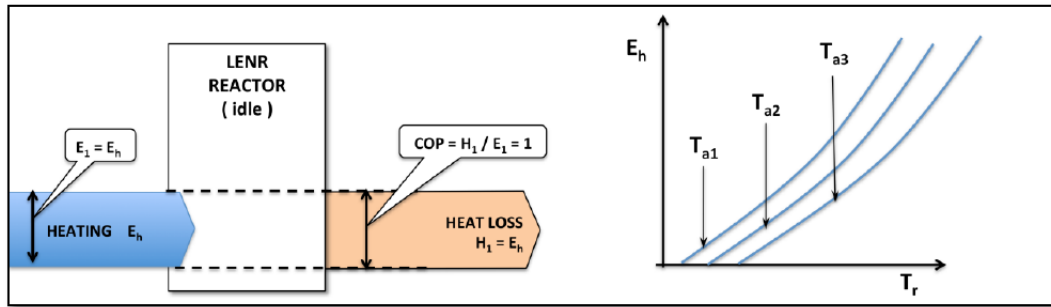


Figure 3. Calibration of the relationship temperature–heat loss ($T_r - H_1$) – Different curves may be required if the ambient temperature T_a is likely to vary.

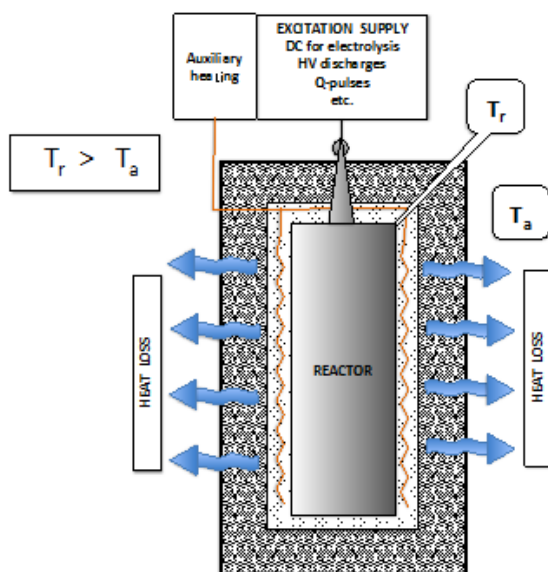


Figure 4. MODE 1. (a) The heat flux is lost into the environment. No use can be made of the heat in this configuration (Compare with Fig. 9). (b) The LENR heat and the additional electrical heating compensate the heat loss.

that some losses must be taken into account. The power consumed from the mains is

$$E_0 = (1/\alpha)E_1. \quad (2)$$

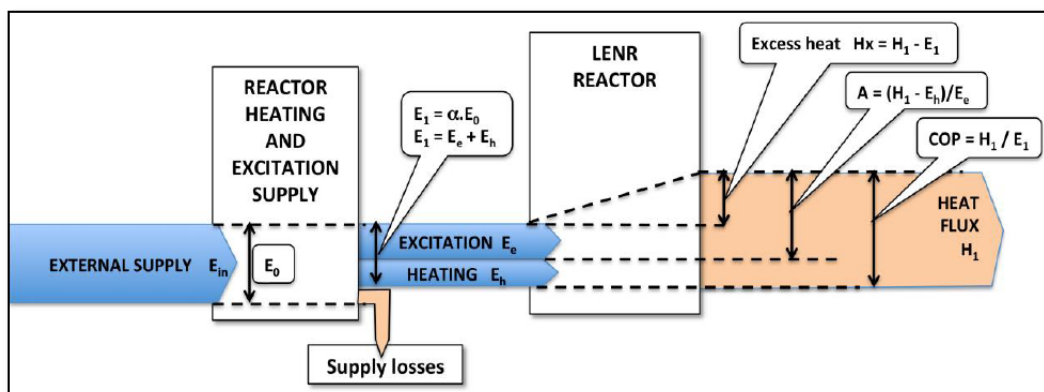


Figure 5. Energy flowchart for a heated LENR reactor (MODE 1) – Electrical energies are shown in blue, heat in orange.

The LENR reactor generates a heat flux H_1 . Because some reactions give off energy in the reactor, H_1 is larger than E_1 . We can define excess heat and coefficient of performance by the following formulas:

$$\text{Excess heat: } H_x = H_1 - E_1, \quad (3)$$

$$\text{Coefficient of performance (COP): } \text{COP} = H_1/E_1. \quad (4)$$

The inputs E_e and E_h are not equivalent. The heating E_h depends on the quality of the thermal insulation and is not directly related to LENR phenomena. Conversely, E_e is the driving force that triggers LENR heat. It is therefore interesting to evaluate the reactor efficiency via a number independent of E_h . We define the energy amplification factor A as follows:

$$\text{Amplification factor: } A = (H_1 - E_h)/E_e. \quad (5)$$

Reactors of the same technology built with different thermal insulations or simply differing by their size will have different COP values, but should be characterized by similar A values. The energy amplification factor is therefore more representative than the coefficient of performance to estimate the efficiency of a LENR reactor, at least if auxiliary heating is required.

5. Cooled Reactor – MODE 2 of Operation

If the excess power of the reactor is sufficient, the auxiliary heating is no longer required to maintain the internal temperature. We have

$$E_h = 0, \quad (6)$$

$$E_1 = E_e. \quad (7)$$

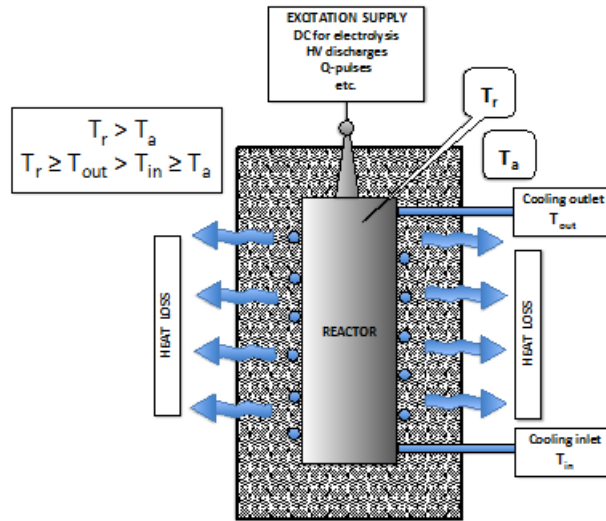


Figure 6. MODE 2 (a) While in operation, the LENR heat is sufficient to compensate the heat loss. (b) The additional heat is evacuated by a cooling system.

On the contrary, the heat produced must be evacuated by a cooling system in order to avoid an overheating. This operation type is called MODE 2 (Fig. 6).

The heat is removed by the circulation of a fluid through a heat exchanger arranged in direct contact with the reactive unit, underneath the thermal insulation blanket. The cooling power for a given T_r can be modulated via the fluid flow rate and inlet temperature.

Figure 7 shows the energy flowchart for a cooled reactor. In this MODE 2, we have:

$$\text{Excess heat: } H_x = H_1 + H_2 - E_e. \quad (8)$$

$$\text{Amplification factor: } A = \text{COP} = (H_1 + H_2)/E_e. \quad (9)$$

The energy input to the reactor is limited to the excitation E_e . Heat output H_2 goes to the cooling system. The heat leaves the reactor unit at a temperature equal or less than T_r . It can be transferred to a user at a temperature T_u inferior to T_r , but ideally higher than T_a . Heat H_1 is lost through the thermal insulation. In Fig. 7, this heat is dissipated in the surroundings at the temperature T_a . However, another configuration is possible, as explained in Section 7.

In the particular case of a reactor that does not need an excitation power supply, we have $E_e = 0$. The MODE 2 is then equivalent to a self-heated or self-sustained operation. The amplification factor and the COP are infinite and do not represent relevant parameters.

6. Importance of the Thermal Insulation

Let us consider the heat balance of a reactor. The LENR excess energy H_x is essentially proportional to the mass of reacting matter, hence to the internal volume V of the reactor, as well as the excitation energy input E_e .

The heat loss H_1 depends on the external surface S of the enclosure, but also on the quality of the insulation material and its thickness t . If L is the characteristic dimension of the reactor, V is proportional to L^3 and S to L^2 . We write

$$E_e + H_x = AL^3, \quad (10)$$

$$H_1 = (B/t)L^2, \quad (11)$$

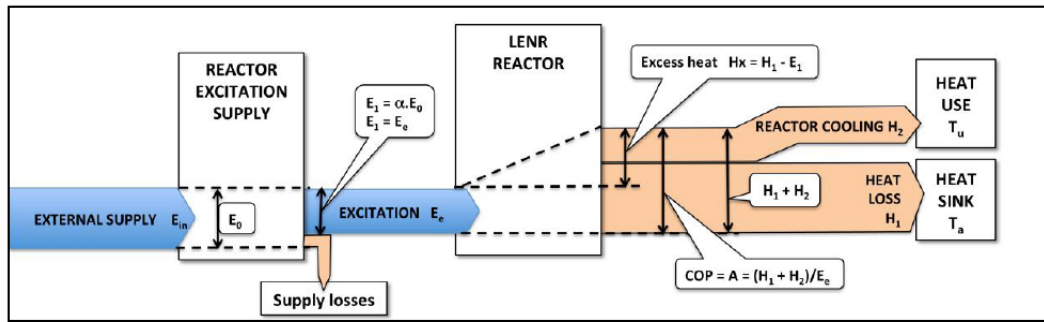


Figure 7. Energy flowchart for a cooled reactor (MODE 2).

where

- A is a factor characteristic of the reactor technology.
- B is a factor characteristic of the thermal insulation design, such as the material thermal conductivity. We suppose in the above equation that the heat loss is governed by the heat conduction through the insulation lagging and that the external surface temperature is low enough to neglect the influence of the cooling by radiation

$$\frac{H_1}{E_e + H_x} = \frac{B/t}{AL} \quad (12)$$

We see that the ratio of the heat loss to the internal heat flux decreases as the dimension L increases. In addition, when the dimension of the reactor is enlarged, it is frequently easy to increase the insulation thickness t to the same proportion. Equation (12) becomes

$$\frac{H_1}{E_e + H_x} = \frac{B/t}{AL} = \frac{B'}{AL^2} \quad (13)$$

The ratio is now inversely proportional to the square of the size. Figure 8 compares two situations.

7. Active Cooling

An active cooling configuration is characterized by a thermal insulation that is continuously swept by a flow of gas going inward [7]. The gas flow rate is carefully selected in order to maintain the outer surface just at ambient temperature. The heat removed by this gas flow is then equal to the heat loss of the insulation. If the gas flow rate is lower than this optimum one, the outer surface is warmer than the ambient temperature, and heat is lost across the hot surface.

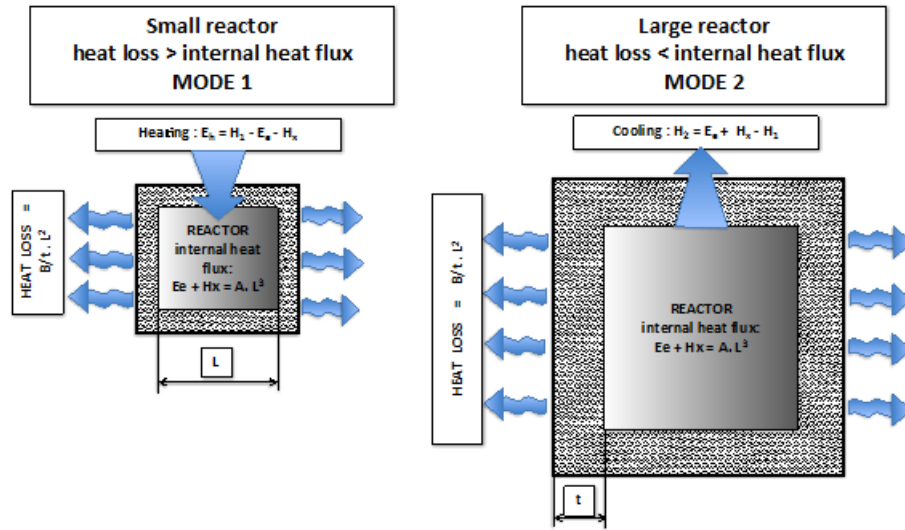


Figure 8. Influence of the reactor size – A larger unit may accommodate a thicker insulation – A given reactor technology operated in MODE 1 as a small unit may become a MODE 2 reactor in a larger size.

If the gas flow rate is too high, too much heat is subtracted from the reactor by the active cooling, so that less heat is available for the main cooling system.

The active cooling does not eliminate the heat loss, but the loss is now in the form of sensible heat that may have a usage. However, a clear distinction should be made between the reactor cooling itself, and the active cooling of the insulation:

- The energy is transferred to the reactor cooling circuit at the high temperature T_{out} . It can for example provide the latent heat required to vaporize water at that temperature if the reactor is designed as a boiler.
- The energy recovered by the active cooling is sensible heat. It could not vaporize a liquid at T_u , but could for instance preheat the flow of liquid water going to a boiler

Active cooling may be applied to all systems, including MODE 1. The reader is invited to compare Figs. 4 and 9 and imagine how to improve the design illustrated in Fig. 4.

8. MODE 2 with Feedback

A heat flux available at a temperature higher than T_a can be processed by a thermal engine to produce mechanical energy, easily transformed into electrical energy by a generator [8]. Theoretically, the thermal machine may also be an array of thermocouples able to elaborate electricity directly from the heat.

The electrical production E_{out} can be reintroduced at the supply input, so that the excitation power required from the external supply is reduced to $E_0 - E_2$ (Fig. 10).

9. MODE 3 of Operation

If the quantity of electricity produced by the generator exceeds the need of the power supply, there is a surplus of electricity that can be exported. This is the definition of autonomous or self-sustained operation, called here MODE 3 (Fig. 11).

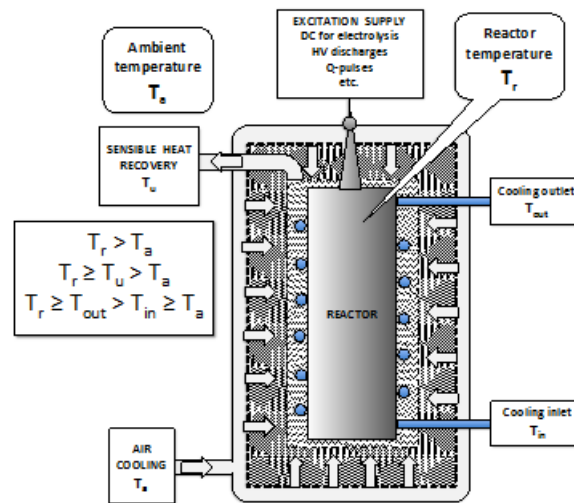


Figure 9. Active cooling. The thermal insulation is fitted with a laminar flow of gas that percolates inward. The gas leaves the enclosure at a temperature T_u that is higher than T_a and may be as high as T_r . The heat loss is recovered at a temperature above T_a and may have an usage.

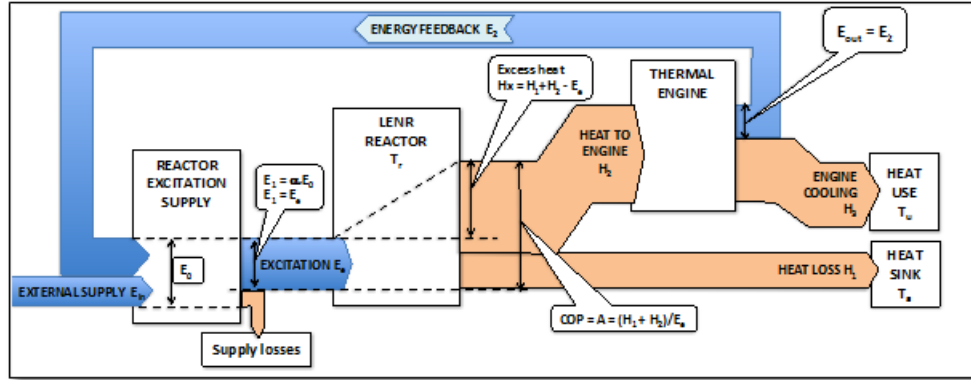


Figure 10. Mode 2 with feedback – The excess heat is transformed into electricity by a thermal engine coupled to a generator. This electrical energy E_{out} is fed back (E_2) to the supply, reducing the external energy consumption.

It is admitted in MODE 3 that an external power supply may still be temporarily required for the starting phase and for the safety of the control system. Following the design of the thermal engine and its performance, the heat output H_3 of the thermal engine may be recovered at an intermediate temperature for ancillary use (cogeneration). Similarly, active cooling may make it possible to find a use for the heat loss H_1 . This is shown in Fig. 12.

Let us consider the complete arrangement: Excitation supply – Reactor – Thermal engine. We can define the energy gain Z :

$$\text{Energy Gain : } Z = E_{out}/E_0 - 1, \quad (14)$$

where Z represents the gain of the system measured in electrical energy.

- If $Z = -1$, the system consumes electricity for the excitation supply and does not produce power. This is the case in MODE 1 and in MODE 2 if no thermal engine is incorporated.

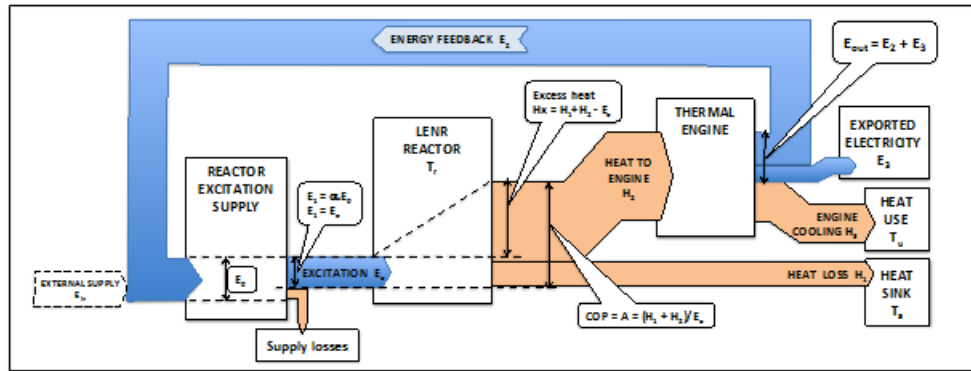


Figure 11. MODE 3 of autonomous operation – The electricity production E_{out} exceeds the consumption of the reactor excitation supply E – The surplus E_3 is exported.

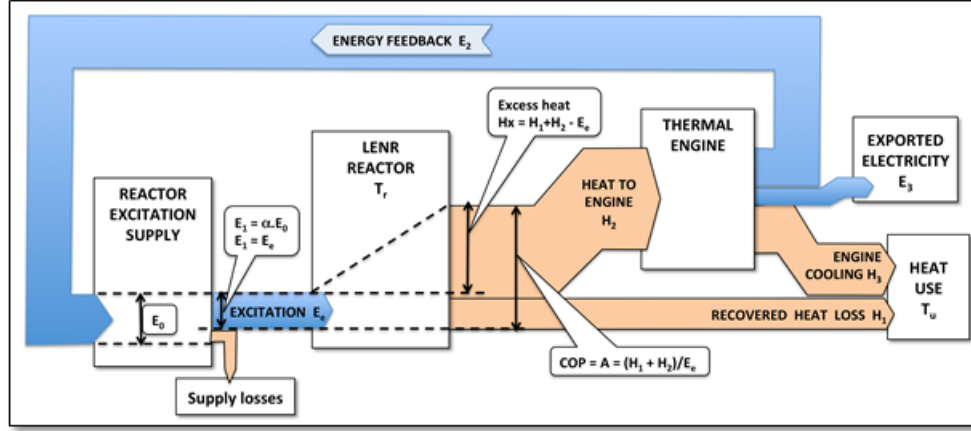


Figure 12. MODE 3 with recovery of the engine thermal output and active cooling.

- Z between -1 and 0 corresponds to Mode 2 with feedback,
- $Z > 0$ describes an autonomous system.

10. Conditions of Autonomous Operation

Different types of thermal engines are known, and it is not the purpose of this paper to describe them in detail. The thermodynamics teaches that these engines must take heat (H_{in}) from a source at a high temperature (T_{hot}) and reject a fraction at the heat sink at a lower temperature (T_{cold}) [9]. They are characterized by their efficiency:

$$\eta = E_{out}/H_{in}. \quad (15)$$

The efficiency is limited by the Carnot formula

$$\eta_c = 1 - T_{cold}/T_{hot}. \quad (16)$$

The engines are not perfect, so that the effective efficiency is lower than the theoretical one

$$\eta = \eta_c \eta_m, \quad (17)$$

where η_m is the machine efficiency. The machine efficiency includes all losses, e.g. the energy lost during the transformation of the mechanical energy into electricity, or the energy required to drive ancillary components like pumps, fans, control, etc. Figure 13 shows the efficiencies attained by different types of thermal engines.

These equations can be utilized to determine the COP required in order to obtain a given Z value. We write

$$E_1 = \alpha E_0, \quad (18)$$

$$\lambda = \frac{T_r}{T_a}. \quad (19)$$

The heat loss is written as a ratio of E via the formula

$$H_1 = f(\lambda - 1) E_0. \quad (20)$$

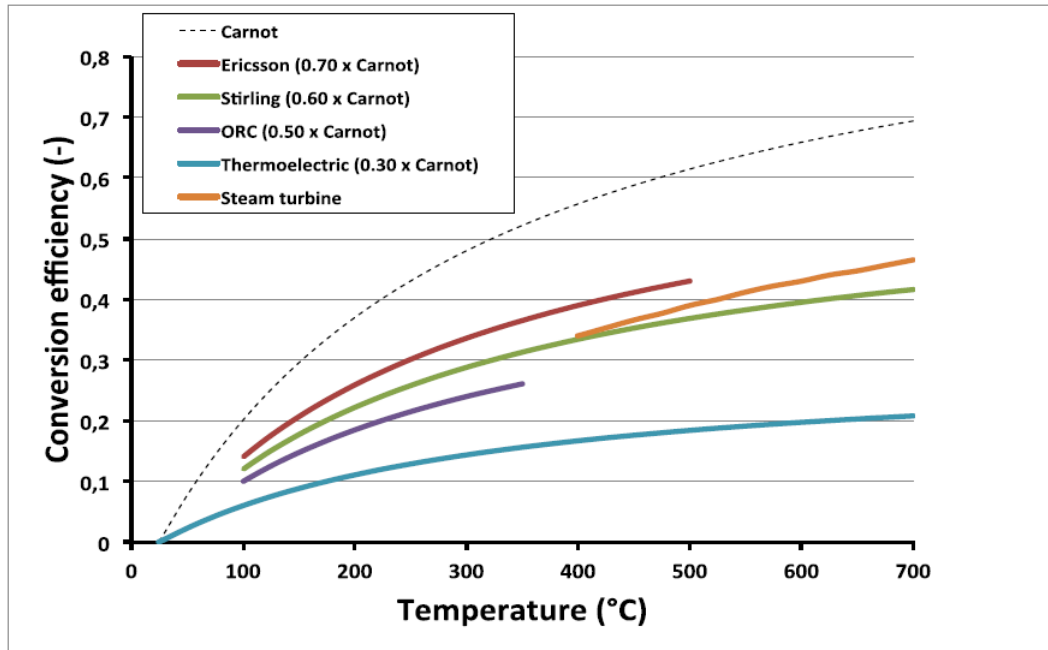


Figure 13. Relationship between the temperature of the heat source (T_{hot}) and the typical efficiency of various thermal engines – $T_{\text{cold}} = 25^{\circ}\text{C}$.

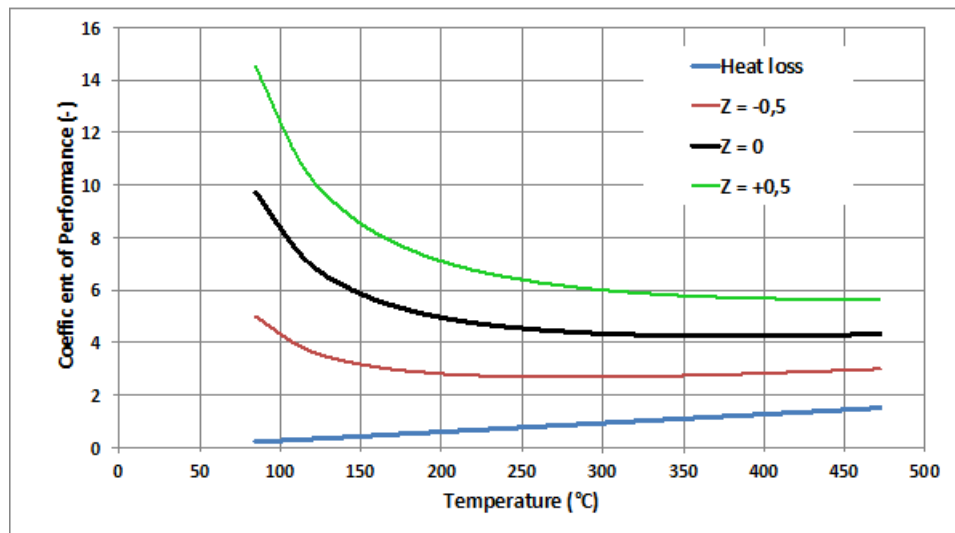


Figure 14. Relationship between the temperature and the COP for different Z values – $\eta_m = 0.7 - f = 1 - T_{\text{cold}} = 25^{\circ}\text{C}$.

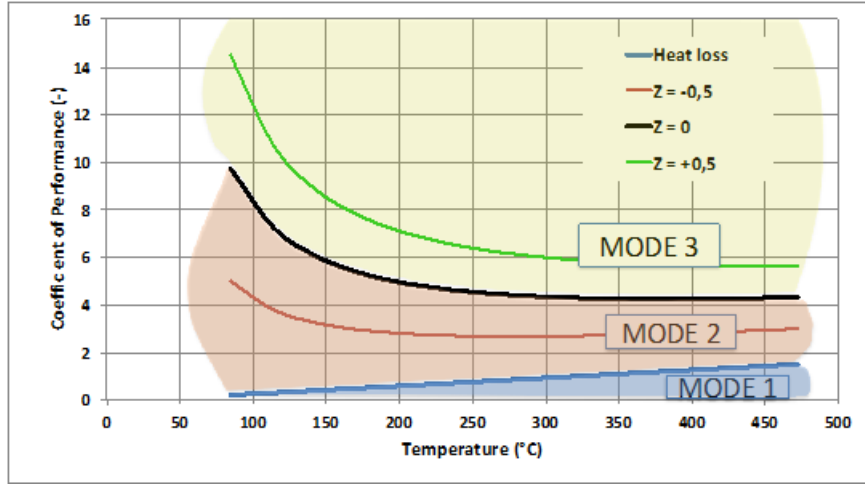


Figure 15. Operation mode domains as a function of the temperature and the COP – $\eta_m = 0.7 - f = 1 - T_{\text{cold}} = 25^\circ\text{C}$.

The efficiency is

$$\eta = \eta_m(\lambda - 1) / \lambda. \quad (21)$$

The energy balance gives

$$E_{\text{out}} = E_2 + E_3 = (1 + Z)E_0 = \eta H_2, \quad (22)$$

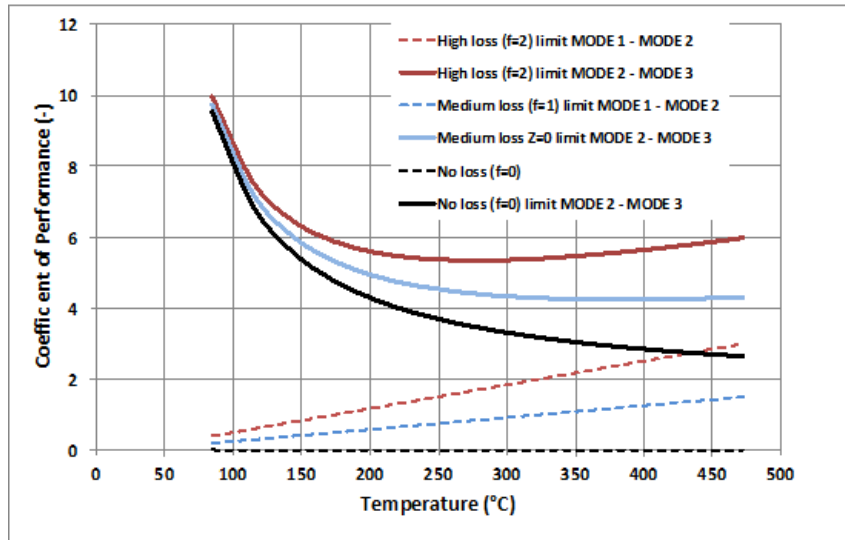


Figure 16. Limits of the different domains for several heat loss factors – $\eta_m = 0.7 - T_{\text{cold}} = 25^\circ\text{C}$.

$$H_2 = (1 + Z)E_0/\eta, \quad (23)$$

$$\text{COP} \propto E_0 = H_1 + H_2, \quad (24)$$

$$\text{COP} \propto E_0 = f(\lambda-1)E_0 + (1 + Z)E_0/\eta. \quad (25)$$

This yields

$$\text{COP} = \frac{f(\lambda-1)}{\alpha} + \frac{(1+Z)\lambda}{\alpha\eta_m(\lambda-1)}. \quad (26)$$

Equation (26) allows the calculation of the COP required for a given heat loss factor and a desired COP. Figure 14 presents an example of results.

The different operation modes are delineated in Fig. 15. The limits between the domains depend on the heat loss factor, as shown in Fig. 16. The COP required for an autonomous operation is reduced if the heat losses are low. It also decreases when the temperature increases, because of the better Carnot efficiency. Figure 16 shows that autonomous mode is difficult to attain for reactors operated at a temperature below 150°C.

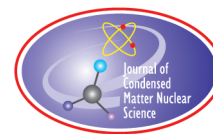
11. Conclusions

LENR reactors may be characterized by different parameters. Different modes of operation are described. The COP is not the best indicator for a reactor that requires external heating. The energy amplification factor should be preferred. The thermal insulation plays an important role. LENR reactors that require external heating in small units may become self-sustained for large sizes.

The production of electricity involves the coupling with a thermal machine. The system is able to export power if the COP and the temperature are high enough.

References

- [1] M. Srinivasan and A. Meulenberg (Guest editors), Special section: low energy nuclear reactions, *Current Sci.* **108**(4) (2015).
- [2] M. Fleischmann, S. Pons and M. Hawkins, Electrochemically induced nuclear fusion of deuterium, *J. Electroanal. Chem.* **261** (1989) 301–308; errata, **263** (1989) 187.
- [3] E.K. Storms, *The Science of Low Energy Nuclear Reaction*, World Scientific, Singapore, 2007, 312 pages.
- [4] M. Swartz, Excess power gain using high impedance and codepositional LANR devices monitored by calorimetry, heat flow, and paired stirling engines, *Proc. ICCF-14*, 10–15 August 2008, Washington, D.C. ISBN: 978-0-578-06694-3, 123 (2010).
- [5] R.A. Oriani, An investigation of anomalous thermal power generation from a proton-conducting oxide, *Fusion Technol.* **30** (1996) 281.
- [6] J.P. Biberian, G. Lonchamp, L. Bonnetain and J. Delepine, Electrolysis of LaAlO₃ single crystals and ceramics in a deuteriated atmosphere, *The Seventh Int. Conf. Cold Fusion*, Vancouver, Canada: ENCO Inc., Salt Lake City, UT, 1998, p. 27.
- [7] Transpiration cooling, www.thermopedia.com/transpiration_cooling
- [8] Heat engine, https://en.wikipedia.org/wiki/Heat_engine
- [9] Thermal efficiency, https://en.wikipedia.org/wiki/Thermal_efficiency



Research Article

Proton Conductors: Nanometric Cavities, H₂ Precipitates under Pressure, and Rydberg Matter Formation

François de Guerville*

i2-HMR International Institute for Hydrogen Materials Research, 56 Rue Estelle, 34 000 Montpellier, France

Abstract

Proton conductors (PC) are metal oxides often used as solid electrolyte with hydrogen above 400 K, in which anomalous presence increase of several chemical elements and excess heat would have been obtained from near-surface locations. Near the surface of other metal oxides, closely spaced hydrogen at a distance of only 2 pm at least during a fraction of the time has been detected, and has been proposed to be in the form of hypothetical ultradense Rydberg matter H(0). How can H(0) form in PC near the cathode interface? Nanometric cavities (NC) were observed in the PC near their cathode interfaces. These NC would contain H₂ precipitates with impurities, under a pressure of the order of 0.1 GPa. Since PC are crossed by a large flux of protons, a simple mechanism is proposed to increase the H₂ pressure in these NC rapidly and temporarily well above the PC tensile strength. A second mechanism is then described to turn this H₂ into a metallic-molecular state, form a Rydberg matter H(1) and then H(0) with a pressure decrease. In NC, the presence of impurities and the entry of the hydrogen atoms in the form of Rydberg atoms are proposed to decrease the pressure required to form metallic-molecular hydrogen. Finally, different experiments are proposed to test this research approach, particularly by transmission electron microscopy and Raman micro-spectroscopy.

© 2016 ISCMNS. All rights reserved. ISSN 2227-3123

Keywords: H₂ precipitates, Impurities, Large hydrogen flux, Nanometric cavities, Partial metallization of hydrogen, Pressure, Proton conductors, Rydberg states

1. Introduction

Some metal oxide crystals with perovskite structure are excellent Proton Conductors (PC). The PC can be used as solid electrolytes with H₂ above 400 K with porous electrodes. They are then penetrated by a very large hydrogen flux (proton conductivity up to 0.4 S/cm at 900 K) [1–3], and incorporate large concentrations of protons (several atomic percent) [4].

The PC are among the simplest and the most effective systems to study Condensed Matter Nuclear Science (CMNS). Mizuno et al. carried out CMNS experiments with polycrystalline PC based on Y-doped SrCeO₃ used as solid electrolytes at 650 K with deuterium passing through Pt porous electrodes, as shown in Fig. 1. Voltage and

*E-mail: francois.de.guerville@i2-hmr.com

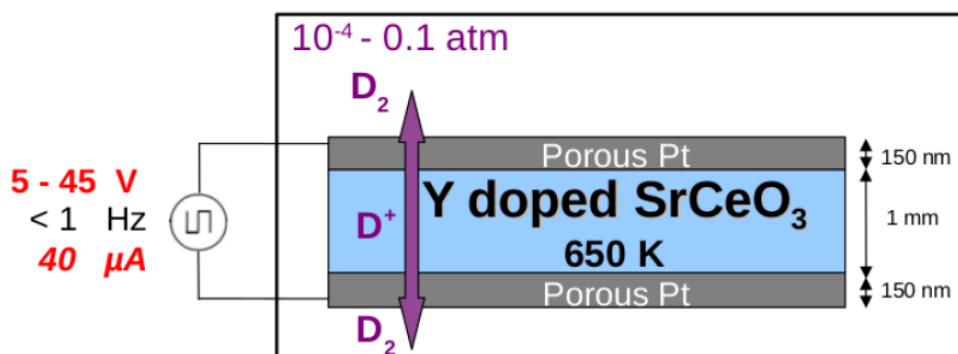


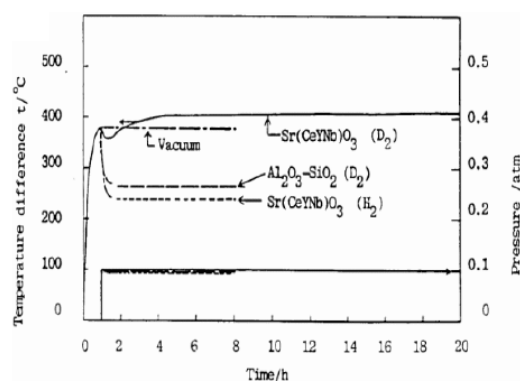
Figure 1. Mizuno's experimental system to study CMNS using a polycrystalline proton conductor based on Y-doped SrCeO_3 as solid electrolyte with D_2 . From [8].

intensity were as low as 18 V and $40 \mu\text{A}$. The unit cell of Y-doped SrCeO_3 keeps a centrosymmetric structure and thus there is no additional electric polarization of the material which could give additional kinetic energy to the hydrogen ions. Mizuno et al. have reported the observation of chemical elements in the PC near their electrode interfaces which were not present before electrolysis [5,6], and anomalous heat production during electrolysis [7–9], as shown in Fig. 2. Similar results were reported by other researchers with other PC [10–12].

Holmlid and coworkers' experiments have shown that, near the surface of highly porous metal oxide crystals based on K-doped Fe_2O_3 exposed to hydrogen, a part of the hydrogen atoms are separated from each other by only 2 pm at least during a fraction of time, as shown in Fig. 3a [13–18]. Other experiments are consistent with the presence of a significant population of compact pairs of hydrogen atoms in other hydrogenated materials [19]. This closely spaced hydrogen might be a new form of hydrogen, called $\text{H}(0)$, shown in Fig. 3b. $\text{H}(0)$ is a hypothetical ultradense form of Rydberg matter with a phenomenal density of 10^5 g/cm^3 . It might be a promising nuclear fuel, superfluid

Element	Before experiment	No excess heat	Excess heat evolved
Li	5 ± 0.7	5 ± 0.7	5 ± 1
Na	10 ± 1	10 ± 1	12 ± 1
Mg	5 ± 0.8	5 ± 1.2	10 ± 3
K	10 ± 0.9	10 ± 1.5	15 ± 1.8
Ca	20 ± 2	20 ± 0.8	40 ± 5
Ba	40 ± 5	40 ± 8	40 ± 10
Al	3 ± 0.2	5 ± 1	15 ± 5
Si	1.5 ± 0.1	3 ± 1	5 ± 1
Fe	0.5 ± 0.1	3 ± 1	5 ± 1
Ni	2 ± 0.1	3 ± 1	5 ± 1
Cu	0.3 ± 0.1	1 ± 1	1 ± 1
Cr	1 ± 0.1	2 ± 1	2 ± 1
Cd	0.5 ± 0.1	1 ± 0.5	1 ± 0.5
Pd	6.5 ± 1	6 ± 1	8 ± 2
Bi	0	0.1	5 ± 1
Zn	0.5 ± 0.1	1 ± 0.1	2 ± 0.2
Nd	2.5 ± 0.1	2.5 ± 0.1	4 ± 1
Sm	2.0 ± 0.1	2.0 ± 0.1	10 ± 1
Gd	0	0	5 ± 1
Dy	0	0	5 ± 1

(a)



(b)

Figure 2. (a) Elemental analysis for impurities in the proton conductor Y-doped SrCeO_3 , showing the presence increase of several chemical elements after electrolysis. (b) Anomalous heat production during electrolysis. From [6,8].

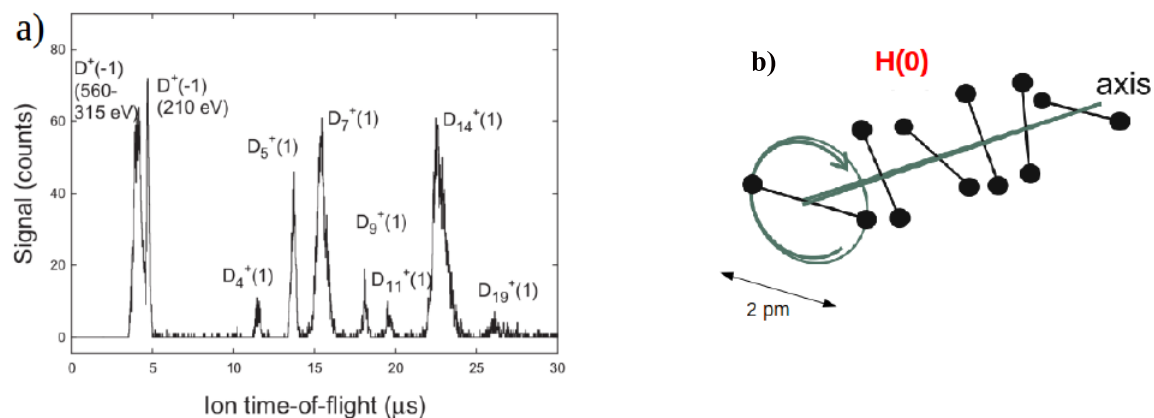


Figure 3. (a) Laser induced Coulomb explosions with time-of-flight mass spectroscopy near the surface of a metal oxide based on K-doped Fe_2O_3 . The two first peaks correspond to closely spaced deuterons (2 pm). From [13]. (b) Hypothetical ultradense hydrogen Rydberg matter $\text{H}(0)$. From [18].

and superconductive at room temperature. The presence of $\text{H}(0)$ in a PC near its cathode interface could explain the observation of new chemical elements and excess heat.

$\text{H}(0)$ would form almost spontaneously from classical hydrogen Rydberg matter $\text{H}(1)$. $\text{H}(1)$ can be viewed as a generalized metal [20–24]. Moreover, $\text{H}(0)$ could be formed directly from H_2 at ultrahigh pressures. Thus, the route explored in this article points toward metallization of hydrogen and high pressures. The main question of this article is: How to form hydrogen Rydberg matter in a PC used as solid electrolyte with H_2 at 650 K near its cathode interface?

2. State of the Art in Condensed Matter Physics

2.1. Nanometric cavities and H_2 precipitates under pressure

There has not been much research into nanoscale structure of PC with large densities of incorporated protons. However, crystalline silicon and metal oxides with perovskite structure implanted by large quantities of protons have been intensely studied, and this knowledge can be adapted to PC.

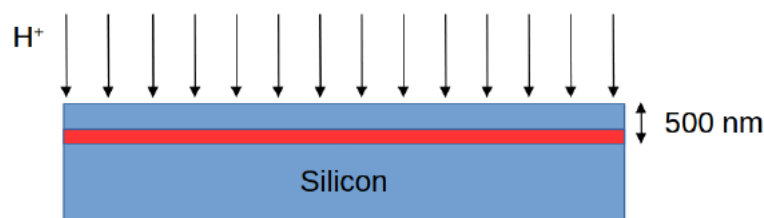


Figure 4. Ionic implantation of H^+ in silicon crystals.

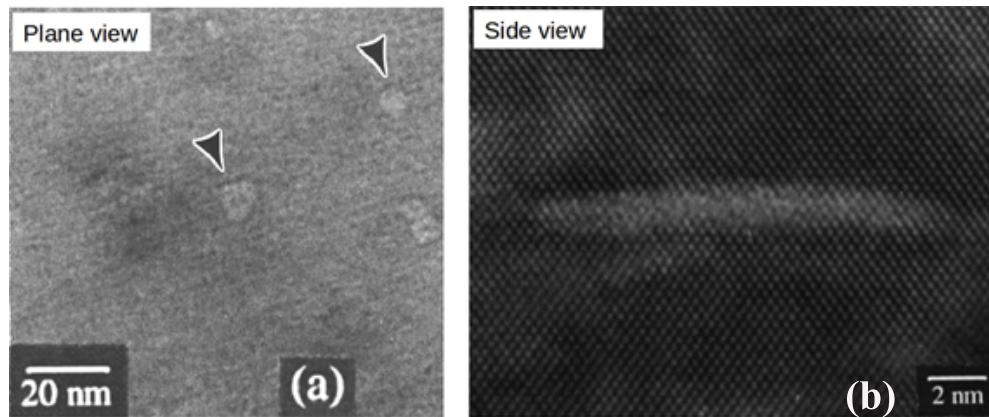


Figure 5. Nanometric cavities in H^+ implanted silicon, after an annealing at 720 K, observed by TEM. (a) Plane view and (b) cross-section side view. From [26].

2.1.1. In silicon implanted with H^+

Silicon does not conduct protons. With the ionic implantation technique, crystal surfaces are temporarily penetrated by a large flux of hydrogen ions. This technique is used to obtain large hydrogen local concentrations in these materials, typically at a depth of several hundred nanometers under the surface, as shown in Fig. 4. During material implantation, many point defects are created among which vacancy-hydrogen complexes V_nH_m [25].

During annealing, when hydrogen concentration locally overtakes the solubility limit, these mobile complexes V_nH_m agglomerate to form disk-shaped cavities of about ten nanometers in diameter [26–28]. This co-precipitation of vacancies and hydrogen, followed by the competitive growth (“Ostwald ripening”) of the Nanometric Cavities (NC) and their coalescence, allow the crystalline matrix-defects system to minimize its elastic energy. Such NC are observable by Transmission Electron Microscopy (TEM) after an annealing at 720 K [26]. Figure 5a shows some NC in their disc plane (plane view). Figure 5b, obtained from a TEM cross-section of the sample, shows a NC perpendicularly

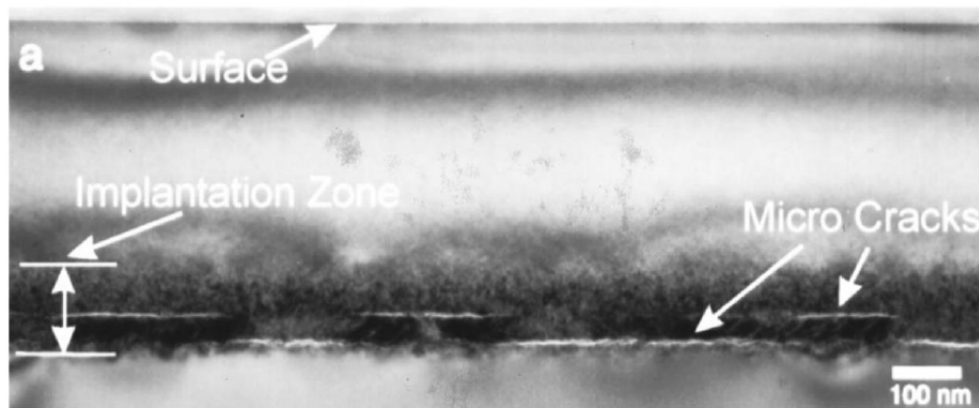


Figure 6. Nanometric cavities in H^+ implanted silicon, after an annealing at 870 K for 30 min, observed by cross-sectional TEM. From [29].

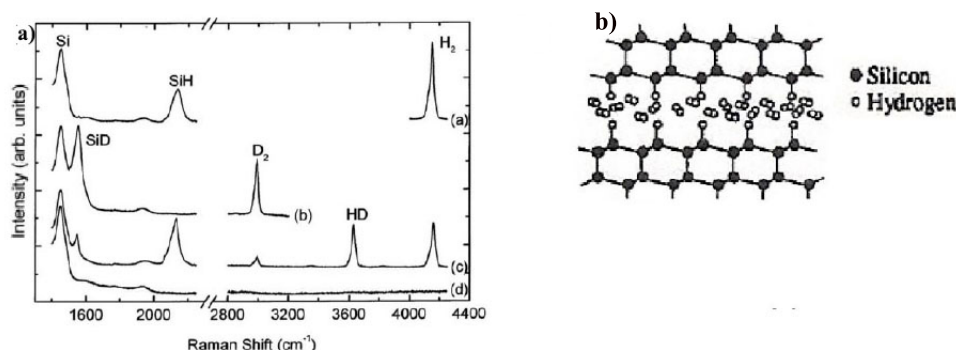


Figure 7. (a) Raman spectroscopy on Si surface implanted with hydrogen ions at 470 K showing the presence of H_2 molecules in nanometric cavities. From [31]. (b) Diagram of H_2 molecules trapped in Si nanometric cavities. From [29].

to its disc plane (side view). Figure 6 shows microcracks formed from a large density of NC in the implantation zone after an annealing at 870 K [29].

These NC contain precipitates of molecular hydrogen H_2 [29–32]. They are traps for hydrogen and for impurities [33], and they contain most of the implanted hydrogen [32]. The presence of H_2 in these NC was established by Raman spectroscopy. In Fig. 7a, the top Raman spectrum is composed of three peaks. The first two correspond to Si–Si and Si–H vibrations. The third one corresponds to the H–H vibration of H_2 (vibron) and has a characteristic position when the H_2 is fluid, as it is the case here [30,31]. Figure 7b shows hydrogen molecules H_2 in a NC [29].

The H_2 filling a NC is typically pressured to a dozen of GPa at 300 K [34–37]. This value is above the tensile strength of silicon, around 7 GPa. It is expected that this internal pressure of H_2 is much larger during annealing above 650 K [34]. This pressure decreases when the diameter of the NC increases. Reciprocally, this H_2 under pressure generates stress on the crystalline matrix. The resulting strain field contrast surrounding a NC can be observed by TEM, as shown in Fig. 8a [28]. A diagram showing the pressure of H_2 in NC on the Si crystalline matrix is presented in Fig. 8b [29].

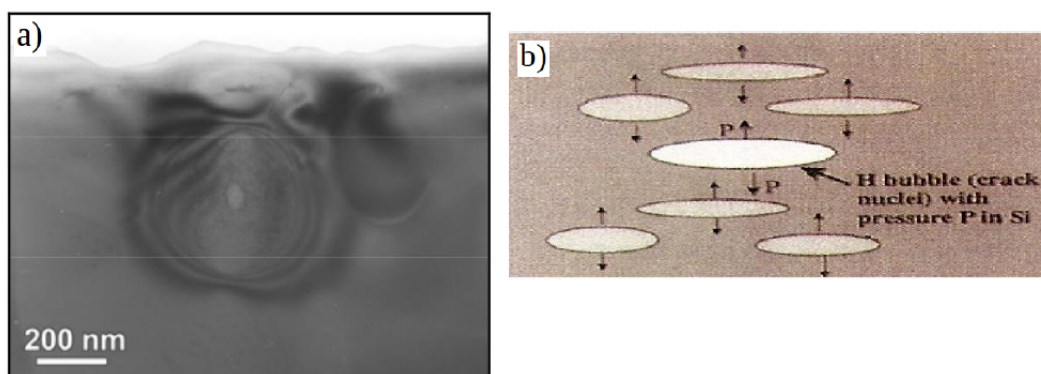


Figure 8. (a) Cross-section TEM image showing a nanometric cavity pressurized by its internal H_2 , and the long-range surrounding strain field, deep under the free surface of a hydrogenated Si wafer below 470 K. From [28]. (b) Diagram showing the pressure of H_2 in nanometric cavities on the Si crystalline matrix. From [29].

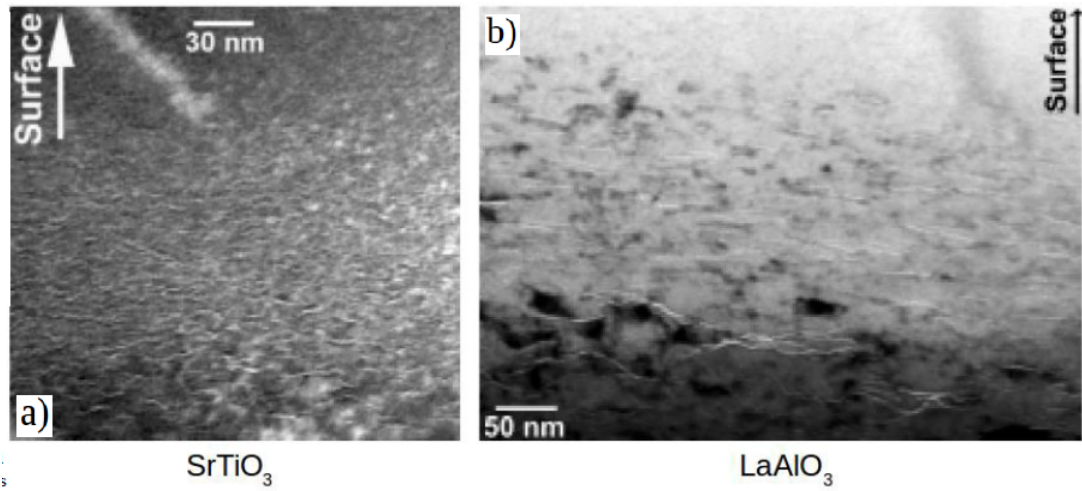


Figure 9. TEM images of high local densities of hydrogen related nanometric cavities (*side view*) in metal oxides with perovskite structure near their surfaces. These samples were implanted with hydrogen at 300 K for SrTiO₃ (a) and 570 K for LaAlO₃ (b). From [38].

2.1.2. In metal oxides with perovskite structure implanted with H^+

The same phenomena are observed in metal oxides with perovskite structure, such as SrTiO₃, BaTiO₃, LaAlO₃ and LiTaO₃ [38–40]. The two TEM images in Fig. 9 show large densities of NC under the surfaces of SrTiO₃ and LaAlO₃ [38].

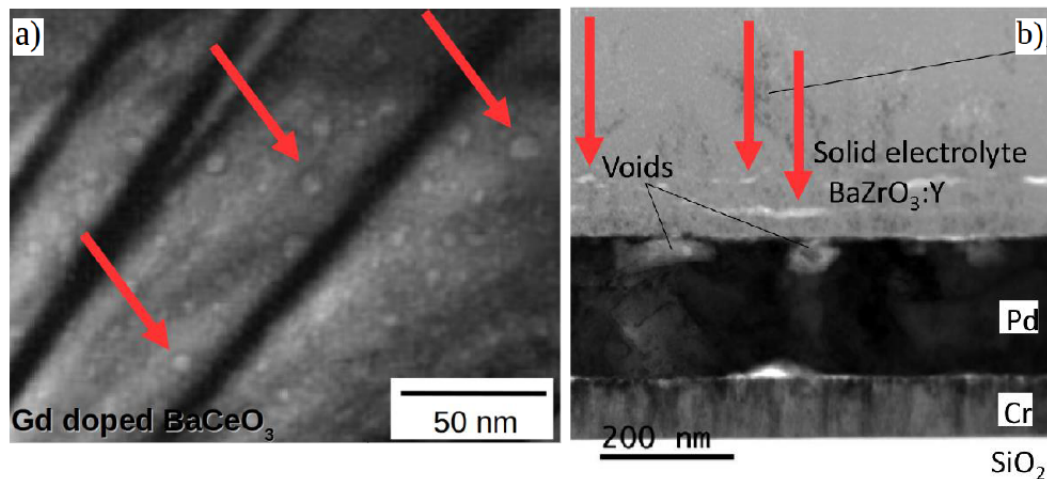


Figure 10. TEM images of nanometric cavities in polycrystalline proton conductors. Red arrows highlight some nanometric cavities. (a) Plane view in Gd-doped BaCeO₃ used below 770 K. From [41]. (b) Cross-section side view in Y-doped BaZrO₃ used at 590 K. From [42].

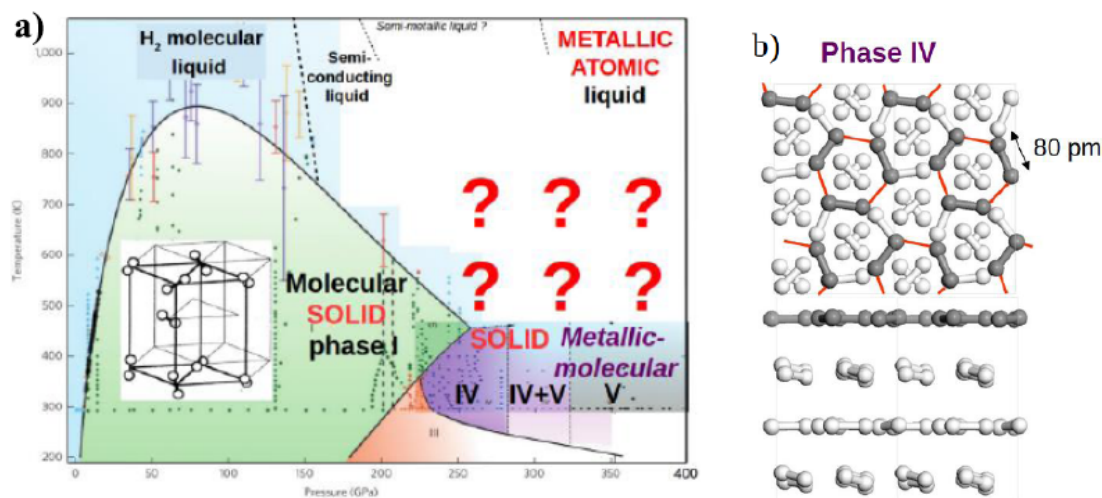


Figure 11. (a) Phase diagram $P - T$ of pure hydrogen, established by Raman spectroscopy. From [44, 46–51]. (b) Metallic-molecular phase IV of hydrogen. From [51].

In hydrogen-implanted BaTiO₃, the internal pressure of H₂ in microcracks was evaluated between 0.004 and 0.5 GPa [39]. This pressure should be considerably higher in NC. The tensile strength of polycrystalline BaTiO₃ is 0.06 GPa.

2.1.3. In proton conductors used as solid electrolytes with hydrogen

High densities of NC related to hydrogen incorporation have been observed by TEM in three polycrystalline PC used as solid electrolytes with hydrogen [41–43]. Figure 10 shows TEM images of Gd-doped BaCeO₃ used below 770 K (Fig. 10a) and Y-doped BaZrO₃ used at 590 K (Fig. 10b). For Y-doped BaZrO₃, these NC were found within a depth

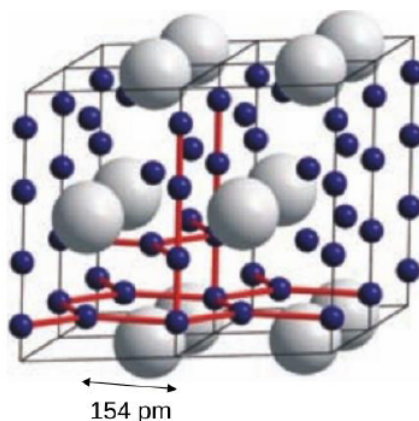


Figure 12. Fully metallic phase of SiH₄ at only 113 GPa at 300 K. From [53].

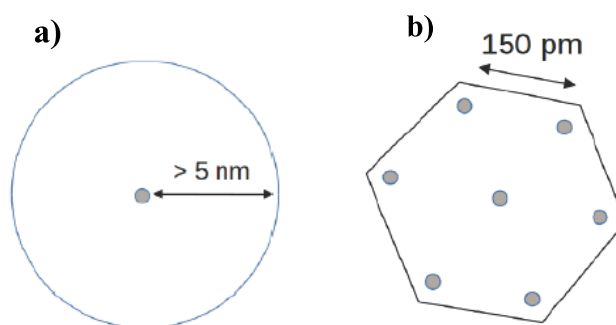


Figure 13. (a) Hydrogen Rydberg atom. (b) Hydrogen Rydberg matter H(1).

of 100 nm from its cathode interface, whereas for $\text{Ba}_3\text{Ca}_{1.18}\text{Nb}_{1.82}\text{O}_{9-\delta}$ used at 1020 K, these NC were found in its grain boundaries.

The phenomena observed in PC near their cathode interface when they are used as solid electrolyte with hydrogen at around 650 K can be similar to those observed in silicon and in metal oxides with perovskite structure implanted with H^+ .

2.2. Partial metallization of hydrogen

2.2.1. Hydrogen with impurities under high pressures

Pure hydrogen can be compressed to high pressures in disk-shaped diamond anvil cells, whose dimensions are typically 100 μm in diameter and 5 μm in thickness [44–49]. The pressure–temperature phase diagram of hydrogen, obtained by Raman spectroscopy, is presented in Fig. 11a [44,46–51]. Hydrogen is a molecular solid in phase I above 5 GPa at 300 K, and above 23 GPa at 650 K. Above 250 GPa at 650 K, the phase of hydrogen has not been studied yet.

Above 250 GPa and at 300 K, hydrogen is a metallic-molecular solid in phase IV and/or V. As shown in Fig. 11b, the structures of these phases are constituted of alternating layers of :

- (1) H_2 molecules forming sheets of graphene type by intermolecular coupling, and whose state is intermediate between metallic state and molecular state,
- (2) normal hydrogen molecules H_2 .

In metallic-molecular H_2 , the intramolecular length of H_2 , initially equal to 74 pm, increases with pressure [51].

Although whether it is possible to produce metallic hydrogen in the laboratory is still debated, above 450 GPa and at room temperature (not shown), hydrogen is supposed to be fully metallic and superconducting.

The presence of some impurities (Li, Si, S, ...) significantly decreases the pressure required to approach a metallic state when hydrogen is compressed in a diamond anvil cell [52–55]. Figure 12 shows the structure of metallic SiH_4 under 113 GPa at 300 K, but SiH_4 is fully metallic above only 50 GPa [53]. In this configuration, hydrogen atoms are separated from each other by 154 pm.

2.2.2. Rydberg states

Different Rydberg states are shown in Fig. 13. A hydrogen Rydberg atom (Fig. 13a) is a hydrogen atom with its electron orbiting very far from the proton ($> 5 \text{ nm}$), quasi-circularly [56]. It results from recombination of a proton

and an electron, and it easily forms on metal oxide surfaces.

Hydrogen Rydberg matter H(1) is a hexagonal plane cluster of circular Rydberg atoms (Fig. 13b), whose electrons are strongly excited and delocalized [20–24]. In this phase, hydrogen is a generalized metal which has properties similar to covalent bonding. Protons are separated from each other by 150 pm at the fundamental energy level.

3. Research Approach

3.1. Rapid and temporary increase of H_2 pressure in nanometric cavities of proton conductors

This research approach starts with the facts that PC, submitted to electrolysis with H_2 at 650 K, can contain a high local density of NC near their cathode interfaces and are crossed by a large flux of hydrogen.

Hypothesis 1: The NC contain H_2 and hydrogen combined with impurities under a pressure on the order of 0.1 GPa.

Hypothesis 2: The NC are penetrated by a large flux of hydrogen.

Hypothesis 3: The entering hydrogen is trapped in the NC in the form of H_2 , and the outgoing hydrogen flux is negligible compared to the entering flux.

Hypothesis 4: The internal pressure of the hydrogen in the NC increases rapidly and temporary well above the PC tensile strength. The questions arising from this hypothesis are discussed in Section 4.1.

3.2. Ultradense Rydberg matter formation in nanometric cavities of proton conductors with decrease of H_2 pressure

From now on, H(0) is supposed to exist and to possibly form in PC. The proposed H(0) formation mechanism is illustrated in Fig. 14.

Hypothesis 5: In NC with a diameter greater than 40 nm, hydrogen penetrates in the form of circular Rydberg atoms ($n \geq 20, l = m = n - 1$).

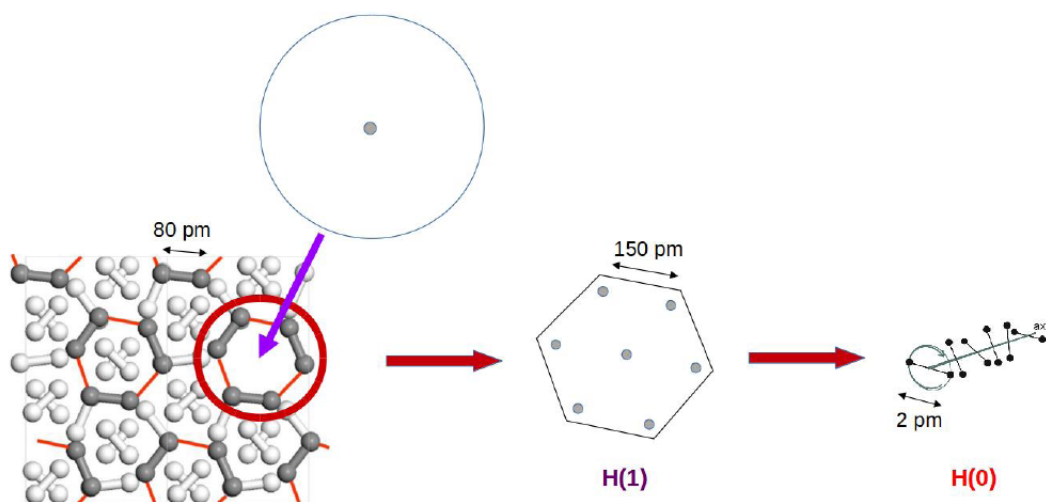


Figure 14. Proposed mechanism for H(1) formation in nanometric cavities consisting of circular hydrogen Rydberg atoms bombarding metallic-molecular hydrogen sheets, followed by the formation of the hypothetical H(0) and decrease of pressure.

Hypothesis 6: The H_2 with impurities in the NC turns temporarily into a metallic-molecular phase. The required temporary internal pressure could be only on the order of tens GPa.

Hypothesis 7: Circular Rydberg atoms penetrating into the NC transfer their excitation energy to the metallic-molecular sheets of H_2 in the immediate proximity of the NC wall, and together, they turn into Rydberg matter H(1).

Hypothesis 8: H(1) spontaneously turns into H(0) under the conditions prevailing in the NC. This transition is accompanied by a pressure decrease in the NC.

4. Discussion

4.1. Rapid and temporary increase of H_2 pressure in nanometric cavities well above the tensile strength of the proton conductor

It should take less than 1 min to increase the pressure of pure hydrogen from 0.1 to 20 GPa at 650 K, in a disk-shaped NC with a thickness of 1.5 nm penetrated by a flux of five hydrogen atoms per nm^2 per second at normal incidence, regardless of its diameter [57]. Nowadays, better PC (for instance, Y-doped $BaZrO_3$ single crystals) can achieve much larger fluxes than the one considered here, estimated from [8]. Otherwise, since NC trap impurities, they might acquire a global electrical charge, and the incoming proton flux in NC might be different from what was envisaged.

In NC, what mechanisms limit this pressure increase? From what is known for H^+ implanted silicon during annealing, H_2 pressure increase in NC should accelerate the NC growth by Ostwald ripening. Yet, the mechanical properties of the crystalline matrix change locally within the vicinity of a single pressurized NC [39]. Pressurized NC could implement compressive stress on the nearby PC matrix, thus having an inhibiting effect on the growth on each other [29].

Moreover, H_2 pressure increase in NC should accelerate the coalescence of a tiny part of the NC into microcracks, in which the internal pressure is lower. At a given annealing temperature, depending on the local concentration of hydrogen, the characteristic time needed to form microcracks can be on the order of 1 h. Consequently, the proposed rapid internal pressure increase may be little limited by the slower NC coalescence into microcracks. Finally, an open question is: Why have only Samgin et al. [11] reported the observation of cracks in their PC samples after CMNS experiments?

4.2. Rydberg matter formation

Other open questions follow. Is it possible to decrease the pressure required for partial metallization of hydrogen in NC down to several tens of GPa, thanks to the presence of impurities and the entry of hydrogen atoms in NC in the form of Rydberg atoms?

What is the NC optimum size to form H(1)? If the NC are too small, circular Rydberg atoms cannot enter them. If they are too large, the H_2 internal pressure may be too low to turn H_2 into metallic-molecular phase. I propose 40 nm in diameter and 1.5 nm in thickness is the optimum size. The best NC orientation should be parallel to the interfaces. Furthermore, could the formation of H_2 Rydberg molecules [58] play a role in H(1) formation?

5. Experimental Tests to Validate this Approach

5.1. Transmission electron microscopy

The TEM is the best tool to observe NC in a crystalline matrix, and study their locations, their sizes, their shapes, their orientations and their density. Strain field contrast is also observable around NC containing hydrogen under pressure.

Together with simulations, it is possible to deduce the H_2 pressure within the NC [34]. The TEM with electron energy-loss spectroscopy enables accurate mapping of hydrogen in the samples, and provides information on its bounding [59,60].

5.2. Raman micro-spectroscopy

Raman micro-spectroscopy reveals hydrogen vibrations and is the most adapted tool to detect the presence of H_2 with impurities trapped in the NC near the cathode interface. Moreover, this technique enables us to identify and study the hydrogen phase: molecular fluid, molecular solid, metallic-molecular solid, or Rydberg matter $H(1)$. For $H(1)$, it is possible to study electronic excitation and vibrational shifts of its partially covalent bonding [20]. However, the presence of impurities in the NC should complicate the deciphering of the Raman spectra. It may then be difficult to identify the hydrogen phase and evaluate its internal pressure.

Otherwise, stresses undergone by the crystalline matrix, generated by H_2 in the NC, are also roughly assessable by Raman spectroscopy.

Sample structural characterizations under the surface up to a depth of about $1\ \mu\text{m}$ can be carried out, after removing the cathode by chemical etching in an acid bath. By using a laser excitation wavelength below the optical absorption threshold, the probed depth can be decreased to about several hundreds of nm or less [61], which is the ideal depth to probe the NC. Furthermore, the use of confocal microscopy also limits the probed depth to $\sim 500\ \text{nm}$.

5.3. X-ray diffraction

X-ray diffraction enables us to measure strain perpendicular to the surface plane in a layer of a crystalline matrix, generated by a large density of in-plane NC containing H_2 under pressure. These measurements can be carried out in-situ [42]. Probed depth is around $2\ \mu\text{m}$.

5.4. Neutron scattering

Neutron diffraction can detect long range ordered structure of deuterium. It does not work so well on protium, due to its lower mass. If there is enough ordered deuterium in NC, a deuterium lattice may be detectable inside. Moreover, information could be obtained about the molecular dynamics and the collective dynamics of hydrogen (phonons) in NC. Yet, the probed depth is very large and the bulk of the sample is probed.

5.5. Nuclear magnetic resonance spectroscopy

An NMR spectrum with anomalously large shift in a proton NMR experiment would provide unambiguous independent confirmation of the presence of closely spaced hydrogen.

5.6. Laser-induced Coulomb explosions with time-of-flight mass spectroscopy

This technique allows to detect closely spaced hydrogen near a material surface, and evaluate the initial distance between them.

6. Conclusion

In proton conductors, used as solid electrolytes with hydrogen around 650 K, large densities of nanometric cavities can form near their cathode interfaces. Assuming these nanometric cavities contain H_2 precipitates with impurities under

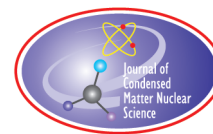
a pressure on the order of 0.1 GPa, a simple mechanism is proposed to increase rapidly and temporarily the H_2 internal pressure well above the tensile strength of proton conductors. Then, assuming hydrogen can exist as ultradense $H(0)$, a second mechanism is proposed to make the H_2 with impurities in the nanometric cavities turn into a metallic-molecular phase, form Rydberg matter $H(1)$ and then form $H(0)$ with a pressure decrease. In nanometric cavities, the presence of impurities and the entry of the hydrogen atoms in the form of Rydberg atoms are proposed to decrease the pressure required to form metallic-molecular hydrogen. Different experiments are proposed to study the hydrogen trapped in these nanometric cavities, particularly by transmission electron microscopy and Raman micro-spectroscopy.

References

- [1] A. Braun, A. Ovalle, V. Pomjakushin, A. Cervellino and S. Erat, Yttrium and hydrogen superstructure and correlation of lattice expansion and proton conductivity in the $BaZr_{0.9}Y_{0.1}O_{2.95}$ proton conductor, *Appl. Phys. Lett.* **95** (2009) 224103.
- [2] D. Pergolesi, E. Fabbri, A. D'Epifanio, E. Di Bartolomeo, A. Tebano, S. Sanna, S. Licoccia, G. Balestrino and E. Traversa, High proton conduction in grain-boundary-free yttrium-doped barium zirconate films grown by pulsed laser deposition, *Nat. Mater.* **9** (2010) 846.
- [3] Y.B. Kim, T.M. Gür, H.J. Jung, S. Kang, R. Sinclair and F.B. Prinz, Effect of crystallinity on proton conductivity in yttrium-doped barium zirconate thin films, *Solid State Ionics* **198** (2011) 39.
- [4] M. Glerup, F.W. Poulsen and R.W. Berg, Vibrational spectroscopy on protons and deuterons in proton conducting perovskites, *Solid State Ionics* **148** (2002) 83.
- [5] T. Mizuno, K. Inoda, T. Akimoto, K. Azumi, M. Kitaichi, K. Kurokawa, T. Ohmori and M. Enyo, Anomalous gamma peak evolution from SrCe solid state electrolyte charged in D_2 gas, *Int. J. Hydrogen Energy* **22** (1997) 23.
- [6] T. Mizuno, T. Akimoto, K. Azumi, M. Kitaichi, K. Kurokawa and M. Enyo, Excess heat evolution and analysis of elements for solid state electrolyte in deuterium atmosphere during applied electric field, *J. New Energy* **1**(1) (1996) 79.
- [7] T. Mizuno, T. Akimoto, K. Azumi, M. Kitaichi, K. Kurokawa and M. Enyo, Anomalous heat evolution from a solid-state electrolyte under alternating current in high-temperature D_2 gas, *Fusion Sci. Technol.* **29** (1996) 385.
- [8] T. Mizuno, M. Enyo, T. Akimoto and K. Azumi, Anomalous heat evolution from SrCeO₃-type proton conductors during absorption/desorption of deuterium in alternate electric field, *Proc. ICCF4* **2** (1993) 14-1.
- [9] R.A. Oriani, An investigation of anomalous thermal power generation from a proton-conducting oxide, *Fusion Sci. Technol.* **30** (1996) 281.
- [10] K.A. Kaliev, A.N. Baraboshkin, A.L. Samgin, E.G. Golikov, A.L. Shalyapin, V.S. Andreev and P.I. Golubnichiy, Reproducible nuclear reactions during interaction of deuterium with oxide tungsten bronze, *Phys. Lett. A* **172** (1993) 199.
- [11] A.L. Samgin, O. Finodeyev, S.A. Tsvetkov, V.S. Andreev, V.A. Khokhlov, E.S. Filatov, I.V. Murygin, V.P. Gorelov and S.V. Vakarín, Cold fusion and anomalous effects in deuterium conductors during non-stationary high-temperature electrolysis, *Proc. ICCF5* **2** (1995) 201.
- [12] J.-P. Biberian, G. Lonchamp, L. Bonnetain and J. Delepine, Electrolysis of LaAlO₃ single crystals and ceramics in a deuteriated atmosphere, *Proc. ICCF7* (1998) 27.
- [13] S. Badiei, P.U. Andersson and L. Holmlid, Production of ultradense deuterium: a compact future fusion fuel, *Appl. Phys. Lett.* **96** (2010) 124103.
- [14] F. Olofson and L. Holmlid, Detection of MeV particles from ultra-dense protium $p(-1)$: laser-initiated self-compression from $p(1)$, *Nucl. Instr. Meth. Phys. Res. B* **278** (2012) 34.
- [15] L. Holmlid, Excitation levels in ultra-dense hydrogen $p(-1)$ and $d(-1)$ clusters: structure of spin-based Rydberg matter, *Int. J. Mass Spectrom.* **352** (2013) 1.
- [16] L. Holmlid and S. Fuelling, Meissner effect in ultra-dense protium $p(l = 0, s = 2)$ at room temperature: superconductivity in large clusters of spin-based matter, *J. Cluster Sci.* **26** (2015) 1153.
- [17] L. Holmlid and S. Olafsson, Spontaneous ejection of high-energy particles from ultra-dense deuterium $D(0)$, *Int. J. Hydrogen Energy* **40** (2015) 10559.
- [18] L. Holmlid and B. Kotzias, Phase transition temperatures of 405–725 K in superfluid ultra-dense hydrogen clusters on metal surface, *AIP Advances* **6** (2016) 045111.

- [19] J. Kasagi, T. Ohtsuki, K. Ishii and M. Hiraga, Energetic protons and α particles emitted in 150-keV deuteron bombardment on deuterated Ti, *J. Phys. Soc. Jpn.* **64**(3) (1995) 777.
- [20] L. Holmlid, Observation of the unidentified infrared bands in the laboratory: anti-stokes stimulated Raman spectroscopy of a Rydberg matter surface boundary layer, *Astrophys. J.* **548** (2001) L249.
- [21] L. Holmlid, Conditions for forming Rydberg matter: condensation of Rydberg states in the gas phase versus at surfaces, *J. Phys.: Condens. Matter* **14** (2002) 13469.
- [22] J. Wang and L. Holmlid, Rydberg matter clusters of hydrogen $(\text{H}_2)_N^*$ with well defined kinetic energy release observed by neutral time-of-flight, *Chem. Phys.* **277** (2002) 201.
- [23] S. Badiel and L. Holmlid, Lowest state $n = 1$ of H atom Rydberg matter: many eV energy release in Coulomb explosions, *Phys. Lett. A* **327** (2004) 186.
- [24] S. Badiel and L. Holmlid, Experimental observation of an atomic hydrogen material with H–H bond distance of 150 pm suggesting metallic hydrogen, *J. Phys.: Condens. Matter* **16** (2004) 7017.
- [25] N. Cherkashin, F.-X. Darras, P. Pochet, S. Reboh, N. Ratel-Ramond and A. Claverie, Modelling of point defect complex formation and its application to H^+ ion implanted silicon, *Acta Mater.* **99** (2015) 187.
- [26] J. Grisolia, G. Ben Assayag, A. Claverie, B. Aspar, C. Lagahe and L. Laanab, A transmission electron microscopy quantitative study of the growth kinetics of H platelets in Si, *Appl. Phys. Lett.* **76** (2000) 852.
- [27] X. Hebras, P. Nguyen, K.K. Bourdelle, F. Letertre, N. Cherkashin and A. Claverie, Comparison of platelet formation in hydrogen and helium-implanted silicon, *Nucl. Instr. Meth. Phys. Res. B* **262** (2007) 24.
- [28] C. Ghika, L.C. Nistor, B. Mironov and S. Vizireanu, Hydrogen-plasma induced platelets and voids in silicon wafers, *Rom. Rep. Phys.* **62** (2010) 329.
- [29] T. Höchbauer, A. Misra, M. Nastasi and J.W. Mayer, Physical mechanism behind the ion-cut in hydrogen implanted silicon, *J. Appl. Phys.* **92** (2002) 2335.
- [30] K. Murakami, N. Fukata, S. Sasaki, K. Ishioka, M. Kitajima, S. Fujimura, J. Kikuchi and H. Haneda, Hydrogen molecules in crystalline silicon treated with atomic hydrogen, *Phys. Rev. Lett.* **77**(15) (1996) 3161.
- [31] A.W.R. Leitch, J. Weber and V. Alex, Formation of hydrogen molecules in crystalline silicon, *Materials Sci. Eng. B* **58** (1999) 6.
- [32] N. Cherkashin, N. Daghbouj, F.-X. Darras, M. Fnaiech and A. Claverie, Cracks and blisters formed close to a silicon wafer surface by He–H co-implantation at low energy, *J. Appl. Phys.* **118** (2015) 245301.
- [33] B. Mohadjeri, J.S. Williams and J. Wong-Leung, Gettering of nickel to cavities in silicon introduced by hydrogen implantation, *Appl. Phys. Lett.* **66** (1995) 1889.
- [34] J. Grisolia, G. Ben Assayag, B. de Mauduit and A. Claverie, TEM measurement of hydrogen pressure within a platelet, *Materials Res. Soc. Proc.* **681** (2001) I3.2.
- [35] X.-Q. Feng and Y. Huang, Mechanics of Smart-Cut(R) technology, *Int. J. Solids Structures* **41** (2004) 4299.
- [36] B. Aspar, C. Lagahe, H. Moriceau, A. Soubie, E. Jalaguier, B. Biasse, A. Papon, A. Chabli, A. Claverie, J. Grisolia, G. Ben Assayag, T. Barge, F. Letertre and B. Ghyselen, Smart-Cut(R) process: an original way to obtain thin films by ion implantation, *Int. Conf. Ion Implantation Technol. Proc.* (2000) 255.
- [37] S. Muto, S. Takeda and M. Hirata, Hydrogen-induced platelets in silicon studied by transmission electron microscopy, *Philosophical Magazine A* **72** (1995) 1057.
- [38] I. Radu, I. Szafraniak, R. Scholz, M. Alexe and U. Gösele, Ferroelectric oxide single-crystalline layers by wafer bonding and hydrogen/helium implantation, *Mat. Res. Soc. Symp. Proc.* **748** (2003) U11-8-1.
- [39] Y.-B. Park, P. Nardi, X. Li and H.A. Atwater, Nanomechanical characterization of cavity growth and rupture in hydrogen-implanted single-crystal BaTiO_3 , *J. Appl. Phys.* **97** (2005) 074311.
- [40] T. Luo, T. Oda, Y. Oya and S. Tanaka, IR observation on O-D vibration in LiNbO_3 and LiTaO_3 single crystal irradiated by 3 keV D_2^+ , *J. Nucl. Mater.* **382** (2008) 46.

- [41] S.M. Haile, D.L. West and J. Campbell, The role of microstructure and processing on the proton conducting properties of gadolinium-doped barium cerate, *J. Materials Res.* **13** (1998) 1576.
- [42] Y. Fukada, T. Hioki, T. Motohiro and S. Ohshima, In situ X-ray diffraction study of crystal structure of Pd during hydrogen isotope loading by solid-state electrolysis at moderate temperature, *J. Alloys Compounds* **647** (2015) 221.
- [43] T. Schober, H.G. Bohn, T. Mono and W. Schilling, The high temperature proton conductor $\text{Ba}_3\text{Ca}_{1.18}\text{Nb}_{1.82}\text{O}_{9-\delta}$ Part II: electrochemical cell measurements and TEM, *Solid State Ionics* **118** (1999) 173.
- [44] H.-K. Mao and R.J. Hemley, Ultra-high pressure transitions in solid hydrogen, *Rev. Modern Phys.* **66** (1994) 671.
- [45] M.I. Eremets and I.A. Troyan, Conductive dense hydrogen, *Nat. Mater.* **10** (2011) 927.
- [46] C.-S. Zha, R.E. Cohen, H.-K. Mao and R.J. Hemley, Raman measurements of phase transitions in dense solid hydrogen and deuterium to 325 GPa, *Proc. Natl. Acad. Sci. U.S.A.* **111** (2014) 4792.
- [47] R.T. Howie, P. Dalladay-Simpson and E. Gregoryanz, Raman spectroscopy of hot hydrogen above 200 GPa, *Nat. Mater.* **14** (2015) 495.
- [48] P. Dalladay-Simpson, R.T. Howie and E. Gregoryanz, Evidence for a new phase of dense hydrogen above 325 gigapascals, *Nature* **529** (2016) 63.
- [49] M.D. Knudson, M.P. Desjarlais, A. Becker, R.W. Lemke, K.R. Cochrane, M.E. Savage, D.E. Bliss, T.R. Mattsson and R. Redmer, Direct observation of an abrupt insulator-to-metal transition in dense liquid deuterium, *Science* **348** (2015) 1455.
- [50] I.I. Naumov, R.E. Cohen and R.J. Hemley, Graphene physics and insulator–metal transition in compressed hydrogen, *Arxiv* (2013) 1305.4649v1.
- [51] C.J. Pickard, M. Martinez-Canales and R.J. Needs, Density functional theory study of phase IV of solid hydrogen, *Arxiv* (2014) 1204.3304v2.
- [52] A.E. Carlsson and N.W. Ashcroft, Approaches for reducing the insulator–metal transition pressure in hydrogen, *Phys. Rev. Lett.* **50** (1983) 1305.
- [53] M.I. Eremets, I.A. Trojan, S.A. Medvedev, J.S. Tse and Y. Yao, Superconductivity in hydrogen dominant materials: silane, *Science* **319** (2008) 1506.
- [54] Y. Xie, Q. Li, A.R. Oganov and H. Wang, Superconductivity of lithium-doped hydrogen under high pressure, *Acta Crystallogr.* **C70** (2014) 104.
- [55] A.P. Drozdov, M.I. Eremets, I.A. Troyan, V. Ksenofontov and S.I. Shylin, Conventional superconductivity at 203 K at high pressures, *Arxiv* (2015) 1506.08190.
- [56] T.F. Gallagher, *Rydberg Atoms*, Cambridge University Press, Cambridge, 1994.
- [57] H. Shimizu, E.M. Brody, H.-K. Mao and P.M. Bell, Brillouin measurements of solid n-H₂ and n-D₂ to 200 kbar at room temperature, *Phys. Rev. Lett.* **47** (1981) 128.
- [58] J. Wang and L. Holmlid, Formation of long-lived Rydberg states of H₂ at K impregnated surfaces, *Chem. Phys.* **261** (2000) 481.
- [59] S. Muto, T. Tanabe and T. Maruyama, Cross sectional TEM observation of gas-ion-irradiation induced surface blisters and their precursors in SiC, *Mater. Trans.* **41** (2003) 2599.
- [60] H. Cohen, P. Rez, T. Aoki, P.A. Crozier, N. Dellby, Z. Dellby, D. Gur, T.C. Lovejoy, K. March, M.C. Sarahan, S.G. Wolf and O.L. Krivanek, Hydrogen analysis by ultra-high energy resolution EELS, *Microsc. Microanal.* **21** (2015) 661.
- [61] D.A. Tenne, A.K. Farrar, C.M. Brooks, T. Heeg, J. Schubert, H.W. Jang, C.W. Bark, C.M. Folkman, C.B. Eom and D.G. Schlom, Ferroelectricity in nonstoichiometric SrTiO₃ films studied by ultraviolet Raman spectroscopy, *Appl. Phys. Lett.* **97** (2010) 142901.



Research Article

Relativity and Electron Deep Orbits of the Hydrogen Atom

J.L. Paillet*

Aix-Marseille University, France

A. Meulenberg†

Science for Humanity Trust Inc., USA

Abstract

This work continues our previous works on electron deep orbits of the hydrogen atom. An introduction shows the importance of the deep orbits of hydrogen (H or D) for research in the LENR domain, and gives some general considerations on the Electron Deep Orbits (EDOs). In a first part we quickly recall the known criticism against the EDO and how we face it. In particular, a solution to fix all problems is to consider a modified Coulomb potential with finite value inside the nucleus. For this reason, we deeply analyzed the specific work of Maly and Va'vra on deep orbits as solutions of the Dirac equation, with such a modified Coulomb potential without singular point. Then, by using a more complete ansatz, we made numerous computations on the wavefunctions of these EDOs, allowing to confirm the approximate size of the mean radii $\langle r \rangle$ of orbits and to find further properties. Moreover, we observed that the essential element for obtaining deep orbits solutions is special relativity. At a first glance, this fact results from an obvious algebraic property of the expression of energy levels obtained by the relativistic equations. Now, a comparative analysis of the relativistic and of the non-relativistic Schrödinger equation allows us to affirm that Special Relativity leads to the existence of EDOs because of the *non-linear form of the relativistic expression* for the total energy, which implies a relativistic non-linear correction to the Coulomb potential.

© 2016 ISCMNS. All rights reserved. ISSN 2227-3123

Keywords: Deep electron levels, LENR, Relativistic quantum physics, Singular solutions

1. Introduction

With the quantum equations habitually used in the literature for computing the bound states of the H atom, we note that there is, in the relativistic form, a crossroad with a choice of value or a choice of sign for a square root in a parameter. According to which path is chosen, the resolution process leads either to the usual “regular” solution or to an unusual one called an “anomalous” solution. This latter is rejected in the Quantum Mechanics textbooks because of its singularity at $r = 0$.

*Corresponding author. E-mail: jean-luc.paillet@club-internet.fr.

†E-mail: mules333@gmail.com.

Why do we emphasize here the use of *relativistic* quantum equations? For (at least) two reasons:

- (1) The relativistic equations can predict EDOs with a mean radius of order femto-meter; whereas the normal non-relativistic equations do not. We give a simple mathematical reason for this fact.
- (2) With an EDO having a mean radius of order femto-meter, the Coulomb potential energy is high enough that the electron, so bound, is necessarily relativistic.

For many decades, the question of the existence of electron deep levels or EDOs for the hydrogen atom has led to a number of works and debates. The issue was raised early in the solutions to the Klein–Gordon and Dirac equations, which became the basis of modern quantum mechanics. Therefore, it could have been given a high degree of credence as the field developed to become the mainstream of modern physics. However, without experimental evidence to support the unusual claims, this issue could not be resolved and the deep-orbit solutions are still considered to be anomalous. With the advent of low-energy-nuclear reactions, LENR, such evidence (albeit indirect) may now be available. What are these orbits and why are they suddenly more important now?

- EDOs, predicted in the anomalous solutions of relativistic quantum equations, have mean radii of their orbitals of order femto-meter. This is five orders of magnitude smaller than the known atomic orbitals.
- So, hydrogen atoms (including deuterium) with an electron in a deep orbit (femto-atoms) can facilitate processes of LENR inside condensed matter. This occurs by ready penetration of atomic electron clouds and nuclear Coulomb barriers, by the avoidance of nuclear fragmentation in $D-D \Rightarrow {}^4\text{He}$ fusion reactions, and by a means of increasing the rate of energy transfer between an excited nucleus and the surrounding lattice
- Moreover, femto-atoms can create femto-molecules and both can combine with lattice nuclei for transmutation without the normal resultant energetic radiations. This is not possible by other mechanisms.
- Mathematical arguments against the anomalous solutions of the relativistic equations have dominated the discussion of this issue for over 50 years. However, by acceptance of the physical reality of a non-singular central potential within a nuclear region, these objections no longer pertain.
- Numerical methods, available now with modern computers, readily allow prediction of properties and features of the EDOs from the exact equations that are not possible with the approximations made to keep the relativistic equations in the form of analytic functions.

Possibly the first application for the deep-electron orbits was in an early explanation of the nature of the neutron as a proton with a tightly bound electron. This particular concept was rejected nearly a century ago on theoretical physics grounds for several reasons [1]. This rejection would have been much more difficult to accept had the charge density distribution of the neutron that is available today been known at the time [2]. The negative outer edge, presently attributed to a negative pion cloud, certainly looks like a deep-orbiting electron.

Since the late 1950s, whenever the deep-orbit solution was rediscovered (every decade), it was immediately rejected based on mathematical, rather than on physical, reasons. Therefore, because the issue was never resolved and the importance of these unobserved orbits was so questionable, the difficult (perhaps impossible at the time) experiments to verify their existence were never even attempted and the issue never became general knowledge in the profession. Decades later, when experimental evidence for halo nuclei was obtained, rather than use the known, but largely forgotten, deep-orbit solutions that would introduce the beginning of a whole new nuclear chemistry and physics, physicists just stretched the strong nuclear potential beyond all expectations to explain the phenomenon.

With the advent of LENR phenomena and subsequent research, recognition that electron proximity between the hydrogen nuclei was necessary to overcome the Coulomb barrier again brought the deep-orbit solutions to the relativistic quantum-mechanical equations into focus [3,4]. However, the concept was unknown within the field and therefore almost ignored. By 2005, it was not even possible to publish papers in favor of the concept. (At that time, it was still possible to get a paper on the subject into the arXiv, [5].) On the other hand, papers showing that such deep orbits

were mathematically forbidden could still be published in physics journals. The present authors have spent the last year proving, in several papers [6–8], that the singular Coulomb potential ($V = k/r = -\infty$ at $r = 0$) used to reject the deep-orbit solution, can be replaced by a more realistic one (in several versions) and can lead to a valid, non-singular solution for the deep orbits.

It was recognized early in the CF development that the best (perhaps the only) means of fusion at low temperatures and energies was to increase the time that negative charge spends between fusing nuclei. This means of overcoming the Coulomb barrier between nuclei is a continuing theme and is addressed in most models of LENR (see e.g., [9]). The other side of the problem was emphasized in 2013 (by Akito Takahashi at ICCF-15): “even if the Coulomb barrier were to be lowered to zero, D+D fusion would still lead to ^4He -fragmentation products, not to the observed atomic ^4He and heat of CF.” This problem is perhaps best addressed by the means and consequences of electron decay to the deep orbits [10,11].

With the recognition that deep-orbit electrons can explain some of the fundamental problems of cold fusion, a more complete study of the nature and effects of these relativistic electrons was begun [12]. An important side issue of this study was the nature of electromagnetic radiation from the deep-orbit electrons and the ability of deep-orbit electrons to transfer energy between an excited nucleus and the lattice [13]. As confidence grew in the CF results for transmutation in both the PdD and NiH systems, the concept of longer-lived “femto-atoms”, their nature and their consequences, became the subject of analysis [14,15]. These studies led to an understanding of 3-body fusion processes (femto-atom + nucleus) to explain both transmutation without hard radiation and selective radio-isotope remediation.

The most-often-challenged portion of the deep-orbit electron scenario is why the deep levels are not immediately filled from atomic orbitals and why are they not readily observed? While there are several reasons, a straight-forward reason involves the lack of overlap of all atomic orbitals, except for the $l = 0$, s-orbits, with the deep-electron orbits. The normal electro-magnetic transition (via photons) between two $l = 0$ levels is highly forbidden. If the deep levels are unable to be populated in the natural environment and in the normal manner, then how are we to get electrons into these levels? This latter question has been addressed in part by [16–18].

Since the deep-orbit model can explain all of the observed CF results that we have addressed and is based on the fundamental equations of relativistic quantum mechanics, it should be readily accepted. It is hoped that, with the cooperation of a mathematician and a physicist in the present authors, the non-physical reasons for rejecting the concept can be eliminated and a firm mathematical base can be laid that would lead to acceptance of both the deep orbits and a theory for cold fusion.

2. Arguments against the EDO States and Possible Solutions

The most known arguments against the EDO states, while assuming a singular $1/r$ Coulomb potential, have been already exposed in [6] and in a more developed way in [7], as well as the possible solutions to resolve these questions. They concern only the radial solutions of the quantum equations. We quickly recall these arguments and some counter-arguments

2.1. The wavefunction has a singular point at the origin

For the solutions called anomalous, the radial function $|R(r)| \rightarrow \infty$ when $r \rightarrow 0$ and the wavefunction $\psi(r, \theta, \varphi)$ does not obey a boundary condition. In fact, this problem comes from the expression of the Coulomb potential in $1/r$. So, some authors of EDO solutions remove this trouble by saying that the classical expression of the central potential is a good approximation for the bound state of a single electron atom, but considering the nucleus as a mathematical point is an unphysical abstraction. Also, one can argue against this problem by saying that the nucleus is not a point, but its charge is “smeared” over a distance of about 1fm. Solving the equation with a smeared out Coulomb potential

would produce a solution not diverging at the origin, but with certain minor changes on the EDO state. We indicate such solutions in Section 2.2.

We can add that, in the case of heavy nuclei, the accepted regular solutions of the relativistic Schrödinger equation also have a singular point at the origin, because the square of the coupling parameter $(Z\alpha)^2$ is not “small”; e.g. for atomic Cs, it is equal to ~ 0.16 , that gives $s \sim -0.2$ for $l = 0$ (for the parameter s , see Section 3.1.1).

2.2. The wavefunction is not square integrable

It is a serious problem, because in this case the wavefunction cannot be normalized in the entire space. As in Section 2.1., it results essentially from the behavior of the wavefunction ψ at the origin and not for $r \rightarrow +\infty$. Indeed, to define the norm of a wavefunction $\psi(r, \theta, \varphi)$ given in spherical coordinates, one has to compute $\int |\psi|^2 \sin \theta r^2 d\theta d\varphi dr = \int |Y(\theta, \varphi)|^2 \sin \theta d\theta d\varphi (\int |R(r)|^2 r^2 dr)$, where $Y(\theta, \varphi)$ are the so-called spherical harmonics, depending on quantum numbers l and m not indicated here. One knows the left integral is finite, while the right one depends on the behavior of $|R(r)|^2 r^2$ at the origin.

Here we can cite the work of Naudts [5], where an EDO state for hydrogen atom is found by using a Klein–Gordon equation, starting from a time-dependent *relativistic Schrödinger equation*. Because of chosen conditions on the parameters of the equation, the obtained solution is square integrable, thus normalizable. We have particularly developed explanations on this interesting result in [7], where the electron binding energy (BE) is very high in absolute value, with $|\text{BE}| \sim 507$ keV. We note the author only looks for solutions corresponding to spherically symmetric states, i.e. with angular quantum number (usually noted l) equal to 0.

Other works exist on singular states of the hydrogen atom, as e.g. in [19], where the author considers a compressed atom in a confinement potential described by a finite potential step at some given radius R_w taken at ~ 2.5 Å. A singular solution with deep orbits is obtained from a non-relativistic Schrödinger equation, by considering only the case $l = 0$, while using specific ansatz and approximation methods. But, because of the method used, the binding energy is not computed; neither is the mean radius. In fact, we think these levels could correspond to what we call pseudo-regular solutions [7].

Finally, we note most works on EDOs show that it is not possible to obtain square-integrable EDO solutions by means of the Dirac equations if keeping a Coulomb potential that is singular at the origin.

2.3. The orthogonality criterion cannot be satisfied

This mathematical condition, defined in a rather subtle way, corresponds to the fact the Hamiltonian, representing the total energy, must be a Hermitian operator, in order for its eigenvalues to be real, since they represent energy values of solutions. So, eigenfunctions corresponding to distinct values have to be orthogonal.

We can find in [20] the author examines the asymptotical behavior of the solutions of the non-relativistic Schrödinger, of the Klein–Gordon, and of the Dirac equations, as functions of formal variations of the coupling constant α , and looks for conditions to satisfy known orthogonality criterion for the equation solutions. In particular the author eliminates the EDO solutions. Nevertheless, one can find in works on self-adjoint extension of operators for potentials with a singularity, e.g. in [21], a mathematical proof that singular solutions of the Klein–Gordon equation satisfy orthogonality for at least an angular momentum $l = 0$. However, no positive result can be proved for the EDO solutions of the Dirac equations.

2.4. The strength of the binding seems to increase when the coupling strength decreases

In [22], the author imagines variations of the coupling constant α and observes consequences on eigenfunctions of a Klein–Gordon equation and of a 2-D Dirac equation. Doing this, he points to a very strange phenomenon concerning

the algebraic expressions of the EDO solutions: when α decreases and tends towards 0, the binding energy of the electron increases in absolute value.

We think this result is obtained in the context of an ill-defined system and is done so, uniquely, on a pure mathematical basis. Indeed, the coupling constant α can be expressed by $\alpha = e/c\hbar$. So, from a physical point of view, we can see α is actually entangled with several fundamental constants, in particular the Planck constant, the velocity of the light, and the elementary electric charge. So, modifying α without caution can certainly lead to paradoxical physical results (e.g., letting α go to zero means that the charge does also; thus, there are no bound states and no binding energy).

2.5. Conclusion

As a quick conclusion of this section, we observed the following facts:

- The three first arguments against EDO automatically disappear if we consider the nucleus not to be a point, i.e. the Coulomb potential is corrected in order to have finite value inside the nucleus.
- Such a corrected Coulomb potential without singular point at the origin is necessary to accept EDO solutions of Dirac equation. Moreover, considering a nucleus with finite dimension has real physical meaning, especially if we look for deep orbit solutions, for which the mean radius is close to nuclear dimensions.

3. The Deep Orbits obtained as Solutions of Relativistic Equations

First, we quickly recall a specific work [3] on deep orbits, named Dirac Deep Levels (DDLs), as solutions of the relativistic Schrödinger and of the Dirac equations, which presented the most complete solution until recently. These solutions include an infinite family of DDL solutions for hydrogen-like atoms. Moreover, as these solutions were obtained by full analytic methods, the algebraic expressions of the energy levels point out an important fact: Special Relativity is essential to actually obtain deep orbits with high binding energy (in absolute value). This point is developed in Section 4. Next, we recall a second work [4] of the same authors, on solutions of Dirac equation for hydrogen-like atoms with a corrected potential near the nucleus. Then we report the results of a recent and complete analysis of this second work, with further developments and open questions. This analysis was required because of some criticism about the method used.

3.1. First results of Maly and Va'vra on “DDLs”

3.1.1. EDO obtained by using the relativistic Schrödinger equation

Maly and Va'vra consider the radial equation in the form given in ([23], 51.15):

$$\frac{1}{\rho^2} \frac{d}{d\rho} \left(\rho^2 \frac{dR}{d\rho} \right) + \left[\frac{\lambda}{\rho} - \frac{1}{4} - \frac{l(l+1) - Z\alpha^2}{\rho^2} \right] R = 0. \quad (1)$$

They introduce an ansatz $R(\rho) = \rho^s e^{-\frac{\rho}{\lambda}} L(\rho)$ in the radial equation, where $L(\rho)$ is a series of powers of ρ , s is a real parameter, and ρ is a real numerical parameter, without physical dimension but proportional to the radius r . Then, one can show that the eigenvalue energy E of the Hamiltonian is defined by the following expression, which is in fact the Sommerfeld relation:

$$E = mc^2 \left[1 + \left(\frac{(Z\alpha)^2}{\lambda^2} \right) \right]^{-1/2}, \quad (2)$$

where we recognize parameters λ and α of the prior equation. They are without dimension, but we have to note that α ($\sim 1/137$) is the coupling constant; for the hydrogen atom, we have $Z = 1$, that we consider hereafter.

Two conditions must be satisfied for obtaining convergence of the series $L(\rho): s(s+1) + \alpha^2 - l(l+1) = 0$, where l is the angular momentum quantum number, and $\lambda = n' + s + 1$, where n' is an integer number ≥ 0 . The first condition, a quadratic equation, has two roots: $s = -1/2 \pm [(l + 1/2)^2 - \alpha^2]^{1/2}$.

The usual regular solution for electronic energy levels is obtained by taking a positive sign in the expression for the root s , while a negative sign yields the so-called anomalous solution, giving the following expression for the energy levels:

$$E = mc^2 \left[1 + \frac{\alpha^2}{\left(n' + \frac{1}{2} - \left[(l + \frac{1}{2})^2 - \alpha^2 \right]^{1/2} \right)} \right]^{-1/2}, \quad (3)$$

where n' is the radial quantum number and l is the angular momentum quantum number.

The values represented by E are the total energy of the electronic orbitals. The corresponding binding energies BE are defined as $BE = E - mc^2$, which values have the usual negative sign.

In previous works, we showed that all energy values given by the expression of E do not correspond to deep orbits, but only the ones satisfying the relation $n' = l$, i.e. *equality between the radial quantum number and the angular quantum number*. Indeed, this condition allows one to drastically reduce the expression for λ :

From $\lambda = n' + s + 1$, $s = -\frac{1}{2} + [(l + \frac{1}{2})^2 - \alpha^2]^{1/2}$ and $n' = l$, we can deduce $\lambda \sim \alpha^2/(2l+1)$, as $\alpha \ll 1$.

Next, by carrying this into the expression of E , one can deduce $E \sim mc^2 \alpha / (2l+1)$. So, for all values of l , including the case $l = 0$, we have $E \ll mc^2$. Under these conditions, the binding energy $|BE|$ is very high and that means the orbit is very deep. There is an infinite family of these very deep energy levels with $|BE| > 507$ keV. Moreover, when the condition $n' = l$ is satisfied, we can note the following fact: if l (and thus also n') increases, then E decreases, which implies $|BE|$ increases.

So, when the radial number increases, the electron is more strongly bound to the nucleus, which is the opposite behavior of the atomic orbitals. As noted in Section 5.1, the coupling constant α exists in only the relativistic equations.

3.1.2. EDO obtained by using the Dirac equation

Maly and Va'vra refer to and use the method developed in [23], by starting with the system of radial equations obtained after separating the variables in spherical coordinates. We recall the Dirac equation, essentially relativistic since built from the relativistic expression of the total energy, has the following form in a central Coulomb potential:

$$(i\hbar\partial_t + i\hbar c \alpha \cdot \nabla - \beta mc^2 - V) \Psi(t, \mathbf{x})$$

where α and β represent the Dirac matrices, and α is in fact a 3-vector of 4×4 matrices built from the Pauli matrices. Here, V is the Coulomb potential, defined by $-e^2/r$.

During the solution process of the system of radial equations by using an ansatz, a condition on a parameter s occurs as an exponent. This condition in the ansatz, like the one appearing in the Schrödinger equation, as seen above, is the following: $s = \pm (k^2 - \alpha^2)^{1/2}$, where the scalar α again represents the coupling constant (do not confuse alpha with the Dirac matrices representation above). Also, as in Section 3.2.1, if taking the positive sign in the expression of s , one has the usual “regular” solutions for energy levels, then with the negative sign, one has the so-called “anomalous” solutions.

The expression obtained for the energy levels is the following:

$$E = mc^2 \left[1 + \frac{\alpha^2}{(n' + s)^2} \right]^{-1/2}. \quad (4)$$

We note this expression again has a form equivalent to the Sommerfeld relation, but where the parameter s has an expression slightly different from the one in Section 3.1.1. It contains the specific Dirac angular quantum number k instead of the usual orbital quantum number l .

If we consider the anomalous solutions, by choosing the negative sign s in the expression of E , this one reads:

$$E = mc^2 \left[1 + \frac{\alpha^2}{\left(n' - \sqrt{(k^2 - \alpha^2)} \right)^2} \right]^{-1/2}. \quad (5)$$

In this expression, n' is again the radial number, while k is the Dirac angular number which can take any integer value $\neq 0$. But hereafter, as k is involved everywhere in absolute value, we suppose $k > 0$. As in the case of the relativistic Schrödinger equation, all solutions do not correspond to deep orbits, but only the ones satisfying the relation $n' = k$, i.e. *equality between the radial quantum number and the Dirac angular quantum number*. Indeed, we can see that if $n' = k$, the sub-expression D of the total energy E , $D = n' - (k^2 - \alpha^2)^{1/2}$ becomes $D = k - (k^2 - \alpha^2)^{1/2}$, which is very small since $D \sim \alpha^2/2k$, and $E \sim mc^2 \alpha/2k$. Then $|\text{BE}| \sim mc^2 (1 - \alpha/2k)$ and $|\text{BE}|$ is close to the rest mass energy of the electron, 511 keV. Note that since k cannot be 0, then neither can n' .

From the expression of $|\text{BE}|$, we can deduce a result similar to the binding energies of the EDOs solutions of the relativistic Schrödinger equation. Under the condition $n' = k$ (necessary condition for EDOs), *when k increases, the absolute value $|\text{BE}|$ of the binding energy increases*. This means that, as the angular momentum k increases, *the electron is more strongly bound to the nucleus*. So, a natural question arose: what about the mean radius? Or more precisely, how does the mean value of the orbit radius progress as n' increases and tends to infinity? One could guess a partial answer to this question, while reading between the lines of the second work of Maly and Va'vra, which we recall in Section 3.2.

3.2. Deep orbits obtained as solutions of the Dirac equation with a corrected potential near the nucleus

In their second work [4], the authors determine the wavefunctions of EDOs, the so-called DDLs, for hydrogen-like atom solutions of the Dirac equation. They considered the nucleus not to be point-like, and thus the potential inside the nucleus is finite at the origin $r = 0$.

This requires one to carry out the following things:

- To choose a radius R_0 , the so-called matching radius, delimiting two spatial domains: an outside one, where the potential is correctly expressed by the usual Coulomb potential, an inside, where the potential cannot be expressed by the Coulomb potential and which no longer has a singular point at $r = 0$. Of course, this choice may seem arbitrary, but it takes physical meaning if one chooses a value R_0 close to the charge radius R_c of the nucleus. For example, for hydrogen H atom, the nucleus is reduced to one proton and this one has $R_c \sim 0.875$ F from CODATA [24]. So one can reasonably choose $1 \text{ F} < R_0 < 1.3 \text{ F}$.
- To choose a suitable expression for the inside potential. It is again an arbitrary point, but we observed (see further in Section 4.2.2) that this choice has weak influence on the numerical results that interest us, especially the value of mean radius as function of k .

- To satisfy continuity conditions at the matching radius R_0 for connecting the inside and outside potentials.
- Solve the system of radial equations for the outside potential, i.e. Coulomb potential, that gives the outside solution composed of two components: functions f_o and g_o .
- Solve the system for the chosen inside potential, that gives the inside solution composed of two components: functions f_i and g_i .
- To satisfy continuity conditions while connecting the respective components of inside and outside solutions.

In their work, the authors made the following choices and processes:

- For the matching radius, the value is not explicitly given in their paper, but from a figure, it seems $R_0 \sim 1.2 F$, but perhaps slightly smaller than this value.
- The chosen inside potential $V(r)$ has the following expression:

$$V(r) = - \left[\frac{3}{2} - \frac{1}{2} \left(\frac{r^2}{R_0^2} \right) \right] \frac{Ze^2}{R_0} + \beta_0. \quad (6)$$

- One can be surprised by the presence of the additive constant β_0 ; if it is not null, the continuity condition is not satisfied by the inside and outside potentials. Nevertheless, potential is relative and we will see further a possible usefulness of this constant. For the time being, we shall consider it is null.
- For finding the outside solutions f_o and g_o , they use the computation method of [25], a completely analytic method, where both components of the radial wavefunction, respectively, include functions F_1 and G_1 , expressed by means of confluent hyper-geometrical series.
- For the inside solutions, they choose an ansatz with two components, having the following form:

$$g_i = Ar^{S_i-1} G_2(r), \quad (7a)$$

$$f_i = iBr^{S_i-1} F_2(r). \quad (7b)$$

Where $G_2(r)$ and $F_2(r)$ are power series. However, one may consider approximations by polynomials, by taking into account the following facts:

- f_i and g_i must be defined for $r < R_0$.
- For $r < R_0$, very small, the power terms vanish when the degree increases.

The classical method used, after inserting the ansatz into the equations, allows one to determine the exponent s_i and the polynomial coefficients in order to obtain the solutions.

Nevertheless, it seems the cited paper was incomplete and useful information was in another paper of the same authors, referenced as “to be published” but never published. Indeed, the chosen ansatz does not allow one to connect both respective components of inside and outside solution, while respecting continuity conditions. A complete analysis of this problem, and the way we resolve it, is developed in [8]. Here, we simply recall the problem was resolved by taking a more complex ansatz including an additional real parameter λ necessary to connect in a suitable manner the inside and outside functions. In our ansatz, the series/polynomials have the following form:

$$G_2(r) = a_1(\lambda r) + a_2(\lambda r)^2 + a_3(\lambda r)^3 + \dots \quad \text{and} \quad F_2(r) = b_1(\lambda r) + b_2(r)^2 + b_3(\lambda r)^3 + \dots \quad (8)$$

The matching process leads to solving a system of two linear equations with two unknown variables, λ , involved in the inside solutions, and a multiplicative coefficient involved in the outside solutions; we showed the system always has solutions for any value of k , which determines energy levels. Moreover, we verified that the orthogonality criterion and boundary conditions are satisfied by each “global solution” formed by the respective outside and the inside solutions.

4. Results obtained by Computations of the DDL Wavefunctions for Modified Potentials, further Developments and Discussion

4.1. Computation process for orbit mean radii

The value of the mean radius is an essential parameter for the LENR, since the range of the strong nuclear force is on the order of femto-meters (fm or F) and quickly decreases at distances $> \sim 3\text{--}5\text{ F}$. The mean radius of its electron orbitals determines the “size” of the atom and the value of the repulsive radius of an atom. This radius can be estimated approximately [4] to be the value where the electron probability density drops to 1/10 of its peak value.

Summarily, the computation process for mean orbit radius *for a given value of k* includes the following steps:

- To determine both couples (f_o, g_o) and (f_i, g_i) of respective outside and inside solutions. At this step, the four functions f_o, g_o, f_i , and g_i include parameters still to be determined
- To connect them in suitable manner and by satisfying the continuity conditions, in order to obtain a couple of global wavefunction solutions (F, G) . During this step, the unknown parameters included in the initial functions f_o, g_o, f_i , and g_i are fixed. The functions thereby completely defined can be noted F_o, G_o, F_i , and G_i .
- To compute the normalization constant N by using the following formula:

$$1/N = \int_0^{R_0} ElD_i dr + \int_{R_0}^{+\infty} ElD_o dr, \quad (9)$$

where ElD_i represents the electron probability density corresponding to the couple of inside functions (F_i, G_i) :

$$ElD_i = 4\pi r^2(|F_i|^2 + |G_i|^2) \quad (10)$$

and likewise ElD_o for the outside functions

$$ElD_o = 4\pi r^2(|F_o|^2 + |G_o|^2). \quad (11)$$

- Finally, to compute the mean radius $\langle r \rangle$ by using the following formula:

$$\langle r \rangle = N \left[\int_0^{R_0} r ElD_i dr + \int_{R_0}^{+\infty} r ElD_o dr \right]. \quad (12)$$

Now we have to note that, in principle, the numerical results of $\langle r \rangle$ should depend on the following preliminary choices:

- The choice of the matching radius R_0 : even if its value is reasonably chosen to fit physical data, such as the charge radius of the considered nucleus, it is rather fuzzy.
- The choice of the inside (nuclear) potential: apart from a common condition requiring it be finite at $r = 0$, there are multiple possibilities, each depending on modeling and approximations for the nuclear structure. Two of the most used examples are the following:
- A simple constant potential equal to the value of the Coulomb potential at the surface of the nucleus and corresponding to an uniformly charged empty spherical shell.

- The potential function defined by the expression written in the previous sub-section and corresponding to a uniformly charged solid sphere.

Nevertheless, one can consider more complex potentials, or intermediate forms of both previous ones.

- A more subtle choice, related to the precision of the inside functions, and depending on the approximation degree chosen for the polynomials of the ansatz, i.e. the power degrees of these polynomials.
- Of course, the choice of the considered hydrogen-like atom.

4.2. Numerical results

We carried out several series of computations for different choices listed in Section 4.1.

4.2.1. Results obtained from parameters near those of Maly and Va'vra

Here we first give the values of $\langle r \rangle$ computed for hydrogen atom H, while following approximately the choices of Maly and Va'vra:

- $R_0 = 1.2$ F.
- A nuclear potential defined by the expression given in Section 4.1 but assuming $\beta_0 = 0$. It approximates the proton by a uniformly charged solid sphere.
- The polynomials of our ansatz have degree 6, while the ones of M&V, for a simpler ansatz, have degree 5.

Under these conditions, we have the following values $\langle r \rangle$ for the mean orbit radii for different k values:

- $k = 1$, $\langle r \rangle \sim 6.62$ F,
- $k = 2$, $\langle r \rangle \sim 1.65$ F,
- $k = 3$, $\langle r \rangle \sim 1.39$ F,
- $k = 10$, $\langle r \rangle \sim 1.22$ F,
- $k = 20$, $\langle r \rangle \sim 1.20$ F.

The computed values are given with only three digits for high values of k , on account of uncertainties on the considered method.

We can note the following facts deduced from these computation:

- We obtain values of *the same size order* as that in [4], while we used *a method which is likely different*. So, we have a good confirmation of the prior results. Those authors indicate explicitly the value 5.2 F for the DDL atom H for $k = 1$, and they give only this case for atomic H.
- The mean radius *decreases* when k *increases*, which is consistent with the fact that the binding energy in absolute value $|BE|$ *increases* when k increases, as expected in [6].
- After an abrupt fall between the value for $k = 1$ and the one for $k = 2$, the value of the radius *asymptotically tends to the value of the matching radius* 1.2 F. One can think there is an actual “accumulation sphere” at $r \sim R_0$, for the DDL orbits corresponding to $k \geq 20$, and these are indistinguishable.

In Fig. 1, we plot the near-nucleus normalized electron probability density functions (NEPD) for $k = 1, 2$, and 3.

4.2.2. Varying the parameters

Here we only report conclusions about results described in detail in [8].

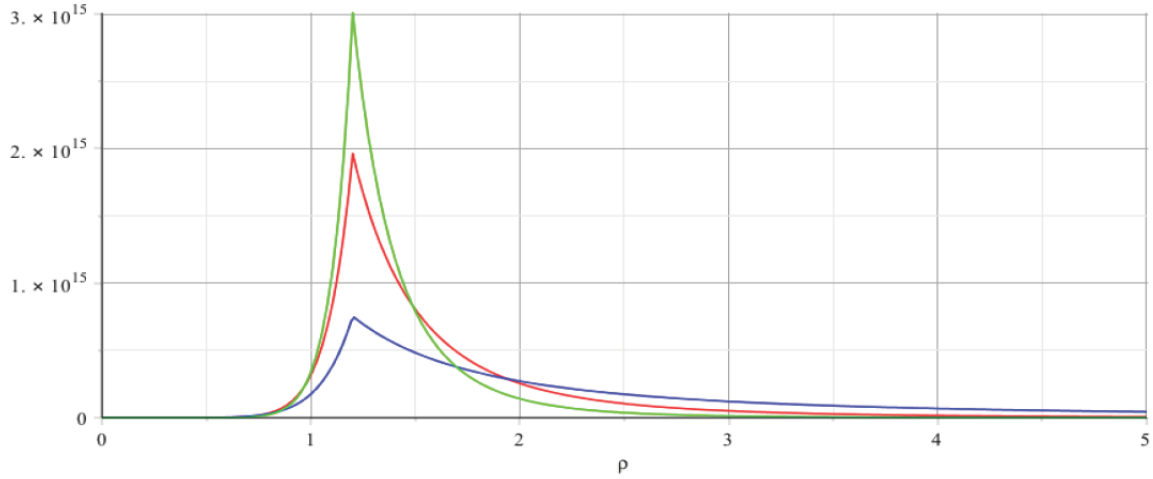


Figure 1. NEPD, for $k=1$ (blue), $k=2$ (red); $k=3$ (green). The radius ρ is in F.

- With different values for R_0 , we obtain the *same kind of progression* when k increases, i.e. $\langle r \rangle$ *decreases* when k increases and $\langle r \rangle$ still *asymptotically tends* to R_0 .
- We also note a near-linear shift of the values of $\langle r \rangle$ in the same direction as the shift of R_0 . This effect is most important for the first values of k . For example, with $R_0 = 0.78$ F (not a reasonable value for atom H but only a style exercise) we obtain $\langle r \rangle \sim 4.6$ F for $k = 1$; and with $R_0 = 2.8$ F, which is reasonable for Li6 atom (it has charge radius $R_c \sim 2.59$ with $Z = 3$), we have $\langle r \rangle \sim 13.4$ F for $k = 1$.
- When taking polynomials of higher degree, we have still the same progression, but with slightly smaller values of $\langle r \rangle$ for the smallest values of k and then there is convergence.
- Surprisingly, a change of the nuclear potential has *almost no influence on the results*. Of course, we tested reasonable changes, i.e. such that the potential does not increase (in absolute value) for $r < R_0$. More precisely, we defined a parameterized potential, which can be fixed in intermediate forms between the potential previously tested and a constant potential for $r < R_0$, by the following expression:

$$V(r) = e^2(-\beta_1 + \beta_2 r^2), \quad \text{with } \beta_1 = (2 + \varepsilon)/2R_0 \text{ and } \beta_2 = \varepsilon/2R_0^3. \quad (13)$$

In fact, one can think the “inside” (i.e. nuclear) potential has only a very weak influence on the results, because the electron probability density inside the nucleus has a weak weight.

In conclusion:

- The values of the mean radius $\langle r \rangle$ are dependent on the angular number k .
- For any considered changes of the parameters, the *progression* of the values when k increases is *always the same*: the values of $\langle r \rangle$ decrease and tend to the value of the matching radius.
- The values of $\langle r \rangle$, globally, are nearly independent of the parameters except for the value of the matching radius R_0 . This seems logical from a physical point of view, when recognizing the charge radius of the nucleus. Nevertheless, the mathematical method introduces an intrinsic degree of arbitrariness in the choice of R_0 that cannot be eliminated.

4.3. Discussion on some criticisms about the considered method, and attempts to correct discrepancies

Here we consider two questions which arose about the method of corrected potential.

4.3.1. *Question about the dependence of the inside solutions on the nuclear charge potential, and the coherence of the values of energies*

On the one hand, we note a subtle criticism [26] about some lack of dependence of the solutions on the nuclear potential. By computation, we verified this lack of dependence (as indicated previously). On the other hand, if we compute, in an approximate manner, the value of binding energies BE corresponding to the computed values of the mean radius, we find some discrepancy.

For this question, we consider as test values, the values of mean radii $\langle r \rangle$ given at the beginning of the Section 4.2.1. for $k=1,2,3$, and 10. Effectively, if we compute binding energies corresponding to these radius values, while considering the simplified hypothesis where the electron orbits are quasi-circular, we obtain the following values of BE: –97, –275, –301, and –320 keV corresponding to radius values 6.62, 1.65, 1.39, and 1.22 F, respectively.

These values have been computed by using the relativistic virial theorem [27,28], with the following relations:

$$PE = -\gamma m v^2 = -e^2/r, \quad KE = mc^2(\gamma - 1), \quad BE = KE + PE, \quad \text{Total energy } E = mc^2 + BE.$$

Of course, these calculations are carried out in a relativistic semi-classical way, but they give size orders having important shifts with respect to the starting values of BE for DDLs orbits, which are the following: –509, –510, –510.4, and –510.8 keV with the same sequence. A possible reason is related to method of corrected potential. On the one hand, the inside functions are directly dependent on the nuclear potential $V(r)$, because this potential is inserted into the Dirac equation system to be solved. On the other hand, they involve DDL original energy values E (i.e. the ones indicated just above) inserted into the equation system, and so they indirectly depend on the Coulomb potential.

To correct this discrepancy, we use a method of iterative computation with convergence, which is precisely described in [8]. Summarily, at each computation cycle, one inserts energies, computed from previously computed radii, into the equations, until they reach a fixed point. We carry out this whole process for each $k = 1, 2, 3$, and 10 with following results:

- for $k = 2, 3$, and 10, the process reaches a fixed value at the first computation cycle, and we obtain the values of BE –275, –301, and –320 keV for radii 1.65, 1.39, and 1.22, respectively.
- for $k = 1$, as the successive values approximately behave as geometrical series; one can say there is convergence at radius value ~ 12 F, that would give BE ~ -56 keV.

In conclusion, we tend to think the actual DDLs for a modified potential will correspond to the results of this convergence process, which provides energy coherence and improved dependence of the inside functions on nuclear potential.

4.3.2. *Question about a discontinuity of the derivative of solutions*

A recent criticism was reported by a colleague, concerning the discontinuity of the derivative of the wave functions at the matching radius. Indeed, in the method for connecting the inside and outside functions at R_0 , for Dirac equation, one satisfies continuity only for the functions, but not for their derivatives. This seems to be a common practice, as the Dirac equation is a first-order differential equation. We can observe, in Fig. 1, that the electron probability functions also have discontinuities of the derivative at $\rho = 1.2$ F, as a consequence of the derivative discontinuity of the wavefunctions.

The criticism about this fact is the following: as the left-derivative and the right-derivative of the solutions are not equal at R_0 , one can deduce, *in reporting their values into the radial equations*, that the potential seems discontinuous at R_0 . This is equivalent to supposing an additional virtual potential ΔP at R_0 , creating a well or a barrier according the sign of ΔP . The author of this criticism claimed that the discontinuity and the virtual potential ΔP are needed for the existence of EDO.

One may ask why this happens, because if the inside and outside functions are solutions of the equations, the continuity of the derivatives should be automatically satisfied. Nevertheless, we must not forget that the inside solutions are obtained by polynomial approximations, which are less and less good when r increases and tends to R_0 . So the discontinuity, as well as the ghost potential, is actually a simple artifact due to technical imperfections of the method of corrected potential:

- There are not enough free parameters in the inside/outside solutions to satisfy *in the same time* (needed since the components f and g are coupled in the radial equation system) the continuity of both components f , g and the continuity of their derivative. The used ansatz (Section 3.2) allows us to satisfy only two equations, but not four equations required for continuity and derivatives.
- The polynomials approximations do not allow us to obtain the continuity of the derivatives at R_0 .

We can say the discontinuity of the wavefunctions has no relation with the existence of EDOs, since it was obtained as solutions of the Dirac equation with pure Coulomb potential. Wavefunctions with modified finite potential are needed only to satisfy mathematical properties (see Section 2) and to compute the mean radii $\langle r \rangle$ of orbits in a more realistic context (i.e., where the nucleus has dimension and the potential is finite). Nevertheless, we wanted to look for possible ways to study/correct this imperfection, while observing in all our computations of normalization constants and $\langle r \rangle$ (see Section 4.3.1) that the components of g , both the inside function g_i and the outside one g_o , dominate. This dominance of g over f can even reach several orders of magnitude for the outside functions when k increases.

So, to compute the mean radius $\langle r \rangle$ with the only largest component yields results close to the results with both components. Then we carried out numerous computations in various ways: e.g. to use the additive parameter β_0 (indicated in Section 3.2) as an additive potential to balance the virtual potential ΔP for the largest component, or to satisfy continuity and derivative continuity for this component. These computations always give results close to the ones indicated in the previous section.

As an example, in Fig. 2, we plotted a zoom of the large component of the wavefunction, satisfying both continuity and derivative continuity, with $k = 2$. For this one, we obtained 1.36 F instead of 1.6 F for the original solution. Of

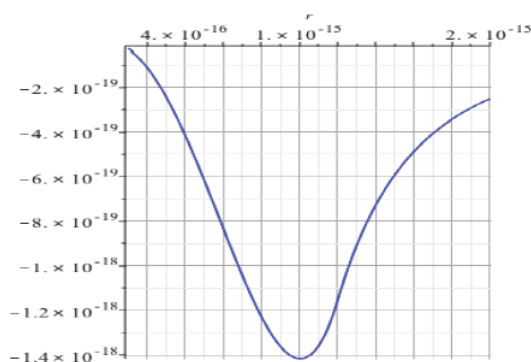


Figure 2. Large component g of the adjusted wavefunction for $k = 2$ and $R_0 = 1.2$ F.

course, it is an approximation since the computation was made only by using the component g . As a conclusion, we think it is not useful to look for a more complex method to resolve this question.

5. Why Special Relativity is needed to obtain EDOs with High Binding Energy

In previous works, we observe that non-relativistic equations give singular solutions, but these do not correspond to orbits with high binding energy (in absolute value). A physical reason is that an electron in a deep orbit is necessarily relativistic. So, it is more logical to use relativistic equations to find EDOs.

We also observed a pure mathematical reason which allows us to sort the EDO among the singular solutions of a relativistic equation, when we have analytic solutions at our disposal with energy levels E determined by an algebraic expression. Under these conditions, we can clearly see EDOs are obtained when a sub-expression, easily identifiable (see Section 3), can be drastically reduced. We saw such reductions are obtained by equating the radial number n' with the involved angular number (l or k). One can wonder if there is not a deeper reason behind this pure algebraic fact, in particular a reason having more physical meaning.

We have found such a deeper reason, first by comparing the relativistic version of the Schrödinger equation with its classical non-relativistic version and then by recognizing a relativistic correction to the potential, which is not taken into account for the usual atomic orbits because it is too weak at these energy levels. We have developed a complete analysis of this question in a paper [29] not yet published. Here we report only some essential elements and conclusion of this analysis.

5.1. Role and meaning of a relativistic parameter in the relativistic Schrödinger equation

The Dirac equation is essentially relativistic. On the other hand, as the Schrödinger equation has two versions, relativistic and non-relativistic, it is very easy to find parameters that make a difference. We can see that there is *one* parameter, which addresses our question and gives actual meaning to the involvement of relativity in EDOs.

We give both following versions of Schrödinger equations for the hydrogen atom, as extracted from [23]:

$$\frac{1}{\rho^2} \frac{d}{d\rho} \left(\rho^2 \frac{dR}{d\rho} \right) + \left[\frac{\lambda}{\rho} - \frac{1}{4} - \frac{l(l+1) - \alpha^2}{\rho^2} \right] R = 0, \quad (14)$$

$$\frac{1}{\rho^2} \frac{d}{d\rho} \left(\rho^2 \frac{dR}{d\rho} \right) + \left[\frac{\lambda'}{\rho} - \frac{1}{4} - \frac{l(l+1)}{\rho^2} \right] R = 0. \quad (15)$$

The former is the relativistic one, already indicated in Section 3.1.1, while the latter is the non-relativistic one. They are expressed in terms of the dimensionless variable ρ for the radius, and R is the radial function, depending on ρ . We can observe that they are almost the same expression, except for the occurrence of an additional parameter, the coupling constant α , in the relativistic version. In [23] the equation contains the symbol γ instead of α , for a possible generalization at any atom with $\gamma = Z\alpha$. Of course, $\lambda \neq \lambda'$ and the transformation of the initial radius r into the dimensionless variable is not the same for both equations

5.2. The term α^2 is the source of EDO solutions

We already saw, in Section 3.1.1, that the energy levels are given by the following expression

$$E = mc^2(1 + \alpha^2/\lambda^2)^{-1/2}. \quad (16)$$

We also noted the EDO solutions are given by inserting $s = -\frac{1}{2} - [(l + \frac{1}{2})^{-1} \alpha^2]^{\frac{1}{2}}$ in the ansatz used for finding the solutions, since it provides a total energy of $E \sim mc^2 \alpha / (2l+1)$, when $n' = l$, and then a very high binding energy $|\text{BE}| = mc^2 [1 - \alpha / (2l+1)]$, where the second term is $\ll 1$. The term α^2 occurring in the expression of E above directly comes from the one occurring in the relativistic equation.

It is not possible to set $n' = l$ in the case of the *non-relativistic equation*, where we recall that the singular solutions are obtained when taking $s = -(l+1)$. Here, the parameter λ' has to satisfy the condition $\lambda' = n' + s + 1$, for all types of solutions, which gives $\lambda' = n' - l$ for the singular ones. As the energy levels are given by $E = -mc^2 \alpha^2 / 2\lambda'^2$, one cannot reduce the expression for E by making $n' = l$, which would lead to $\lambda' = 0$ and thus to a singularity in the non-relativistic E .

5.3. What does the occurrence of α^2 mean?

The key to the answer is the fact the relativistic equation is built from the relativistic expression of total energy in free space $E^2 = c^2 \mathbf{p}^2 + m^2 c^4$, where \mathbf{p} is the momentum vector. Next one introduces an electromagnetic field in covariant form into the expression of E , and finally, since the nuclear Coulomb potential has spherical symmetry, one can write $(E - V)^2 = c^2 \mathbf{p}^2 + m^2 c^4$, where V is the Coulomb potential depending on the radius r . Afterwards, the expression $(E - V)^2 - m^2 c^4$, developed into $E^2 - m^2 c^4 - 2VE + V^2$, gives rise to several energy factors during the process of the Schrödinger building.

For example, the term λ/ρ occurring in the equation, and proportional to the Coulomb potential energy V , comes from $2VE$. However, it is the term γ^2/ρ^2 , *distinctive in the relativistic equation*, which interests us. It comes from and is proportional to V^2 . Moreover the parameter λ , used while building the dimensionless equation (14), is defined by $\lambda = 2E\alpha/\hbar c\varepsilon$ with $\varepsilon = [4(m^2 c^4 - E^2)/\hbar^2 c^2]^{1/2}$ one has $\lambda > 0$. By looking at this equation, one can observe the term α^2/ρ^2 , greater than zero and proportional V^2 , is added to the term λ/ρ , which is greater than zero and proportional to V .

So, we find the real meaning of the occurrence of α^2 in Eq. (14) as cause of the existence of EDOs. It corresponds to a *dynamic relativistic correction to the Coulomb potential energy* V in the form of a term proportional to V^2 , which strengthens the static potential energy V .

Of course, the Dirac equation leads also to the same relativistic quadratic correction of the static potential V , but less directly visible than for the Klein-Gordon (or relativistic Schrödinger) equation. The general form of this correction (see e.g. [30,31]), but neglecting the centrifugal barrier paper, leads to the following effective “dynamic” potential:

$$V_{\text{eff}} = V(E/mc^2) - V^2/2mc^2. \quad (17)$$

Note that in the case of a relativistic electron, one can show $V_{\text{eff}} = \gamma V + V^2/2mc^2$, where γ denotes the well-known relativistic coefficient, i.e. $\gamma = (1 - v^2/c^2)^{-1/2}$.

Note also that, while looking at both expressions of V_{eff} given above, it is not clearly visible that one always has $|V_{\text{eff}}| > |V|$, i.e. a strengthening of the “normal” Coulomb potential. However, physically, since potential is an integral of the Coulomb force that increases as the electric-field lines of both the electron and central potential are relativistically compressed (strengthened), one would expect it to increase. Where the (effective) energy of the increased potential comes from and how it can exceed the static potential energy (normally) used to determine the invariant total system energy is another discussion.

Nevertheless, we showed in [29] that, at least in the case of quasi-circular orbits, we have the following result:

- One always has $|V_{\text{eff}}| > |V|$ and V_{eff} is attractive (a negative value),
- $|V_{\text{eff}}|$ quickly increases as a function of $|V|$, with a parabolic behavior in $|V|^2$ when $|V| \rightarrow +\infty$.

5.4. Computation of V_{eff} in the case of EDOs

Again with the quasi-circular orbits hypothesis, we computed the values of V_{eff} for the values of mean radii $\langle r \rangle$ given in Section 4.2.1. for EDOs orbits with $k = 1, 2, 3$, and 10 and assuming $R_0 = 1.2 F$.

We have the following results for V_{eff} , where we indicate, at the same time, the values of $\langle r \rangle$, V , γ , $\Delta V = |V_{\text{eff}} - V|$, and the kinetic energy KE:

- $k = 1$, $\langle r \rangle \sim 6.6 F$, $\gamma \sim 1.2$, $V \sim -218 \text{ keV}$, $V_{\text{eff}} \sim -222 \text{ keV}$, $\Delta V \sim 4 \text{ keV}$, $\text{KE} \sim 120 \text{ keV}$,
- $k = 2$, $\langle r \rangle \sim 1.7 F$, $\gamma \sim 2.2$, $V \sim -873 \text{ keV}$, $V_{\text{eff}} \sim -1.15 \text{ MeV}$, $\Delta V \sim 277 \text{ keV}$, $\text{KE} \sim 597 \text{ keV}$,
- $k = 3$, $\langle r \rangle \sim 1.4 F$, $\gamma \sim 2.4$, $V \sim -1.04 \text{ MeV}$, $V_{\text{eff}} \sim -1.47 \text{ MeV}$, $\Delta V \sim 430 \text{ keV}$, $\text{KE} \sim 734 \text{ keV}$,
- $k = 10$, $\langle r \rangle \sim 1.2 F$, $\gamma \sim 2.7$, $V \sim -1.17 \text{ MeV}$, $V_{\text{eff}} \sim -1.79 \text{ MeV}$, $\Delta V \sim 620 \text{ keV}$, $\text{KE} \sim 854 \text{ keV}$.

Of course, value uncertainties are great, therefore the numbers are rounded for clarity.

From the results above, we can see that, when k increases and as $\langle r \rangle$ decreases, γ and $|V_{\text{eff}}|$ increase because of relativistic effects and $|V|$ increases because the circularization of the orbits allows a lower average radius in the potential minimum. We also note that the ratio $\Delta V/\text{KE}$ increases with these changes because of the non-linear relativistic effects.

So, from a physical point of view, we can think the relativistic motion of the electron strengthens its effective potential energy in the Coulomb field, and even an increasing part of the kinetic energy seems “to act” on the strengthening ΔV of the potential energy, when the velocity of the electron increases. However, the effective potential used above does not include the centrifugal barrier that also increases with both k and γ .

6. Conclusion, Open Questions, Future Works

- At this point, we have reviewed the method of corrected nuclear potential applied to the deep-orbit solutions of Maly and Va’vra, we extended the results found by those authors and we found new results concerning the general properties of the deep orbits. Indeed, on the one hand, we have confirmed the order of values of mean radii $\langle r \rangle$ given by the authors. On the other hand, while varying the computational parameters, we observed that changes of values for $\langle r \rangle$ depend on few, other than the matching radius R_0 . Even if the choice of R_0 is a little arbitrary, this dependence is logical from a physical point of view when taking into account the charge radius of the nucleus (itself essentially related to the atomic number Z and the mass number A of the atom). We observed, in particular, a weak dependence of $\langle r \rangle$ on the inside functions, i.e. the solution inside the nucleus. In fact, the weight of the inside functions is about one half that of the outside functions.
- Concerning the general properties of the deep orbits, we had previously shown that the mean radii $\langle r \rangle$ decrease asymptotically to R_0 as the angular number k increases. This leads to the binding energy (in absolute value) increasing with k .
- Considering the weak dependence of results on our parametric variations, we can say the method is rather robust, a strength of this method of corrected potential.
- We also analyzed possible weaknesses of the method, identified in some criticism and in our own observations about the energy levels corresponding to the values of $\langle r \rangle$. The question of consistent energies for the values of $\langle r \rangle$ led us to a modified computation process assuming almost circular orbits. This gives the same values of $\langle r \rangle$ for $k > 1$, but almost doubles the radius for $k = 1$. The principal changes in the results concern new values of binding energy, which are significantly smaller (in absolute value) than those for the original EDOs. We think these values, from 275 keV (for $k = 2$) to 320 keV (for $k = 10$), with a limit $\sim 320 \text{ keV}$ as $k \rightarrow \infty$, could be the actual values for EDOs. But this is still conjecture, because computations were made only with the simplified hypothesis of almost circular orbits. Anyway, we can note such modifications have

no implication for the existence of EDOs in the LENR process. Nevertheless, the lower binding energies of this computation greatly enhance the probability of populating the deep levels by near-field electromagnetic coupling of electrons in atomic orbitals with adjacent lattice nucleons and raising them to low-lying nuclear excited states.

- Another question is based on a discontinuity of the wavefunction derivatives at their matching point that leads to a virtual additive potential at R_0 . Nevertheless, while attempting to correct possible unwanted influence of this potential on the results, we observed by computation that there are no significant effects.
- Most importantly, we reveal the essential role of Special Relativity for the existence of EDOs with high binding energy due to the quadratic expression of the relativistic total energy. This leads to a dynamic correction to the original Coulomb potential and yields a noteworthy strengthening of the potential under some hypotheses. A more detailed analysis of the role of Special Relativity can be found in [29].
- Concerning open questions, the following is not yet resolved: the equality condition for radial number and angular number allows one to discriminate the true EDOs, characterized by strong binding energy, amongst the set of other singular solutions of equations, which have almost the same binding energies as the classical regular ones. In previous papers, we called these special non-EDO solutions, “pseudo-regular solutions.” In the same vein, we have not yet interpreted the meaning of these pseudo-regular solutions.
- Finally, a serious problem is still hanging over the existence of EDOs: do they respect the Heisenberg relation? Recent, but approximate, computations tend to answer yes to this question. Indeed, a first solution came from the spin-orbit interaction, which generates a very high attractive potential at the very small EDO radii. This potential exceeds that needed to provide the very high “Heisenberg kinetic energy” corresponding to electrons at these radii.
- To study the stability of EDOs, we still have to work more deeply on the properties of magnetic interactions and other possible effects near the nucleus, in order to evaluate the possible combinations of potential energies. In particular, the ones involved in the works of Vigier [32], Barut et al. [33] and Samsonenko et al. [34], and the correction to the Dirac operator due to the anomalous magnetic moment of the electron [35] might pertain.

Appendix added in Review

Up to now, we have worked on deep orbits as singular solutions of the Dirac equation, after analyzing, verifying and extending known works on this subject, such as those of Maly and Vav'ra [3,4].

Historically, the relativistic quantum mechanics for the electron became a field of quantitative science with the advent of the Dirac equations, which has subsequently been used for a very large number of applications. Indeed, many models for atoms, molecules and solids are based on many-electron generalizations of the Dirac equation. Nevertheless, we have now to take into account some known difficulties concerning this model of quantum physics. For example, where the generalization of the single-electron Schrödinger equation to the two-electron case immediately led to answers that compared well with experiment, the analogous generalization of the single-electron Dirac equation to the two-electron case led to the Brown–Ravenhall disease [36]. This problem (also referred as the continuum dissolution problem) is pointed out in virtually all works on many-electron questions. Summarily, it arises because solutions of Dirac equation form two continuums: the electron and positron ones; then, on double excitation of a pair of correlated electrons, one electron can end in the negative energy continuum (positrons), while the other lands in the positive energy continuum, the total system energy being retained. As a consequence, the number of such electron-positron states for an initial electron pair is infinite, and any energy level of the bound electron pair system is infinitely degenerate. This problem can be resolved by introducing special projection operators in the Hamiltonian to restrict it only to positive energy states, but of course one has no longer the classical “key in hand” analytic solution.

The Dirac equation includes other problems, such as e.g. the Klein paradox or also the fact, noted by Thaller [35],

that the Newton–Wigner operator (usually) taken as position observable leads to superluminal propagation.

Such problems lead us to introduce methods of quantum electrodynamics (QED) in our next works. Indeed, a critical feature in the construction of QED, which allowed a resolution for Brown–Ravenhall disease, was the complete elimination of the negative energy states for the description of electrons, and a corresponding complete elimination of the positive energy states for the description of positrons.

Moreover, QED became indispensable to continue our study, as it can take into account much subtle phenomena, such as, e.g. Lamb shift, which could be much more important near the nucleus than for atomic electrons.

Of course, as noted by Rusakova [37], the Brown–Ravenhall disease appears only in many-body cases. But the reviewer states our localized solutions of Dirac equations are in fact negative energy state solutions, after ending up analyzing such states in various ways. We think this could be a consequence of the fact the Dirac Hamiltonian is not bounded from below. As in QED, where the negative energy states are simply removed by construction from the available spectrum, the best way to resolve the question would be to try to look for deep orbits by using QED methods. One can even say that if there exists only one reason to introduce QED in our future work, it is this one.

Nevertheless, we have to recall [7] that the deep orbits, as singular solutions of Dirac equation, occur only when the angular number k and radial number n' are equal. This case, for $k = n'$, separates the positive- and negative-energy solutions. It falls on the positive-energy side. In fact there is a lot of other singular solutions: for $k > n'$, we explicitly get negative energy solutions, while for $k < n'$, we get solutions having almost the same (positive) energy levels as the regular ones (pseudo-regular solutions). As indicated in the conclusion above, we have not yet interpreted this situation, but one can think this profusion of weird solutions certainly introduces a big complication into the research of effective deep orbits.

Acknowledgement

The authors wish to thank the reviewer for bringing the problems related to the use of Dirac equation to our attention, and for his advice to continue our work. This work is supported in part by HiPi Consulting, Ashland, VA, USA; by the Science for Humanity Trust, Bangalore, India; and by the Science for Humanity Trust Inc., Tucker, GA, USA.

References

- [1] Brown, Laurie M. The idea of the neutrino, *Phys. Today* **31**(9) (1978) 23.
- [2] G.A. Miller, *Phys. Rev. Lett.* **99**, 112001 (2007) 0705.2409.
- [3] J.A. Maly and J. Va'vra, Electron transitions on deep Dirac levels I, *Fusion Sci. Technol.* **24**(3) (1993) 307–318, http://www.ans.org/pubs/journals/fst/a_30206.
- [4] J.A. Maly and J. Va'vra, Electron transitions on deep Dirac levels II, *Fusion Sci. Technol.* **27** (1) (1995) 59–70, http://www.ans.org/pubs/journals/fst/a_30350.
- [5] J. Naudts, On the hydrino state of the relativistic hydrogen atom, arXiv:physics/0507193v2.5, 2005.
- [6] J.L. Paillet and A. Meulenberg, Basis for electron deep orbits of the hydrogen atom, (ICCF-19), *19th Int. Conf. on Condensed Matter Nuclear Science*, Padua, Italy, 13–17 April 2015, *J. Condensed Matter Nucl. Sci.* **19** (2016) 230–243.
- [7] J.L. Paillet and A. Meulenberg, Arguments for the anomalous solutions of the Dirac equations, *J. Condensed Matter Nucl. Sci.* **18** (2016) 50–75.
- [8] J.L. Paillet and A. Meulenberg, Electron deep orbits of the hydrogen atom, *Proc. 11th Int. Workshop on Hydrogen Loaded Metals*, Airbus Toulouse, 15–16 Oct. 2015, preprint, <http://vixra.org/abs/1605.0099>.
- [9] A. Meulenberg, Extensions to physics: what cold fusion teaches, Special Section: Low Energy Nuclear Reactions, Section editors: M. Srinivasan, and A. Meulenberg, *Current Science* **108** (4) (2015) 499–506. <http://www.currentscience.ac.in/cs/php/feat.php?feature=Special%20Section:%20Low%20Energy%20Nuclear%20Reactions&featid=10094>.

- [10] A. Meulenberg and K.P. Sinha, Tunneling beneath the 4He^* fragmentation energy, *J. Condensed Matter Nucl. Sci.* **4** (2011) 241–255.
- [11] A. Meulenberg, From the Naught orbit to He^4 ground state, *16th Int. Conf. on Condensed Matter Nuclear Science*, Chennai, February 6–11, 2011; *J. Condensed Matter Nucl. Sci.* **10** (2013) 15–29.
- [12] A. Meulenberg and K.P. Sinha, Deep-electron orbits in Cold Fusion, *17th Int. Conf. Condensed Matter Nuclear Science*, Daejeon, South Korea, 12–17 August, 2012; *J. Condensed Matter Nucl. Sci.* **13** (2014) 368–377.
- [13] A. Meulenberg and K.P. Sinha, Deep-orbit-electron radiation emission in decay from $4\text{H}^{*}\#$ to 4He , *17th Int. Conf. Condensed Matter Nuclear Science*, Daejeon, South Korea, 12–17 August, 2012, *J. Condensed Matter Nucl. Sci.* **13** (2014), 357–368.
- [14] A. Meulenberg, Femto-atoms and transmutation, *17th Int. Conf. on Condensed Matter Nuclear Science*, Daejeon, South Korea, 12–17 August, 2012, *J. Condensed Matter Nucl. Sci.* **13** (2014) 346–357.
- [15] A. Meulenberg, Femto-helium and PdD transmutation, ICCF-18, *18th Int. Conf. on Cond. Matter Nuclear Science*, Columbia, Missouri, 25/07/2013; *J. Condensed Matter Nucl. Sci.* **15** (2015) 117–124.
- [16] K.P. Sinha and A. Meulenberg, Lochon catalyzed D–D fusion in deuterated palladium in the solid state, *National Academy of Sci. (India) Lett.* **30** (7,8) (2007) arXiv:0705.0595v1.
- [17] A. Meulenberg and K.P. Sinha, Composite model for LENR in linear defects of a lattice, ICCF-18, *18th Int. Conf. on Cond. Matter Nuclear Science*, Columbia, Missouri, 25/07/2013, Proceedings at <http://hdl.handle.net/10355/36818>.
- [18] A. Meulenberg, Pictorial description for LENR in linear defects of a lattice, ICCF-18, *18th Int. Conf. on Cond. Matter Nuclear Science*, Columbia, Missouri, 25/07/2013, *J. Condensed Matter Nucl. Sci.* **15** (2015) 106–116.
- [19] V.K. Ignatovitch, A missed solution for an atom-a gate toward cold nuclear fusion, https://www.researchgate.net/publication/259196190_ratis5.
- [20] A. de Castro, Orthogonality criterion for banishing hydrino states from standard quantum mechanics, *Phys Lett A* **369** (5) (2007) 380–383.
- [21] T. Nadareishvili and A. Khelashvili, Some problems of self-adjoint extension in the Schrödinger equation, <http://arxiv.org/pdf/0903.0234.pdf>.
- [22] N. Dombey, The hydrino and other unlikely states, arXiv:physics/0608095v1, 2006.
- [23] L.I. Schiff, *Quantum Mechanics*. 3rd Edition. Mc-Graw Hill, New York, 1968.
- [24] CODATA-2014. <http://physics.nist.gov/cuu/Constants/>.
- [25] S. Fluegge, *Practical Quantum Mechanics*, Vol. 2, Springer, Berlin, 1974.
- [26] R.T. Deck, J.G. Amar and G. Fralick, Nuclear size corrections to the energy levels of single-electron and - muon atoms, *J. Phys. B: At. Mol. Opt. Phys.* **38** (2005) 2173–2186 [27].
- [27] W. Lucha and F.F. Schöberl, Relativistic virial theorem, *Phys. Rev. Lett.* **64** (23) (1990) 2733–2735.
- [28] J. Gaite, The relativistic virial theorem and scale invariance, arXiv:1306.0722v1, *Phys-Usps* **56** (9) (2013).
- [29] J.L. Paillet and A. Meulenberg, Special relativity as explanation of the electron deep orbits, preprint, to be published in *Foundations of Physics*.
- [30] S.V. Adamenko and V.I. Vysotskii, Mechanism of synthesis of superheavy nuclei via the process of controlled electron-nuclear collapse, *Found. Phys. Lett.* **17** (3) (2004) 203–233.
- [31] S.V. Adamenko and V.I. Vysotskii, Evolution of annular self-controlled electron-nucleus collapse in condensed targets, *Found. Phys.* **34** (11) (2004) 1801–1831.
- [32] J.P. Vigiér, New hydrogen(deuterium) Bohr orbits in quantum chemistry and cold fusion processes, *Proc. ICCF4*, 1994, Hawaii, p.7-1.
- [33] A.O. Barut and J. Kraus, Solution of the Dirac equation with Coulomb and magnetic moment interactions, *J. Math. Phys.* **17**(4) (1976)506,507.
- [34] N.V. Samsonenko, D.V. Tahti and F. Ndahayo, On the Barut–Vigiér model of the hydrogen atom Physics, *Phys. Lett. A* **220** (1996) 297–301.
- [35] B. Thaller, *The Dirac Equation*, Springer, Berlin, 1992.
- [36] G.E. Brown and D.G. Ravenhall, *Proc. Roy. Soc. Lond. A* **208** (1951) 552.
- [37] Irina L. Rusakova, Yuriy Yu. Rusakov and Leonid B. Krivdin, Theoretical grounds of relativistic methods for calculation of spin–spin coupling constants in nuclear magnetic resonance spectra, *Russian Chem. Rev.* **85**(4), (2016) 356–426.



Research Article

The Dark side of Gravity and LENR

Frederic Henry-Couannier*

Aix-Marseille Univ, CPPM, 163 Avenue De Luminy, 13009 Marseille, France

Abstract

A previous article paved the way from a dark gravity theory (DG) toward LENR. This article is intended to go beyond the conceptual foundations (which will only be briefly summarized), and to provide a more technical detailed road map. An important revision of the theory was also made necessary by the recent direct detection of gravitational waves by Ligo. Finally, justifications will be given for adopting a slightly modified view of the process that triggers the formation of micro lightning balls, those enigmatic objects being produced in association with (and arguably responsible for) LENR, as we have recently identified the key role being played by a local increase of the density of electrons by various methods including a high luminosity beam (pulse) of electrons on a target. © 2016 ISCMNS. All rights reserved. ISSN 2227-3123

Keywords: Anti-gravity, Field discontinuities, Janus field, LENR, Negative energies, Time reversal

1. Introduction

As a reminder, in this introduction we shall list the main conceptual steps toward Dark Gravity and main achievements of the theory referring the reader to our previous article [18] for a more in-depth presentation.

- In the 1970s, due to the increasing difficulties in trying to reach a coherent theory of quantum gravity, many theorists were led to doubt that the gravitational field was the metric describing the geometrical properties of space–time itself. Rather we should perhaps rehabilitate the old view of a nondynamical space–time with metric $\eta_{\mu\nu}$ beyond the field $g_{\mu\nu}$, the latter remaining merely, for all fields minimally coupled to it, the prism through which the space and time intervals (inherently nondeformable) are seen deformed.
- But all attempts toward theories involving both $g_{\mu\nu}$ and $\eta_{\mu\nu}$ to hopefully facilitate quantization, were strongly conflicting with accurate tests of the equivalence principle and were progressively abandoned. Those attempts however missed a crucial point: in presence of $\eta_{\mu\nu}$, $g_{\mu\nu}$ has a twin $\tilde{g}_{\mu\nu}$. The two being linked by

$$\tilde{g}_{\mu\nu} = \eta_{\mu\rho}\eta_{\nu\sigma} [g^{-1}]^{\rho\sigma} = [\eta^{\mu\rho}\eta^{\nu\sigma} g_{\rho\sigma}]^{-1} + \quad (1)$$

are just the two faces of a single field (no new degrees of freedom) that we called a Janus field.

*E-mail: fhenryco@yahoo.fr.

- The action (thus the equations derived from it) must be invariant under the permutation of $g_{\mu\nu}$ and $\tilde{g}_{\mu\nu}$. This is achieved by simply adding to the usual GR and SM (standard model) action, the similar action with $\tilde{g}_{\mu\nu}$ in place of $g_{\mu\nu}$ everywhere.

$$\int d^4x (\sqrt{g}R + \sqrt{\tilde{g}}\tilde{R}) + \int d^4x (\sqrt{g}L + \sqrt{\tilde{g}}\tilde{L}), \quad (2)$$

where R and \tilde{R} are the familiar Ricci scalars built from g or \tilde{g} as usual and L and \tilde{L} the Lagrangians for respectively SM F type fields propagating along $g_{\mu\nu}$ geodesics and \tilde{F} fields propagating along $\tilde{g}_{\mu\nu}$ geodesics. This theory symmetrizing the roles of $g_{\mu\nu}$ and $\tilde{g}_{\mu\nu}$ is DG.

- It results from the derived equations that the only interaction allowed between our side F fields and \tilde{F} fields of the dark side of the DG universe is Anti-gravity (readily readable from Eq. (1) involving an inverse matrix g^{-1})
- This is the only kind of theory enabling Anti-gravity (negative energy sources for gravity) in a stable way.
- A negative energy is just the energy of an ordinary field as seen from the other side of gravity. All fields living on the same side of gravity see each other as positive energy fields (but this sign is then merely a matter of convention).
- The fundamental symmetry linking the two faces of the Janus field $g_{\mu\nu}$ and $\tilde{g}_{\mu\nu}$ is actually time reversal. This is most easily checked in DG cosmological solutions but also in the gravific energy reversal when the observer changes sides under time reversal. This time reversal is really understood as a genuine discrete symmetry in a gravitational context and does not apply to our field through a general coordinate transformation.
- According special relativity alone, time reversal was the natural way to transform a positive into negative energy. However, a less obvious anti-unitary time reversal operator was elected in QFT, which avoided the regeneration of negative energies but not any removal nor reinterpretation of those states which from the beginning have been solutions of all our relativistic field equations. In DG, QFT negative energy solutions and a Unitary time reversal can now be rehabilitated.
- The well known instability issues between interacting positive and negative energy fields are trivially solved for nongravitational interactions which are forbidden between F and \tilde{F} fields. Moreover even the new anti-gravitational interaction is stable as first advocated by JP Petit [3,7,8] (no runaway), the precursor and first explorer of Dark Gravity, and more recently Hossenfelder [4].

2. Solving the Equations for a Cosmological Solution

2.1. The scalar-tensor cosmological field

For a cosmological solution, both $g_{\mu\nu}$ and $\tilde{g}_{\mu\nu}$ must be homogeneous and isotropic, and given a flat nondynamical space-time with its Minkowskian metric entering in Eq. (1), this is only possible provided the spatial curvature parameter $k = 0$ in both faces of the FRW Janus field. We leave as an open option for the future the less natural case of a static nondynamical but curved space-time in which case $g_{\mu\nu}$, $\tilde{g}_{\mu\nu}$ and the metric of space-time will share the same k and, for the scale factor, the same solutions as in the flat case since k terms will be found to cancel out from the equations. So far we just note that the already tested with good accuracy, perfect flatness of our universe, can be considered a prediction of DG (without any need for inflation) since there is no reason why the nondynamical space-time itself should be curved in DG.

The next step is to try the Janus FRW ensatz and solve the equations for the scale factor $a(t)$. One finds that only a static field can satisfy all the equations which would appear a dead end for a DG theory trying to describe the expansion history of the universe. However, it turns out that the theory is easily saved if the elements of the cosmological field are required to be tied together and cannot be varied independently. This is the case if our field

needed to describe cosmological expansion is built from a scalar Φ and we can write $g_{\mu\nu} = (-A, A, A, A) = \Phi\eta_{\mu\nu}$ and $\tilde{g}_{\mu\nu} = (-1/A, 1/A, 1/A, 1/A) = \frac{1}{\Phi}\eta_{\mu\nu}$. Quite naturally, we shall call this field a scalar-tensor Janus field.

The form taken by this homogeneous field could be further justified based on discrete space–time symmetry arguments, [2], Section 6. Moreover, we will later argue that this field has to be genetically homogeneous, i.e Φ is from birth required to be the spatially independent $\Phi(t)$, ensuring it cannot be perturbed in anyway because we will need to avoid any adverse scalar contribution to the radiation of gravitational waves.

Another independent Janus field will thus be required later to describe local gravity, a field where all elements will be allowed to vary independently as usual but then a field forced to remain asymptotically static to satisfy all the equations.

But for now, we are left with only one fundamental scalar equation to be satisfied by our scale factor $a(t) = 1/\tilde{a}(t)$ in $\Phi(t) = A(t) = a^2(t)$ instead of the two Friedman equations in GR so we avoid the equation which in case $k = 0$ in GR implies that the universe density is constrained to be the critical density. In DG, having no such constraints to be satisfied by our densities we no longer need Dark Matter to fill any missing mass at the cosmological scale. Our fundamental cosmological single equation obtained by requiring the action to be extremal under any variation of $\Phi(t) = a^2(t)$ is:

$$a^2 \frac{\ddot{a}}{a} - \tilde{a}^2 \frac{\ddot{\tilde{a}}}{\tilde{a}} = \frac{4\pi G}{3} (a^4(\rho - 3p) - \tilde{a}^4(\tilde{\rho} - 3\tilde{p})). \quad (3)$$

2.2. Cosmology

We investigated in details the solutions of this cosmological equation and have shown that DG is able to reproduce the same scale factor expansion evolution as obtained within the standard LCDM Model. This is all summarized in Fig. 1. This expansion implies that the dark side of the universe is in contraction and was already dominated by radiation

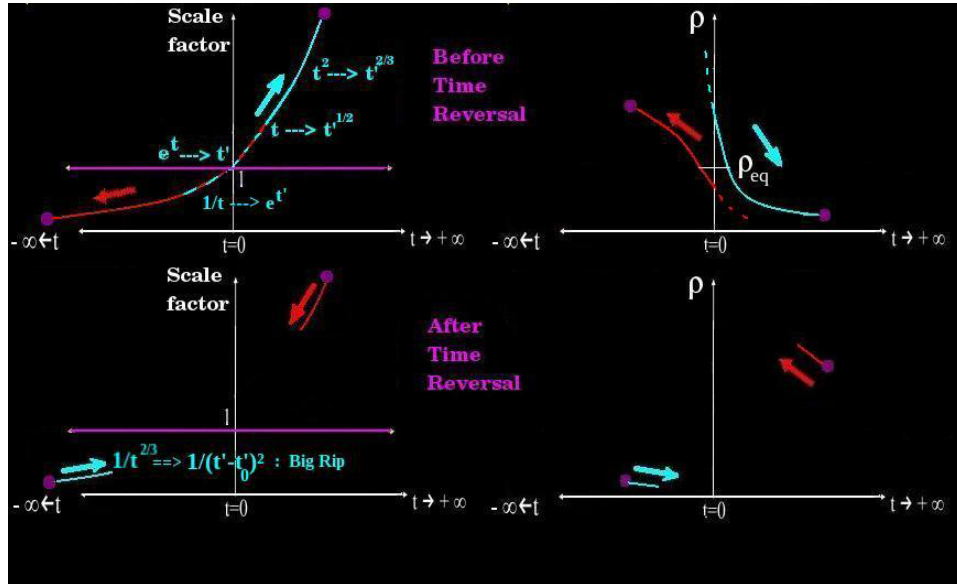


Figure 1. Evolution laws and time reversal of the conjugate universes, our side in blue.

at the time of our side nucleosynthesis. Otherwise a nonvanishing source $\tilde{\rho} - 3\tilde{p}$ from the Dark side would have implied a quite different evolution from LCDM and very different fractions for the light elements following Big-Bang Nucleosynthesis, which is completely excluded. The reason why the radiative era evolution $t'^{1/2}$ (the solutions first obtained in conformal time t are straightforwardly translated into standard cosmological time t' evolution laws) and subsequent decelerated evolution $t'^{2/3}$ in the cold era on our side are the same as in LCDM is simple: provided our side scale factor $a(t)$ dominates the inverse scale factor $\tilde{a}(t) = 1/a(t)$ and provided $\tilde{\rho} - 3\tilde{p}$ vanishes as well during our side hot era, dark side terms can be neglected in our cosmological equation which reduces to a cosmological equation known to be valid within GR (Figs. 1–3).

The very new feature of this history is that we are now also able to account for the recent acceleration of the universe without a cosmological constant in DG, assuming a discrete transition, genuine permutation of the conjugate scale factors which occurred about the transition redshift $z_{tr} = 0.7$. Such transition is a very peculiar but also very natural feature of a theory where the discrete nature of the time reversal symmetry is really accounted for. We understand that the huge discontinuous transition itself did not produce an observable effect at the time it occurred. In particular the densities are the same just before and just after the transition. This seems to conflict with the usual understanding that the densities vary when the scale factor varies, the exact behaviour being deduced from the free fall equations. However the free fall equation simply does not apply to the time reversal process itself that instantaneously exchanges the roles of the conjugate scale factors. On the contrary our current understanding is that all physical quantities (matter and radiation properties) remain the same in such transition so that in our cosmological equation (3) it is only the terms that depend explicitly on the scale factors that are modified.^a

So neither the Hubble factors (the scale factor is transformed into its inverse and at the same time the infinitesimal dt is also transformed into $-dt$ so that \dot{a}/a is invariant) nor densities did experience any discontinuity at the transition however the subsequent evolution now started to be driven by the dominant $\tilde{a}(t)$ term on the left-hand side of our cosmological equation.

On the right-hand side of our cosmological equation, let us stay open minded and consider two alternatives. The conjugate side now should have reached huge densities after contracting by a $\simeq 10^9$ factor between Big Bang Nucleosynthesis and now (remember we don't need to care about the instantaneous discontinuous permutation itself since it does not modify the densities). Thus $\tilde{\rho} - 3\tilde{p}$ still zero is normally expected in a radiation dominated phase so that $\rho - 3p \simeq \rho \propto 1/a^3(t)$ drives the evolution...

In this case our cosmological equation simplifies

$$\tilde{a}^2 \frac{\ddot{\tilde{a}}}{\tilde{a}} \propto \frac{1}{\tilde{a}}. \quad (4)$$

With solution $a(t) \propto t^{-2/3}$ which translates into an accelerated expansion regime $(t' - t'_0)^{-2}$ with a Big Rip at future time t'_0 .

Another possibility is the one represented in Fig. 2 where a mother Universe lost contact with its conjugate and split into two new baby conjugate universes about a new re-normalized η background at a reset time origin t_0 . If this happened during the cold matter dominated era (for instance between $z = 1000$ and now), this scenario is interesting because now our conjugate side universe might not be extremely different from our side since the two originated recently from a same mother. Following this scenario, right now this recently born conjugate universe can be both in

^aWe shall investigate later discontinuities in space, e.g. what happens when light or a body crosses the frontier between two regions where different regimes of the scale factor take place, one expanding and one contracting for instance. In this particular case of a discontinuity in space rather than in time, the body does not experience time reversal crossing it, so the equation of free fall applies (wave equations can always be solved in presence of potential discontinuities: forces are undefined but potential barriers and their effects are well defined, remind the square potentials of our basic QM courses) and new effects are expected that will be the subject of forthcoming sections.

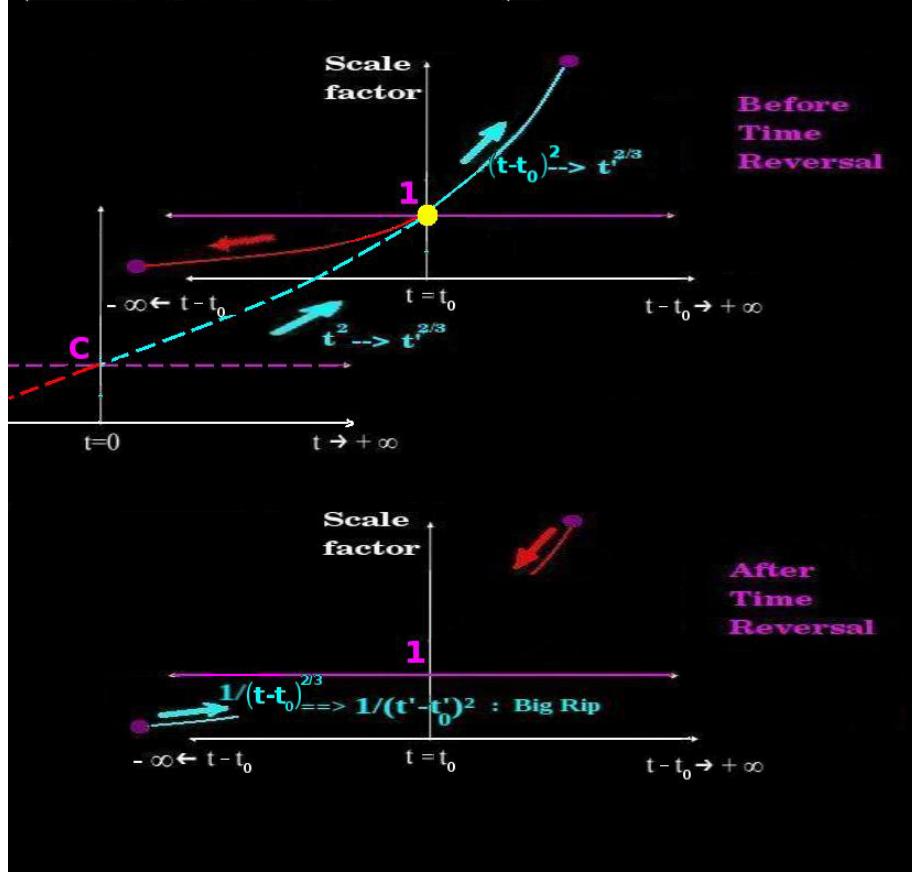


Figure 2. Universe splitting giving birth to a new couple of conjugate universes, our side in blue.

a matter dominated era or radiation dominated era if it had enough time between the yellow point where it started to contract and the purple point of time reversal in Fig. 2.

The equation of state can be such that $\tilde{\rho} - 3\tilde{p} \propto 1/(\tilde{a}^{3+\delta}(t))$ with $0 < \delta < 1$, $\delta = 0$ corresponding to a cold matter dominated era and $\delta = 1$ to a state not far from matter radiation equality. More radiation dominated (fast increasing $\delta > 1$) would eventually result again in a negligible $\tilde{\rho} - 3\tilde{p}$ so we are back to the Big Rip of our first case when our side $\rho - 3p \simeq \rho \propto 1/a^3(t)$ drives the evolution. In case $0 < \delta < 1$ the conjugate side can momentarily drive the evolution all the easier as $a^4(\rho - 3p) \ll \tilde{a}^4(\tilde{\rho} - 3\tilde{p})$ for $a(t) \ll \tilde{a}(t)$. Then our cosmological equation simplifies in a different way:

$$\tilde{a}^2 \frac{\ddot{\tilde{a}}}{\tilde{a}} \propto \tilde{a}^{1-\delta}. \quad (5)$$

With solution $a(t) \propto t^{-2/(1+\delta)}$ which translates into an accelerated expansion regime $t'^{2/(1-\delta)}$.

Constraining the age of the universe to be the same as in LCDM is the easiest way to ensure that there will be no noticeable departure between our and the LCDM cosmological history insofar as we are not looking at the fine details of the recent transition between decelerated and accelerated regime. In case of a discrete transition applying

everywhere simultaneously we could derive the following formula relating the transition redshift to the power α of the recent accelerated expansion law t'^α .

$$z_{\text{tr}} = \left(\frac{2/3 - \alpha}{1 - \alpha} \right)^\alpha - 1. \quad (6)$$

Then one could check that our predicted $\alpha = 2/(1 - \delta)$ in the second case gives $0.33 < z_{\text{tr}} < 0.78$ for $0 < \delta < 1$ in good agreement with the best current estimation $z_{\text{tr}} = 0.67 \pm 0.1$ [17]. In the first case $\alpha = -2$ gives $z_{\text{tr}} = 0.27$ which, we notice, is quite close to $z_{\text{tr}} = e^{1/3} - 1 \approx 0.4$ corresponding to a modified fictitious LCDM cosmology with a discontinuous transition between 100 % cold dark matter and 100 % Λ dominated universe.

We probably cannot assume that the transition redshifts were everywhere exactly the same due to local inhomogeneities so that integrated over large regions, the resulting transition is likely to be observed significantly smoothed by this dispersion of z_{tr} . The mean transition redshift is very sensitive to this since the LCDM very smooth transition well fits the data with $z_{\text{tr}} \approx 0.7$ while a discrete transition would imply $z_{\text{tr}} = e^{1/3} - 1 \approx 0.4$ as we already noticed.

The good agreement in the second case particularly for a small δ , seems to imply a small dispersion of z_{tr} while in the first case or radiation dominated second case a much larger dispersion implying a very progressive and smoothed transition on the mean is required, a scenario which probably will be more difficult to discriminate from the very progressive LCDM transition between matter and Lambda dominated expansion.

Another lesson of the previous analysis is that with a possible succession of time reversals and rebirths of universes, particularly if the rebirth is originating from a finite sub-region of a mother universe (maybe a giant black-hole), the equality between matter and antimatter, which presumably was a starting point, can be completely lost in a given couple of conjugate universes and the fraction of baryons over photons can also be quite arbitrary on both sides.

Notice then that when we say that the conjugate side was in a radiative era at the time of our side BBN, this does not necessarily mean that it was very dense: on the contrary it could have been a very low energy density universe where the fraction of photons over baryons was and has remained much greater than on our side.

3. Local Gravity

Another Janus field and its own separate Einstein–Hilbert (E–H) action are required to describe local gravity because it cannot be mixed with our previous cosmological scalar-tensor field in the same E–H action without reintroducing an additional unwanted equation for the latter.

We can summarize what we learned from solving the equations for this field in the isotropic case.

- Our new Janus field for local gravity can only satisfy the equations provided it is asymptotically Minkowskian (as we already noticed in Section 2). This ensures that any global evolution is exclusively driven by our previous cosmological tensor-scalar field.
- We found a couple of static isotropic conjugate solutions in vacuum of the form $g_{\mu\nu} = (B, A, A, A)$ and $\tilde{g}_{\mu\nu} = (1/B, 1/A, 1/A, 1/A)$

$$A = e^{\frac{2MG}{r}} \approx 1 + 2\frac{MG}{r} + 2\frac{M^2G^2}{r^2}, \quad (7)$$

$$B = -\frac{1}{A} = -e^{\frac{-2MG}{r}} \approx -1 + 2\frac{MG}{r} - 2\frac{M^2G^2}{r^2} + \frac{4}{3}\frac{M^3G^3}{r^3} \quad (8)$$

perfectly suited to represent the field generated outside an elementary source mass M . This is different from the GR one, though in good agreement up to Post-Newtonian order. It is straightforward to check that this Schwarzschild new solution involves no horizon: no more black hole!

- The solution also confirms that a positive mass M in the conjugate metric is seen as a negative mass $-M$ from its gravitational effect felt on our side.
- The exponential form of the metric implies that a trivial superposition principle allows us to combine the field generated by a mass M_1 and the field generated by a mass M_2 at the same place: gravity is linear in the argument of the exponential. We did not already figure out all the implications of this result which we believe is of fundamental importance. We know about great theoretical efforts that were undertaken toward a modified theory of gravity just to get this kind of solution instead of the Schwarzschild GR one [26].

4. Gravitational Waves, Sound Waves and Vacuum Energy

4.1. Gravitational waves

Let us introduce a plane wave perturbation $h_{\mu\nu}$ with its counterpart $\tilde{h}_{\mu\nu}$. Then, up to a redefinition of the gravitational constant G by a factor two (the same as for the equations of the $B = -1/A$ isotropic static field of Section 3), the linearized equations could be the same in GR and DG. Indeed, without such redefinition here we have:

$$2 \left(R_{\mu\nu}^{(1)} - \frac{1}{2} \eta_{\mu\nu} R_{\lambda}^{(1)\lambda} \right) = -8\pi G (T_{\mu\nu} - \tilde{T}_{\mu\nu}). \quad (9)$$

We know that the physical degrees of freedom for these plane waves are quadrupolar (spin 2) and could well account for the recent direct observation of gravitational waves by Ligo. The apparent problem is that this equation is also valid to second order in the perturbation $h_{\mu\nu} = -\tilde{h}_{\mu\nu}$ because one just needs to add a quadratic term $t_{\mu\nu} - \tilde{t}_{\mu\nu}$ on the right-hand side standing for the energy-momentum of the gravitational field itself which has two cancelling contributions since $t_{\mu\nu} = \tilde{t}_{\mu\nu}$ to second order in small plane wave perturbations. This does not mean that there is no wave. Indeed the Linearized Bianchi identities are still obeyed on the left-hand side and it therefore follows the local conservation law:

$$\frac{\partial}{\partial x^\mu} (T^{\mu\nu} - \tilde{T}^{\mu\nu} + t^{\mu\nu} - \tilde{t}^{\mu\nu}) = 0, \quad (10)$$

where the indices were raised with η . The interpretation could be the following: for any wave radiated on our side which energy carried away by $t^{\mu\nu}$ was lost by $T^{\mu\nu}$ there is of course the accompanying wave on the conjugate side with the same energy $\tilde{t}^{\mu\nu} = t^{\mu\nu}$ carried away implying a back-reaction effect on whatever is the content of $\tilde{T}^{\mu\nu}$: $\partial_\mu T^{\mu\nu} = \partial_\mu \tilde{T}^{\mu\nu}$. It results that the following conservation equations might be separately verified:

$$\partial_\mu (T^{\mu\nu} + t^{\mu\nu}) = 0, \quad (11)$$

$$\partial_\mu (\tilde{T}^{\mu\nu} + \tilde{t}^{\mu\nu}) = 0. \quad (12)$$

In the first equation, we have exactly the same definition of $t_{\mu\nu}$ as in GR while in Eq. (9) the coupling is $G/2$ instead of G in GR. Then for the same strength of gravity (implying a redefinition of G in the equations of the $B = -1/A$ field of Section 3) we expect a radiated power divided by 2 in DG relative to GR.

One could imagine trying to get the correct emission of GW thanks to a separate Einstein–Hilbert action just for our quadrupolar plane waves with a twice larger coupling but this is extremely unnatural Ad-Hoc and most probably nonsensical to separately handle in this way the GW modes and those of the static local field.

A more appealing possibility is if a compact source of mass M on our side generates by its anti-gravitational effect, a matter depleted region, e.g. a “hole” in the conjugate side distribution of matter-energy (resulting in an effective mass $-M$ there in static equilibrium with M on our side) which effect would be equivalent to exactly doubling the source term in Eq. (9) to help us exactly recover the same prediction as in GR without redefining G .

Another idea would maybe help this to work, e.g. get the exact $-M$ effective mass on the conjugate side in any case. The DG theory for the first time allows us to speculate about the vacuum being populated by a network of point fundamental masses with alternating masses plus or minus m_0 , because such picture is then granted to be stable. The masses could be very big provided they are close to each other (small pitch of the network) without having ever been noticed experimentally. Then a given body immersed on our side in such false vacuum would attract the positive plus m_0 on our side and repel the negative minus m_0 of the conjugate side resulting in the actual effective mass that we do measure for this body (we shall investigate in the next section another very different and unrelated kind of vacuum polarisation effect determined by vacuum quantum fluctuations). Because of this vacuum gravitational polarisation effect, any massive body might (further investigation needed) actually be considered as a pair of mass $+M$ on our side and almost exactly effective $-M$ (depleted vacuum region) on conjugate side resulting in the total effective gravific mass $2M$ so we do not need any redefinition of G to recover the same predictions as in GR for both gravitational waves radiation and the local static field! Moreover the mass $+M$ on our side and $-M$ effective mass counterpart on the conjugate side free fall in exactly the same way in any external gravitational field because the behaviour of $-M$ is the same as that of an Archimedian Bubble: it falls in the opposite way, so this extension of the theory appears fully consistent!

Finally, we might consider an unconventional boundary condition for our fields being asymptotically Minkowskian up to a normalisation constant, e.g. $C\eta_{\mu\nu}$ far from sources (this would not matter in GR). Then for $C \gg 1$ we are back to GR for local gravity because all terms depending on the conjugate field become negligible. Moreover $C\eta_{\mu\nu}$ might be conceived as a frozen state of our tensor scalar field. This option is much less appealing because we might lose our beloved exponential static solution at the same time. Eventually, following this last approach, depending on the local C value, a departure from GR predictions could be expected or not both for the gravitational waves radiated power and the local static gravitational field, e.g. depending on the context, we could get either exponential elements or the GR Schwarzschild solution for the static isotropic gravity; and get either no gravitational waves at all or the same radiated power as in General Relativity.

Anyway, stability is granted since those waves and the fields they directly couple to either on our or the conjugate side carry the same sign of the energy.

4.2. Gravity of the vacuum energy

It is well known that the vacuum energy arises as a cosmological constant term which we shall denote Λ . In the absence of gravitational or electromagnetic sources, there is also no reason why such term should differ on our and conjugate side of the Janus field, so the related energy momentum tensors simply are:

$$T_{vac}^{\mu\nu} = \Lambda g^{\mu\nu}, \quad \tilde{T}_{vac}^{\mu\nu} = \Lambda \tilde{g}^{\mu\nu} \quad (13)$$

and the corresponding source term in the DG equation:

$$\sqrt{g}T_{vac}^{\mu\nu} - \sqrt{\tilde{g}}\tilde{T}_{vac}^{\rho\sigma}\eta_{\tau\rho}\eta_{\lambda\sigma}g^{\tau\mu}g^{\lambda\nu} = \sqrt{g}\Lambda g^{\mu\nu} - \sqrt{\tilde{g}}\Lambda \tilde{g}^{\mu\nu} \quad (14)$$

naturally vanishes when $g_{\mu\nu} = \eta_{\mu\nu}$. This is already an impressive result!

However, this might not be the case in general, not only because of the nonvanishing $\sqrt{g} - \sqrt{\tilde{g}} = \sqrt{g} - \frac{1}{\sqrt{g}}$ factor but also because of an expected vacuum “polarisation” induced by any local concentration of mass: then Λ gets replaced by a polarized $\Lambda f_p(g)$ on our side and anti-polarized $\Lambda f_p(\tilde{g}) = \Lambda/f_p(g)$ on the conjugate side. Therefore the source term in the DG equation becomes proportional to $F(g) - 1/F(g)$ where $F(g) = \sqrt{g}f_p(g)$ so that a condition

for a vanishing vacuum contribution to gravity anywhere is $f_p(g) = \frac{\sqrt{\eta}}{\sqrt{g}}$ ($f_p(g)$ needs to be a scalar) which does not seem unreasonable.

So the solution to the worse discrepancy between observation and the General Relativity theory (the vacuum energy contribution to gravity should be huge everywhere which does not appear to be the case) is really now at hand in DG. By the way let us note that a theory without any polarization effect but with an effective action of the kind $\int d^4x \sqrt{\eta} \Lambda \ln(g/\eta)$ on both sides of the Janus field would equally lead to a vanishing vacuum contribution to the gravitational field.

4.3. Acoustic waves

On the very hot conjugate side of our universe (but maybe not so dense if at the beginning of its contraction the conjugate side was almost empty and dominated by photons) not only gravitational but also acoustic waves (as the waves that left their imprint on the CMB) can propagate. The effect of those sound waves can also indirectly be detected from our side as they modify the local density of the fluid and therefore its local gravity felt on our side according the Janus field. Interferometers are also able to detect such longitudinal (acoustic like) waves as these do not expand/contract the two arms in the same way.

5. The Unified DG Theory

5.1. DG actions

Eventually the theory splits up into two parts, one with total action made of a E–H action for our scalar-tensor homogeneous and isotropic Janus field added to SM actions for F and \tilde{F} type fields respectively minimally coupled to $\Phi\eta_{\mu\nu}$ and $\Phi^{-1}\eta_{\mu\nu}$. The other part of the theory has an E–H action for the asymptotically Minkowskian Janus Field $g_{\mu\nu}$ for local gravity (which perturbations $h_{\mu\nu}$ and $\tilde{h}_{\mu\nu}$ can account for the detected gravitational waves) added again to SM actions for F and \tilde{F} type fields respectively minimally coupled to $g_{\mu\nu}$ and $\tilde{g}_{\mu\nu}$.

Our efforts did not allow us to merge the two Janus fields into one, neither in a single E–H action, as we already saw, nor in a single SM source action. This is because when we vary $g_{\mu\nu}$ in its E–H action, this field must also be alone in a SM action and not combined either in an additive or multiplicative way with $\Phi\eta_{\mu\nu}$ because globally there must be an exact cancellation between positive and negative gravific effects from both sides for $g_{\mu\nu}$ to remain asymptotically Minkowskian while introducing $\Phi\eta_{\mu\nu}$ in a SM source action would obviously break the equilibrium.

We thus have two separate theories: one theory that describes the generation of the homogeneous $\Phi\eta_{\mu\nu}$ and also how matter and radiation fields “feel” the effects of this field and one theory that describes the generation of local gravity $g_{\mu\nu}$ and gravitational waves and also how matter and radiation fields react to this gravity. Now the question is: is it possible to merge the theories by merely adding the SM and E–H Actions for $\Phi\eta_{\mu\nu}$ to the SM and E–H Actions for the asymptotically Minkowskian $g_{\mu\nu}$?

Following this way is technically feasible (see Section 9): we need to vary the matter and radiation fields in both SM actions these belong to in order to get their equations of motion. One finds violations of the Weak Equivalence Principle, and also strongly excluded expansion effects of orbital planetary periods relative to atomic periods in the solar system. Trying to cure this by varying the electromagnetic coupling according the scalar $\Phi(t)$ (as in Section 9) is not a solution because it would severely conflict with other strong constraints on the time variation of the fine structure constant. Thus, though we eventually have a good candidate for a unified theory, the latter is not suited to correctly describe all aspects of gravity in the inner part of the solar system at least during the last decades.

In GR because expansion effects and local gravity are described in the same field, it was possible to derive that local gravity in the solar system completely cancels the effect of the background expansion: in other words the solar

system is not expanding which is confirmed by various tests showing for instance that planetary periods are not drifting relative to atomic clock periods.

In DG we have two separate fields which implies that wherever the homogeneous scalar–tensor field applies it will hardly be possible to avoid the related expansion effects: this is for instance what we get in the solar system in our unified theory candidate where we merely add the actions of the two fields.

The only possible solution not to conflict with observational constraints which do not see expanding planet trajectories, is therefore to admit that $\Phi\eta_{\mu\nu}$ was absent at least in the inner part of the solar system during the last decades. But even more it might be that $\Phi\eta_{\mu\nu}$ is always totally absent in the vicinity of mass concentrations and is only discontinuously switched on far away from those gravity sources.

This way DG mimics GR again: no effect of expansion on small scales, but progressively taking place for GR when reaching the largest scales and discretely reappearing in DG at some distance from masses. This implies the existence of genuine field discontinuities at the frontier between zones where the asymptotically Minkowskian $g_{\mu\nu}$ applies alone and zones where $\Phi\eta_{\mu\nu}$ and $g_{\mu\nu}$ are most probably both active and their dynamics could well be described within our unified theory candidate.

To make the argument more simple, let us neglect local gravity and thus approximate our asymptotically Minkowskian $g_{\mu\nu}$ by $\eta_{\mu\nu}$ in the inner part of the solar system. Of course not to lose the cosmological redshift the transition must not be between this $\eta_{\mu\nu}$ and, in the same coordinate system, the outside $\Phi\eta_{\mu\nu}$ where photons spent most of the time during their cosmological trip. On the contrary, understanding that $\eta_{\mu\nu}$ is the metric in standard cosmological time coordinate the transition must be between this $\eta_{\mu\nu}$ and $\Phi\eta_{\mu\nu}$ as well expressed in standard cosmological time coordinate. This means that such new kind of spatial transition discontinuity (between $\eta_{\mu\nu}$ and $\Phi\eta_{\mu\nu}$ expressed in standard time rather than the previously encountered kind of discontinuity between $\Phi\eta_{\mu\nu}$ and $\Phi^{-1}\eta_{\mu\nu}$) now only affects the spatial elements of the metric: small speed matter can freely cross such discontinuity without any noticeable effects while on the contrary light will see a real potential barrier when crossing it.

5.2. Alternating theories

An as well interesting alternative would make appeal to discontinuities in time rather than in space. We are naturally led to consider a possible alternating between the two theories, i.e. that the time is divided in pairs of slots with durations T_g and T_Φ , one for the asymptotically Minkowskian dynamics and one for the homogeneous field dynamics. This kind of time quantization is facilitated by what we have understood about discontinuities in time as having no effect by themselves and allowing now to jump not only between $\Phi\eta_{\mu\nu}$ and $\Phi^{-1}\eta_{\mu\nu}$ but also between $\Phi\eta_{\mu\nu}$ and $g_{\mu\nu}$. So maybe $\Phi\eta_{\mu\nu}$ and the related expansion effects were momentarily absent in the inner part of the solar system, in a recent past including a few decades because it was switched off as it is periodically switched on and off and is therefore able to account on the mean for the redshift on cosmological time scales.

6. Spatial Discontinuities and the Pioneer Effect

6.1. Spatial discontinuities

We have already considered two kinds of discontinuities in time (between $\Phi\eta_{\mu\nu}$ and $\Phi^{-1}\eta_{\mu\nu}$ or between $\Phi\eta_{\mu\nu}$ and $g_{\mu\nu}$) and also spatial discontinuities (between $\Phi\eta_{\mu\nu}$ and $g_{\mu\nu}$). We now shall investigate possible spatial discontinuities of a second kind, e.g. between $\Phi\eta_{\mu\nu}$ and $\Phi^{-1}\eta_{\mu\nu}$. Indeed, one single solution $a(t)$ for the scale factor might not be at work everywhere on a given side of the universe. Some regions might instead be evolving according to the other solution $1/a(t)$ implying that the conjugate background (scalar–tensor) metrics exchange their roles from one to the neighbour region but then also a genuine discontinuity of this background field at their common frontier. The background field is a two valued field that can only jump from one value to the other T-conjugate one: this is another far reaching

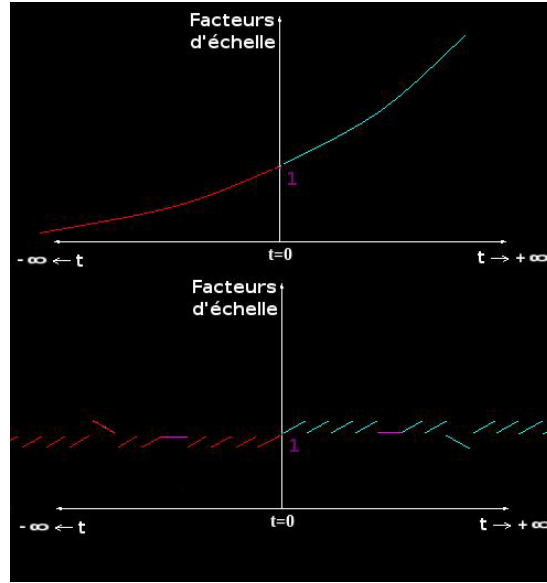


Figure 3. Periodic time resets of the conjugate universes, our side in blue.

consequence of the fact that this scalar-tensor field is “genetically” space independent and cannot smoothly vary in space as would any other usual field because of an inhomogeneous source.^b As we already noticed in our previous article, the discontinuities do not necessarily imply huge potential barriers even though the scale factors have varied by many orders of magnitude between BBN and now. This is because time reversal but also time resets have no effect by themselves as we already explained in a previous section so that the two expansions pictured in top and bottom of Fig. 3 could be actually indistinguishable as for the total cosmological redshifts these imply as long as the evolutions in the continuous phases would be the same (this is not the case in Fig. 3 because in the bottom plot the evolution also had steady and contracting phases, which is also a possibility). On the other hand, the evolution represented at the bottom of Fig. 3 with its periodic resets implies that the conjugate scale factors might remain close to each other so that the implied potential barrier would not necessarily be huge from one region to the neighbour one and the related effects when crossing it might even remain unnoticed in some cases.

6.2. The Pioneer Effect

6.2.1. Introduction

One might wonder why we are still interested in the Pioneer effect after the final verdict by Wikipedia: “The apparent anomaly was a matter of tremendous interest for many years, but has been subsequently explained (in 2012) by an

^bAs we already stressed in previous articles [24], being discontinuous with perhaps global rather than local factors triggering those discontinuities, we have a promising framework to explore the roots of the as well discontinuous and nonlocal rules of quantum mechanics though on the other hand the instantaneous nonpropagated nature of the local gravitational field is now much less obvious than we believed it to be, there being quadrupolar waves to propagate it (maybe!, it is left as an open question whether the quadrupolar propagating modes (pure plane wave hypothesis, no $1/r$ dependency) and isotropic mode (timeless in DG as in GR, according to the Birkhoff theorem) are eventually independent degrees of freedom or not).

anisotropic radiation pressure caused by the spacecraft's heat loss."

The problem is that the spacecraft asymmetric radiation estimated contribution to the anomaly had been shown to be much too small by Anderson [15] taking into account the details of the spacecraft which was specifically designed to keep the radiation as symmetric as possible. On the contrary one finds that all recent "detailed" simulations, in one way or another had to modify the structural properties of the spacecraft just to obtain the desired result: a much larger asymmetry of the radiation. My own detailed analysis is available in [24] (and [25] only in french sorry). Anderson himself is of course not convinced and has again, last summer, published an attempt to explain the Pioneer anomaly and its sudden onset after Saturn encounter by fundamental physics [16], relating it to the cosmological expansion just as we do (but not in the same way). He claims that the "thermal contribution to the anomaly can be approximately modeled to give almost only $\approx 12\%$ ": that's quite an accurate number isn't it? ...and discussed at length in the conclusion of the publication.

6.2.2. Our theoretical explanation

Above formula (16) of Ref [15] there is a CHASMP frequency drift being mentioned which value is half the usually admitted Pioneer effect, followed by the ambiguous comment: half way only. This has even led the author of [14] to interpret that the Pioneer anomaly was actually a H_0 instead of $2H_0$ drift in time rate. The ambiguity for us is the following: did they actually measure a H_0 Pioneer effect on a half way only (implying the Pioneer clock was not locked on the earth clock, contrary to what is asserted several times in the article [15]) from which they deduced the two way $2H_0$ frequency drift assuming it was a Doppler effect or did they really measure the $2H_0$ effect on the complete two way and then deduced from that, again assuming its really an anomalous Doppler effect, the half way value (that would be extremely strange because then there is absolutely no point mentioning this half way value as they do!).

For us, the effect has nothing of a Doppler effect and is actually due to a drift in time of the Pioneer free (unlocked) clock relative to earth clocks so there is an ambiguity because the two above interpretations can be translated into either a H_0 frequency drift in time of Pioneer clock relative to earth clock in the first (one way measurement) case and a $2H_0$ frequency drift in time in the second (two way measurement) case.

In the following we shall explain how we could explain both a $2H_0$ and a H_0 (more straightforward) rate for the drift. We tend to more believe in the H_0 drift because it is more natural in our theoretical framework, but we must still consider the $2H_0$ alternative possibility.

Suppose we can compare ticks of two identical clocks separated by a field discontinuity (with conformal metric assumed on both sides): in one region times accelerates as $a(t)$ and in the other region times decelerates as $1/a(t)$ so from the point of view of one clock the other will be seen to accelerate or decelerate at a rate equal to twice H_0 . This is exactly (quantitatively) equal to the usually admitted $2H_0$ Pioneer frequency drift effect! Now if in one region times accelerates as $a(t)$ and in the other region the cosmological background is stationary, from the point of view of one clock the other will be seen to accelerate or decelerate at a rate equal to H_0 . This second case is more appealing for us because the region where there is no background effect would be the inner part of the solar system (where we find our earth clocks) where indeed various precision tests have shown that expansion or contraction effects on orbital periods are excluded. Obtaining a $2H_0$ Pioneer frequency drift effect without conflicting with such observational constraints is less obvious but we are going to show that it's possible as well. After all we don't know for sure which one of the two above interpretations is correct so we are obliged to consider the two cases. The interpretation of the sudden onset of the Pioneer anomaly after Saturn encounter is also straightforward if this is where the spacecraft crossed the discontinuity of the field at the frontier between the two regions. The discontinuity absolute effect itself would have remained unnoticeable if the two scale factors are close (as we explained earlier) and only the relative drift in time started to be measurable.

We feel sorry for the experts but we prefer to present here a much detailed derivation for the beginners in GR. Hereafter subscript P refers to Pioneer and subscript E to the Earth. In the conformal time t coordinate system we write the metrics:

$$\begin{aligned} d\tau_P^2 &= a^2(t)(dt_P^2 - (dx_P^2 + dy_P^2 + dz_P^2)) \Rightarrow dt_P = \frac{1}{a(t)} d\tau_P, \\ d\tau_E^2 &= a^{-2}(t)(dt_E^2 - (dx_E^2 + dy_E^2 + dz_E^2)) \Rightarrow dt_E = a(t) d\tau_E \end{aligned} \quad (15)$$

for rest clocks ($dx = dy = dz = 0$), from which follows considering two successive ticks of identical clocks ($d\tau_P = d\tau_E$):

$$\frac{dt_E}{dt_P} = a^2(t) = \frac{f_P}{f_E} \Rightarrow \frac{\dot{f}_{P/E}}{f_{P/E}} = 2 \frac{a\dot{a}}{a^2} = 2 \frac{\dot{a}}{a}, \quad (16)$$

where $f_{P/E}$ and $\dot{f}_{P/E}$ are the frequency and frequency derivative of the Pioneer clock as measured from Earth, i.e. taking as reference an Earth clock. Of course this expression is valid in conformal time coordinate t .

We want the expressions in standard time coordinate t' because this is the one we use to get the Hubble cosmological parameter. On earth we have

$$\begin{aligned} d\tau^2 &= dt'^2 - a'^{-2}(t')(dx^2 + dy^2 + dz^2) \\ &= g'_{\mu\nu} dx'^\mu dx'^\nu \\ &= g_{\mu\nu} dx^\mu dx^\nu \\ &= a^{-2}(t)(dt^2 - (dx^2 + dy^2 + dz^2)); \end{aligned} \quad (17)$$

however, using this same t' that puts the earth metric in standard form, the Pioneer metric would have a quite different form, neither standard nor conformal. Anyway we now just need

$$\frac{f'_P}{f'_E} = \frac{dt'_E}{dt'_P} = \sqrt{\frac{g'_{00P}}{g'_{00E}}} = \sqrt{\frac{\left(\frac{\partial t}{\partial t'}\right)^2 g_{00P}}{\left(\frac{\partial t}{\partial t'}\right)^2 g_{00E}}} = \sqrt{\frac{g_{00P}}{g_{00E}}} = \frac{dt_E}{dt_P}. \quad (18)$$

This transformation of coordinate is very well known and very simplified because only the time is transformed. So the frequency ratio is still the same as it was in conformal coordinate ...

$$\frac{f'_P}{f'_E} = a^2(t) \quad (19)$$

but now we just would like to express it in the new t' coordinate. This is an easy task because the space–space metric elements are invariant under such time transformation, for instance:

$$a^2(t) = -\frac{1}{g_{11}} = -\frac{1}{g'_{11}} = a'^2(t'). \quad (20)$$

Eventually

$$\frac{f'_P}{f'_E} = a'^2(t') \Rightarrow \frac{\dot{f}'_{P/E}}{f'_{P/E}} = 2 \frac{a'\dot{a}'}{a'^2} = 2 \frac{\dot{a}'}{a'}, \quad (21)$$

where of course all derivatives now are relative to the standard time t' .

Now beware that our scale factor is not $a'(t')$ but $1/a'(t')$ in Eq. (17) so an increasing $a'(t')$, needed to obtain the Pioneer blue shift, a positive $2(\dot{a}'/a')$, describes a contracting universe with respect to earth reference clocks. This is

even better understood coming back to the conformal coordinate system where Eq. (15) makes it clear that earth clocks time intervals are increasing while Pioneer clocks time intervals are decreasing relative to constant photon periods in this coordinate system. In other words, as seen from Pioneer the universe is expanding (cosmological photons are red shifted) whereas as seen from earth the universe is instead contracting (cosmological photons are blue shifted). Yet we know that from earth we see that the universe has been expanding for billion years. What the Pioneer effect tells us is that this has not always been the case, because at least at the time the Pioneer effect was registered the universe is contracting relative to earth clocks rather than expanding. Only the Dark Gravity theory and its discrete symmetries allow that, because discrete jump from an expanding to a contracting solution are naturally expected to occur either globally or locally, when the conjugate metric exchange their roles. Eventually

$$\frac{\dot{f}'_P}{\dot{f}'_E} = 2 \frac{\dot{a}'}{a'} = -2H'_{00} = 2H'_0, \quad (22)$$

where H'_{00} refers to the instantaneous recent Hubble factor at least valid during the last decades while H'_0 is the cosmological Hubble parameter as we get it from an SNs magnitude-redshift fit for instance. They are opposite as the result of a transition $a'(t') \rightarrow 1/a'(t')$.

However, one concern remains. We already noticed that no expansion/contraction effect has been active in the inner part of the solar system during the past decades. So neither of the two metrics in Eq. (15) are actually acceptable in the inner part of the solar system.

This problem is easily solved and to simplify the argument we neglect, hereafter, the nonrelevant local gravitational fields. The problem is solved because the metric in the inner part of the solar system is actually $g_{\mu\nu} \approx \eta_{\mu\nu}$ alone as we explained earlier (which trivially avoids expanding orbits) and the cosmological effects are only switched on outside of this zone with a discrete transition from $\eta_{\mu\nu}$ to the metric of $d\tau^2 = dt'^2 - a(t')^2 d\sigma^2$. The important point here is that this $\eta_{\mu\nu}$ is already expressed in standard time coordinate so rest clocks from both sides of such new kind of discontinuity are obviously not drifting with respect to each other since no scale factor applies to temporal elements of both metrics. The only possible effects, Shapiro delay and deflection for photons crossing such discontinuity, are irrelevant here (these are more interesting in case of a huge discontinuity surrounding a black hole candidate because most of its radiation might be reflected, allowing the hole to remain as black as in GR but without any event horizon).

Let us emphasize that this $\eta_{\mu\nu}$ has nothing to do with the stationary solution of our scalar-tensor field which is $\eta_{\mu\nu}$ in conformal rather than standard time! Again, this $\eta_{\mu\nu}$ is an approximated expression of our asymptotically Minkowskian field $g_{\mu\nu}$. Now, after the discontinuity between asymptotically Minkowskian and scalar-tensor field, as a second step we can switch the very different kind of discontinuity between the expanding and contracting solutions of the scalar-tensor field: this is just what we did above to get the Pioneer effect.

This reasoning in two steps and with two successive discontinuities allows us to understand more easily how we can get the $2H_0$ acceleration flipping directly between $\eta_{\mu\nu}$ (earth side) and $a^2(t)\eta_{\mu\nu}$ of Eq. (15) (Pioneer side) expressed in the same time t' (see Eq. (17)), that puts the $a^{-2}(t)\eta_{\mu\nu}$ metric (rather than the $a^2(t)\eta_{\mu\nu}$ metric) in a standard form.

This means that we are able to both account for the acceleration of Pioneer clock at a rate $2H_0$ relative to earth clocks even though the latter clocks and actually all the inner part of the solar system encompassed by the discontinuity are not submitted to any scale factor effect as required by observational constraints!

Now if the pioneer anomaly was actually $\dot{f}'_P/\dot{f}'_E = H_0$ instead of $2H_0$ everything is more simple because this rather means that we have a direct transition from $\eta_{\mu\nu}$ (earth side) to $a^2(t)\eta_{\mu\nu}$ of Eq. (15) (Pioneer side) now both already in conformal time t , rather than a transition from $\eta_{\mu\nu}$ in standard time t' and $a^2(t)\eta_{\mu\nu}$ transformed to the t' time coordinate as we just explained above to get the $2H_0$ effect. Moreover, $\eta_{\mu\nu}$ in this case (H_0 effect), and still neglecting local gravitational fields, could as well be interpreted as a stationary solution of our scalar-tensor (background) field.

6.2.3. PLL issues

A last but not least issue is that in principle a Pioneer spacecraft should behave as a mere mirror for radio waves even though it includes a frequency multiplier. This is because its re-emitted radio wave is phase locked to the received wave so one should not be sensitive to the own free speed of the Pioneer clock.

Our interpretation of the Pioneer effect is thus that either all data were actually collected in open loop mode (kind of conspiracy theory since, to obtain correct Doppler data, this anyhow implies manipulations at the level of raw data that was not documented, which then prevented any theoretical convincing explanation of the Pioneer effect. Notice that the open loop mode is anyway mandatory to get the H_0 Pioneer effect rather $2H_0$) or there was a failure of on board PLLs to specifically “follow” a Pioneer like drift in time.

The latter interpretation makes sense since we never studied before how the scale factor varies on short time scales: it might be that it only varies on very rare and short time slots but much more rapidly (with much bigger Hubble factor) so that integrated on longer durations we recover the mean known H_0 . This behaviour would produce high frequency components in the spectrum which might have not passed a low pass filter in the PLL, resulting in the on board clocks not being able to follow those sudden drifts and keep locked. Only when the integrated total drift of the phase would reach a threshold level, this system would “notice” that something went wrong, perhaps resulting in those instabilities and loss of lock (?) that one can notice in the Doppler fit residues (Fig. 9 of Ref. [15]). Indeed (from now on we give up the primes in our notations) for a $f = 2.29$ GHz clock, $\dot{f} = f \cdot 2a_{p/c} = 1.2 \times 10^{-8}$ Hz/s where a_p is the anomalous acceleration in the most usual (not our) interpretation of the Pioneer effect, and we used formula (15) of Ref. [15]. A loss of lock seems to be happening at least twice a year as we can see in Fig. 9 of Ref. [15]. On half a year the Pioneer effect reaches a 0.15 Hz total drift ($a \approx 13$ degrees phase shift) which might be close to or greater than the suspected threshold. The inability to keep lock also makes sense if the PLL system was actually designed specifically not to keep lock on a Pioneer type drift in time which were not so difficult to theoretically anticipate: any local effect of the cosmological expansion could only possibly arise if one could compare free clock speeds as we have explained in details above ... so it's hard to believe that no solar system mission attempted to do this given the major theoretical issues, and given that the deep space environment is very helpful for the necessary on-board clock stability to be granted.

7. From Field Discontinuities to LENR

7.1. Reminder

We have so far encountered discontinuities in time and discontinuities in space. The latter type can also further be divided into two kinds: the first kind is a discontinuity between a zone where the local tensor field applies alone and another zone where the scalar-tensor homogeneous field is also switched on. We are going here to focus on the second kind of spatial discontinuities, those between the different possible solutions of our homogeneous scalar–tensor field which of course imply potential barriers able to accelerate massive particles crossing them (the energy gained or lost is proportional to their mass) so these could be new sources of energy for LENR phenomena. However these are totally transparent to light or other massless particles. We have already paved the way to LENR in details in a previous article. We refer the reader to this article [18] (see also [9,10,12,13] and references therein for experimental evidences related to “strange objects” produced in association with LENR) and will now focus on what is new in our understanding of the mechanism that is responsible for the apparition of a micro-ball lightning (mbl).

What remains true here is that the source term in Eq. (3) determines whether the background (scalar–tensor field) chooses the $a(t)$ evolution or the $1/a(t)$ evolution. It just depends on which contribution is the greater, our side or the conjugate side one. If we are in a vast region dominated by the conjugate side source term then a local concentration of energy on our side, as soon as it locally exceeds the conjugate side one, triggers the background flip in this region to the

other regime, producing a discontinuity at the surface frontier between the external area where the conjugate side still dominates and the internal one which is enclosed by the discontinuity. Notice also that it is only the nonkinetic sources of energies that contribute to our source terms which tend to vanish in the ultra-relativistic limit. We then proposed that the universal trigger be a concentration of charges implying a local increase of the electrostatic energy because such form of static energy could better fill the available space than rest mass energy of nucleons confined inside a very small volume at the center of atoms.

7.2. Electronic density is the trigger

However, because the nucleons rest mass is by far the dominant form of energy it certainly implies discontinuities near the surface of these nucleons or nuclei. There however, the discontinuous low potentials (less than 10 eVs) are completely insignificant relative to the energies at work involving the strong interactions. The question is therefore: what could increase the density of static energy outside of the nuclei to pull the discontinuities out of these, and hopefully enough far away to allow them to encompass not even a single atom but many atoms? The electrostatic energy was indeed a candidate for that but the electronic density of energy as implied by the electrons rest masses is much greater and is also able to fill the volume of an atom or several atoms: this is what an electron wave function does if it truly represents the electron rest mass spread over a volume. Moreover, this form of energy can really become dominant over the conjugate side one thanks to a local concentration of electrons, because most of the conjugate side content is ultra-relativistic and has a very reduced contribution as we already noticed. However conjugate side fluctuations may play an important role by indirectly favouring more or less LENR. Those fluctuations could also be related to the local conjugate side production of a large number of matter-anti-matter pairs near their production threshold where these are nonrelativistic and can contribute to the source. This is an argument for understanding the sometimes very unpredictable and capricious character of LENR if, as we believe, LENR is made possible by the production of mbls.

7.3. Best experimental methods

So now the game for LENR hunters would be to find the best way to increase or make fluctuate the local density of electrons, not inside the atoms where it is imposed by the individual potential well of each nucleus, but rather at their periphery to pull out the discontinuities out of the atoms and let them encompass many atoms.

We believe that all methods allowing the system to reach the highest local pressures, the better in an impulsive way, should be helpful to achieve this. Electrical discharges are also another way to bring for a short time a large number of electrons in a small volume before these escape because of their mutual repulsion. Another way is to throw a beam packet with a very large number of electrons (impulse) onto a target: the results obtained already 10 years ago by this method was very impressive and have supported almost all features of our mbl theory [19], including the production of extremely exotic nuclei with thousands of nucleons! Plasma discharges have also given impressive results showing transmutations, unexplained energy release and big lightning balls with a substructure appearing to involve many much smaller lightning balls [22,23]. The needed super-compression might also be obtained in Z-pinch and other discharge experiments where anomalies have indeed been reported [20].

7.4. The stability issue

The next question is: is the mbl produced by such a local increased density of electrons, stable? As we explained in our previous article [18], the discontinuous potential barrier is completely negligible for electrons so it does not ensure the stability of an mbl which origin is a concentration of electrons. It depends however on how electrons escape the mbl

then: is the electron density going to drop uniformly or much faster near the surface of the mbl? In the first case many discontinuities will eventually appear, each to encompass each individual atom (just as many islands may remain when sea level rises at the place there was a single larger island) and the mbl will soon disappear in this way. In the second case the discontinuity will start to push the nuclei against each other up to the point where the electrons cannot escape because they must compensate the nuclei positive charge concentration by their own negative charges: at this point the mbl is auto-stabilized because the concentration of electrons that gave birth to it is maintained by the concentration of nuclei.

7.5. The mbl collapse

Also notice that such mbls where positive and negative charges densities are increased together are not necessarily very charged (net charge) on the contrary to mbls produced by electrical discharges where there is a dominant concentration of one type of charge. Anyway our slow and fast collapse scenarios for mbls [18] must be revised since there is now nothing such as a slow or fast neutralization of an mbl to make it collapse. A collapse would now most probably be driven by the conditions prevailing on the conjugate side if they modify the balance between the two source terms in Eq. (3). The rapidity of such collapse remains crucial to predict which transmutations and nuclear reactions will be allowed. A too fast collapse will heat the content of the mbl too fast and it will lose its nuclei before these can fuse or participate to any nuclear reactions. To be more quantitative we can consider as an exercise a mbl which radius is initially one micrometer and which content is hydrogen at 2000 K and density nearly stp (we cannot exclude such low density mbls for instance in case a fluctuation in the distribution of matter energy on the conjugate side, or a local increase of electrostatic energy density on our side was the trigger). During a first phase of the collapse dividing the radius by 10 (volume by 1000), the density remains lower than the condensed Hydrogen density. Because the initial thermal energy of the mbl is 10^{-11} J and its radiative power according the Stefan–Boltzman law starts from 10^{-5} W and will decrease by a factor 100 as the mbl size gets reduced by 10, the mbl could dissipate its energy in 1 μ s unless its collapse is much faster than this time. In this fast collapse case, instead the temperature might rise adiabatically as $T \propto 1/R^{3(\gamma-1)} = 1/R^{1.2}$ and the mbl would see its temperature increased by a factor 16, and the mean kinetic energy per nucleus allows the Hydrogen to escape the mbl that soon disappears in this way.

As a second exercise, we can consider a mbl with initially already the density of condensed matter, for instance Ni at again 2000 K and 1 μ m radius. Now the initial thermal energy of the mbl is $\approx 3 \times 10^{-8}$ J which could be dissipated in 3 ms. But now the compression of the condensed matter is expected to be converted in elastic energy (a form of electrostatic internal energy) rather than thermal energy so the temperature might not increase as in the gas case for a fast adiabatic compression. This is fortunate for the stability of the mbl but it remains true that a collapse much shorter than a millisecond would not allow the mbl to dissipate its initial thermal energy radiatively: moreover, after suddenly collapsing by a factor 10, the mbl now needs as much as 0.3 s to radiatively dissipate this energy.

The lesson from the two previous exercises is that the initial content and density of the mbl does matter.

Now beyond a factor 10 compression level if the mbl is still alive, we are now crushing densities beyond those of condensed matter and the temperature can more easily remain stable so that the mbl itself has good chance to remain stable up to much higher densities needed both to help trigger nuclear reactions and thermalize their radiation products.

In a slow collapse of an mbl with a large number of nuclei, the nuclei remain cold and at some point their wave functions will overlap, and a collective, new many body kind of nuclear process is expected to be triggered. Because this is a reaction involving a large number of degrees of freedom, it is not unnatural, as in any system with many degrees of freedom, to see a continuously evolving nuclear process with very progressive energy exchanges taking place as there is a collective re-arrangement of the nucleons between nuclei (According L. Urutskoev [11] this might explain the difference between short duration experiments giving a small energy release per nuclei involved in transmutations as in his own discharge experiments, while longer experiments, à la Rossi, would produce much larger time integrated

energy releases.) Continuous here means that each step of the process would involve a small energy release, which is possible as the mass difference between a many body input and many body output to a reaction can almost be made as small as we like. Thus what is crucial for such process to proceed in this way is both the extreme density AND extreme coldness of the state of matter reached at the end of the mbl collapse and actually only mbls can reach such state: stars and the primordial universe are both extremely dense but also extremely hot and for instance it will take many billions of years for white dwarf to cool down to such room temperatures while a micrometer object can radiate away its heat much more effectively. The cold temperature is presumably very important because it is the parameter that ensures that two body collisions and their huge nuclear energy releases will not be triggered before reaching the state where the nuclei wave functions all largely overlap (large Heisenberg extension is related to the small mean kinetic energy) each other and presumably begin to behave as a whole intricate entity! Of course this is still a very qualitative picture at this stage, and should be hopefully confirmed by detailed analysis and computations by nuclear physics experts: hopefully because the experimental evidence is already there and overwhelming (Ref. [19] for instance)!

7.6. Remarks concerning lowest energy experiments trying to generate heat

Eventually in an experiment which impulse energies are too small so that mbls are hardly produced and a too small number of them is able to reach the density conditions for nuclear fusion, it is better to increase as much as possible the number of sites where high pressures are reached in condensed matter or where micro electrical discharges could take place. For example huge local pressures (GPa) can be reached locally in silicium platelets and cracks [21] after the Silicium was submitted to a 32 keV Hydrogen ions beam so a beam is an effective method to create high pressure spots to favour the generation of mbls in materials. This most probably contributes effectively to the impressive LENR anomalies obtained in various low energy beam (in Japan for instance) or discharge experiments.

For low energy experiments it also makes sense to feed the mbls with the lightest fuels such as hydrogen isotopes which according the usual laws of nuclear physics have an enhanced probability to fuse, well before the conditions could be reached to obtain other less favored reactions. It remains an open question whether, in order to produce heat, it's more interesting to trigger two body reactions which high energy radiation products are efficiently thermalized in the ultra-dense mbl or many body reactions with a much lower and more progressive energy release. But let us keep in mind that the first nuclear reactions taking place can lead to premature disintegration of the mbl and prevent it to reach the conditions for other kind of reactions.

7.7. Tritium and Helium 3

One more feature difficult to explain in LENR experiments able to trigger hydrogen fusion into He4 is the observation of tritium while He3 is absent. The ultra-dense medium inside an mbl as we understand it might be the key to the enigma because it leads to a medium populated with high Heisenberg energy electrons. Those are able to transform protons belonging to various nuclei into neutrons through the weak interaction. We believe that for instance most He3 nuclei could be effectively transformed into tritium when the 19 keV needed energy can be provided by the electrons. The same kind of process starting from a heavier nuclei (nickel for instance) involving a chain of fusions with protons, each followed by weak transformation of those protons into neutrons would also allow to explain the chain of nickel transmutations leading to heavier Ni isotopes observed in the Rossi reactor according to the Lugano report.

8. Conclusion

We have reviewed the genesis of the DG theory along with some of its most important results in cosmology, but also described how the gravitational waves and the Pioneer effect can be understood within this new framework. Let us

stress that the Pioneer effect remains ambiguous and has been interpreted by some as a clock acceleration with rate H_0 rather than $2H_0$. DG can explain both quite simply and naturally but a rate H_0 is even more straightforwardly obtained. A last part was devoted to an important revision of the mechanism that we believe is responsible for the apparition of micro lightning balls appearing to be strongly correlated with LENR effects in many kind of experiments.

9. Annex: Matter and radiation field equations: the two metric case

In the following, we want to see what kind of equations we could get assuming our radiation and matter fields at the same time minimally couple to both our homogeneous cosmological field and asymptotically Minkowskian field in their respective separate actions. We by the way applied a “somewhat questionable trick” to get the same expansion effect on gravitationally and electromagnetically bound system, otherwise this would not be natural. We remain in the conformal time coordinate system and adopt the conventions of [6].

As in [6], p. 358, formula (12.1.6), we take the matter (particle with mass m and charge e) and radiation (EM vector potential A_μ) action as:

$$I_M = -m \int dp \frac{d\tau(p)}{dp} - \frac{1}{4} \int d^4x \sqrt{g} F_{\mu\nu}(x) F^{\mu\nu}(x) + e \int dp \frac{dx^\mu(p)}{dp} A_\mu(x(p)) \quad (23)$$

and vary the dynamical variable $x(p)$ and A_μ following the same steps as in [6], p. 359, but keeping p as the integration variable. First varying $x(p)$ we eventually get the action variation

$$\begin{aligned} \delta I_M = \int dp g_{\mu\lambda}(x(p)) & \left(-m \frac{dp}{d\tau(p)} \left[\frac{d^2 x^\mu(p)}{dp^2} + \Gamma_{\rho\sigma}^\mu(x(p)) \frac{dx^\rho(p)}{dp} \frac{dx^\sigma(p)}{dp} \right] \right) \delta x^\lambda(p) \\ & + e \int dp g_{\mu\lambda}(x(p)) \frac{dx^\rho(p)}{dp} F_\rho^\mu(x(p)) \delta x^\lambda(p). \end{aligned} \quad (24)$$

But now suppose the same matter and radiation fields are also minimally coupled to another $\bar{g}_{\mu\nu}$ in \bar{I}_M which variation $\delta \bar{I}_M$ we need to add to the previous δI_M . With the same integration variable:

$$\begin{aligned} \delta \bar{I}_M = \int dp \bar{g}_{\mu\lambda}(x(p)) & \left(-m \frac{dp}{d\bar{\tau}(p)} \left[\frac{d^2 x^\mu(p)}{dp^2} + \bar{\Gamma}_{\rho\sigma}^\mu(x(p)) \frac{dx^\rho(p)}{dp} \frac{dx^\sigma(p)}{dp} \right] \right) \delta x^\lambda(p) \\ & + e \int dp \bar{g}_{\mu\lambda}(x(p)) \frac{dx^\rho(p)}{dp} \bar{F}_\rho^\mu(x(p)) \delta x^\lambda(p). \end{aligned} \quad (25)$$

Now $\bar{g}_{\mu\nu}$ is nothing but our scalar tensor $a^2(t)\eta_{\mu\nu}$ and $g_{\mu\nu}$ our local field. If we want to study the first order effects of the scale factor $a(t)$ we can certainly approximate $\bar{g}_{\mu\lambda}$ by $a^2 g_{\mu\lambda}$ and $d\bar{\tau}(p)$ by $a d\tau(p)$. Eventually changing the integration variable from p to τ , requiring a vanishing total action variation gives us the equation of motion for our particle:

$$(1 + a) \frac{d^2 x^\mu(p)}{dp^2} + (\Gamma_{\rho\sigma}^\mu(x(p)) + a \bar{\Gamma}_{\rho\sigma}^\mu(x(p))) \frac{dx^\rho(p)}{dp} \frac{dx^\sigma(p)}{dp} = \frac{e}{m} \frac{dx^\rho(p)}{dp} (F_\rho^\mu(x(p)) + a^2 \bar{F}_\rho^\mu(x(p))), \quad (26)$$

where we eventually renamed τ into p again. Did you see the “trick”? Anyway there is no doubt that such equations could more rigorously be obtained by introducing extra scalar coefficients $\Phi = a^2(t)$ where we need them in the actions ... however there is also no doubt this would be at the price of violating constraints on the secular variation of the fine structure constant.

Now varying $A_\mu(x)$ we eventually get the total action variation

$$\begin{aligned} & \int d^4x \left(\frac{\partial}{\partial x^\mu} [\sqrt{g} F^{\mu\nu}(x)] + e \int dp \delta^4(x - x(p)) \frac{dx^\nu(p)}{dp} \right) \delta A_\nu(x) \\ & + \int d^4x \left(\frac{\partial}{\partial x^\mu} [\sqrt{\bar{g}} \bar{F}^{\mu\nu}(x)] + e \int dp \delta^4(x - x(p)) \frac{dx^\nu(p)}{dp} \right) \delta A_\nu(x) \end{aligned} \quad (27)$$

and with $\bar{g}_{\mu\nu} = a^2(t)\eta_{\mu\nu}$, $\sqrt{\bar{g}}\bar{F}^{\mu\nu}(x) = F_{\mu\nu}(x)$ we see that the derived Maxwell equations will not be sensitive to the scale factor as expected in conformal time coordinate. We again require the action variation to vanish to get:

$$\frac{\partial}{\partial x^\mu} [\sqrt{g} g^{\mu\rho} g^{\nu\sigma} F_{\rho\sigma}(x) + \eta^{\mu\rho} \eta^{\nu\sigma} F_{\rho\sigma}(x)] = -2e \int dp \delta^4(x - x(p)) \frac{dx^\nu(p)}{dp}. \quad (28)$$

However, this equation violates the Weak Equivalence Principle in gravitational redshift experiments so this is already a dead end.

Now our purpose is to only investigate the effect of the scale factor in Eq. (26) for the case $a(t) \gg 1$ to see if at least something interesting could happen in this sector. Then:

$$\frac{d^2 x^\mu(p)}{dp^2} + \left(\frac{1}{a} \Gamma_{\rho\sigma}^\mu(x(p)) + \bar{\Gamma}_{\rho\sigma}^\mu(x(p)) \right) \frac{dx^\rho(p)}{dp} \frac{dx^\sigma(p)}{dp} = \frac{e}{m} \frac{dx^\rho(p)}{dp} \left(\frac{1}{a} F_\rho^\mu(x(p)) + a \bar{F}_\rho^\mu(x(p)) \right) \quad (29)$$

with $F_{\rho\nu} = (\partial_\rho A_\nu - \partial_\nu A_\rho)$ where $A_\mu = (V(r), 0, 0, 0)$. The free fall equations of motion in the plane $\theta = \pi/2$ and in the slow velocity approximation read:

$$\frac{d^2 r}{dp^2} + \frac{1}{2a} \frac{B'}{A} \left(\frac{dt}{dp} \right)^2 + 2 \frac{\dot{a}}{a} \frac{dr}{dp} \frac{dt}{dp} = \frac{q}{m} \frac{V(r)'}{a(t)} \left(\frac{1}{A} + 1 \right) \frac{dt}{dp},$$

$$\frac{d^2 \phi}{dp^2} + 2 \frac{\dot{a}}{a} \frac{d\phi}{dp} \frac{dt}{dp} + \left(\frac{A'}{aA} + \frac{2}{r} \right) \frac{dr}{dp} \frac{d\phi}{dp} = 0,$$

$$\frac{d^2 t}{dp^2} + \frac{B'}{aB} \left(\frac{dr}{dp} \right) \left(\frac{dt}{dp} \right) + \frac{\dot{a}}{a} \left(\frac{dt}{dp} \right)^2 = \frac{q}{m} \frac{V(r)'}{a(t)} \left(\frac{1}{B} + 1 \right) \frac{dr}{dp}.$$

We integrate the second equation after dividing it by $d\phi/dp$

$$\frac{d}{dp} \left[\ln \left(\frac{d\phi}{dp} \right) + \ln A^{1/a} + \ln a^2 + 2 \ln r \right] = 0 \Rightarrow \frac{d\phi}{dp} \propto \frac{1}{a^2 r^2}$$

keeping only the leading $a(t)$ term (we could as well have switched off the local gravity).

We then perform the integration of the third equation:

$$\frac{dt}{dp} \frac{d}{dp} \left(\ln \frac{dt}{dp} + \ln B + \ln a \right) = \frac{q}{m} \frac{dV}{a(t) dp} \left(\frac{1}{B} + 1 \right) \quad (30)$$

or defining $u = a(t)(dt/dp)$ and keeping only leading term in $a(t)$:

$$u \frac{d}{dp} (\ln u) \approx \frac{2q}{m} \frac{dV}{dp} \quad (31)$$

hence now

$$\frac{dt}{dp} = \frac{2}{a(t)} \left(\frac{q}{m} V(r) + 1 \right) \propto \frac{1}{a(t)},$$

which allows us to get

$$\dot{\phi} \approx \frac{1}{ar^2}$$

We could again have switched off local gravity and electromagnetism to get this result. The first equation in the small speed limit and using

$$\frac{d}{dt} \left(\frac{dt}{dp} \right) = -\frac{\dot{a}}{a} \frac{dt}{dp}$$

gives

$$\begin{aligned} \frac{d}{dt} \left[\frac{dt}{dp} \frac{dr}{dt} \right] \frac{dt}{dp} + \frac{1}{2} \frac{B'}{aA} \left(\frac{dt}{dp} \right)^2 + 2 \frac{\dot{a}}{a} \dot{r} \left(\frac{dt}{dp} \right)^2 &= \frac{q}{m} \frac{V(r)'}{a(t)} \left(\frac{1}{A} + 1 \right) \frac{dt}{dp} \\ \Rightarrow \left[\ddot{r} - \frac{\dot{a}}{a} \dot{r} \right] + \frac{1}{2} \frac{B'}{aA} + 2 \frac{\dot{a}}{a} \dot{r} &\approx \frac{q}{m} V(r)'. \end{aligned}$$

Eventually,

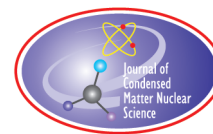
$$\ddot{r} \approx \frac{q}{m} V'(r) - \frac{1}{2} \frac{B'}{A} - \frac{\dot{a}}{a} \dot{r}.$$

Thanks to our “trick” (for which again we surely could elaborate a rigorous version thanks to our “always available when needed” scalar field), the effects of expansion are the same on electromagnetic or gravitationally bound systems and, for circular orbits, produce a drift of their periods relative to periods of free electromagnetic waves which are constant in our conformal coordinate system: therefore the universe is correctly expanding. In standard cosmological time, on the contrary, light periods would of course expand as usual relative to constant gravitational and electromagnetic periods. However we again emphasize that in this case we most probably cannot avoid WEP violations and also large, already ruled out, evolution of the fine structure constant. Eventually the lesson is that at least in the inner part of the solar system during the last decades, our homogeneous field was not active in any way. On the other hand, wherever our homogeneous field is switched on gravitationally bound system will expand (relative to atoms) in the same way whatever the scale (stellar systems, galaxies, and of course larger scale structures). Trying to avoid this would produce variations of the fine structure constant.

References

- [1] F. Henry-Couannier, *Int. J. Mod. Phys. A* **20**(NN) (2004) 2341–2346.
- [2] F. Henry-Couannier, *Global J. Sci. Frontier Res. A* **13**(3) (2013) 1–53.
- [3] J.P. Petit, *Astrophys. Space Sci.* **226** (1995) 273.
- [4] S. Hossenfelder, *Phys. Rev. D* **78** (2008) 044015.
- [5] F. Henry-Couannier, Dark Gravity, *Global J. Sci. Frontier Res. F* **12**(13) (2012) 39–58.
- [6] S. Weinberg, *Quantum Field Theory*, Vol. 1, Cambridge University Press, Cambridge, 1972.
- [7] J.P. Petit, *C. Roy. Acad. Sci. Paris.* **285** (1977) 1217–1221.
- [8] J.P. Petit, and G. D’ Agostini, *Astrophys. Space Sci.* **354** (2014) 611–615.
- [9] E. Lewis, *J. Condensed Matter Nucl. Sci.* **2** (2009) 13.
- [10] L.I. Urutskoev and V.I. Liksonov, *Ann. Fond. Louis de Broglie* **27**(4) (2002) 701.
- [11] L.I. Urutskoev, Private communication.
- [12] K. Shoulders and S. Shoulders, Charge Clusters In Action, manuscript article, 1999.

- [13] M. Rambaut, *Proc. 11th Int. Conf. on Cold Fusion, Marseille*, 2004, pp. 798–805.
- [14] L.M. Tomilchik, arXiv:0710.3994, 2007.
- [15] J.D. Anderson, P.A. Laing, E.L. Lau, A.S. Liu, M.M. Nieto and S.G. Turyshev, *Phys. Rev. D* **65** (2002) 082004.
- [16] J.D. Anderson and M.R. Feldman, *Int. J. Mod. Phys. D* **24** (2015) 1550066.
- [17] M. Vargas dos Santos, R.R.R. Reis and I. Waga, *J. Cosmol. Astropart. Phys.* **02** (2016) 066.
- [18] F. Henry-couannier, *J. Condensed Matter Nucl. Sci.* **18** (2016) 1–23.
- [19] S.V. Adamenko and V.I. Vysotskii, *Proc. 10th Int. Conf. on Cold Fusion, Cambridge*, 2003, pp. 493–508.
- [20] A.V. Agafonov, V.A. Bogachenkov, A.P. Chubenko, A.V. Oginov, A.A. Rodionov, A.S. Rusetskiy, V.A. Ryabov, A.L. Shepetov and K.V. Shpakov, Observation of hard radiations in a laboratory atmospheric high-voltage discharge, arXiv:1604.07784, to be published.
- [21] F.-X. Darras, *Precipitation et contrainte dans le silicium implante par hydrogene*, These, Universite Paul Sabatier, 2015.
- [22] A. Klimov, *J. Condensed Matter Nucl. Sci.* **19** (2016) 145–154.
- [23] A. Klimov, *J. Condensed Matter Nucl. Sci.* **19** (2016) 155–163.
- [24] <http://www.darksideofgravity.com/pioneeradiation.html>
- [25] http://www.darksideofgravity.com/GPB_underscore_news.html
- [26] H. Yilmaz, New approach to general relativity, *Phys. Rev.* **111** (1958) 1417–1426.



Research Article

Investigations of the Lugano HotCat Reactor

Mathieu Valat*, Alan Goldwater, Robert Greenyer, Robert Higgins and Ryan Hunt

Martin Fleischmann Memorial Project

Abstract

Since its release, the “Lugano Report” has attracted a lot of attention from many scientific groups as well as individuals. Following attempts to reproduce the claimed results, the Martin Fleischmann Memorial Project[†](MFMP) is adding significant insights to the replication community across the Internet. The first part of the paper describes the replication of the Lugano Report’s thermal measurements. It presents the experimental setup, instrumentations as well as the results produced by the MFMP team. The second part describes attempts to reproduce the excess energy claimed in the Report. After ten experiments and five incremental revisions of the apparatus, MFMP published results on the Internet showing apparent correlation between anomalous heat production and broadband low energy gamma radiation. This paper offers a review of these two significant experiments, done in March 2015 and January 2016.

© 2016 ISCMNS. All rights reserved. ISSN 2227-3123

Keywords: Andrea Rossi, e-cat, Lithium aluminum hydride, Lugano report, Nickel, Replication

1. Replication of the Thermal Heat Measurement from the Lugano Report

Following the release of the Lugano Report [1], the Martin Fleischmann Memorial Project (MFMP) decided to allocate part of its efforts toward replication/validation of the report’s thermal measurements. Numerous shortfalls were found in the measurements and analyses within this report. One critical error was determination of the temperature based upon an emissivity function for alumina that was wrong [2], which occurred due to lack of additional means of temperature measurement for correlation. This part of the project (funded by the Infinite Energy Foundation) consisted of reverse-engineering duplication of the geometry and materials of the Lugano “HotCat” reactor and its metallic mounting rack. The objective was to produce a calibration dataset for direct comparison with the reported Lugano measurements [1].

For this calibration, Temperature of the replica reactor was measured using the same Optris PI-160 thermal imaging camera with identical factory calibration (for measurement up to 1500°C), and emissivity selection was implemented exactly as in the Lugano analyses. The calibration was performed with a sweep of electrical heater coil Power input (presumed to be equal to heat output), measured with the same power analyzer (PCE 830) as the system described in

[†]www.quantumheat.org.

*Corresponding author. E-mail: mathieu.valat@gmail.com.

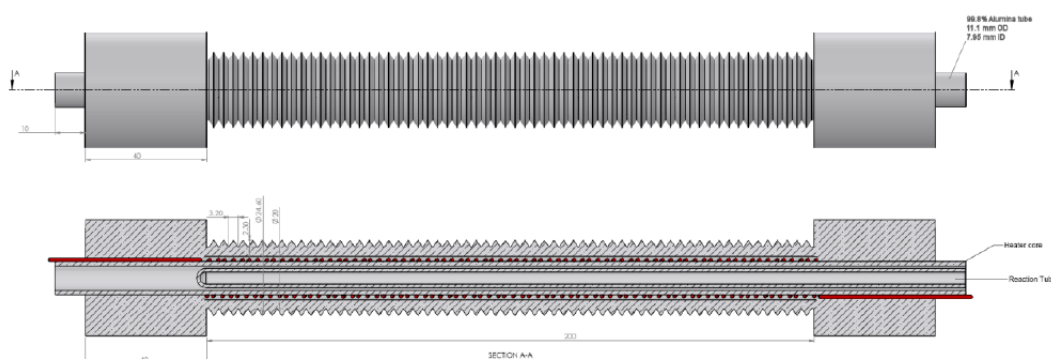


Figure 1. Schematic of the ceramic cell.

the original document. For this calibration, no fuel would be used, so the sole source of heat would be electrical input to the heater coil. The calibration based upon this replica would be used to produce a function, $T_{\text{Lugano}} = f(P)$, that could be used to determine the heats generated in the Lugano experiment by direct comparison, instead of by calculation as was done in the report.

According to instructions in the Optris infrared camera manual, it was necessary to use a high-emissivity black paint on the surface of the alumina reactor to set the emissivity factor of the camera. The high-emissivity paint was provided by Aremco (reference 840-CM) for use in this test.

This experiment used additional means of temperature measurements not used in the Lugano Report. A Williamson infrared Pyrometer (model Pro 91-65-C) and type-B and type-K thermocouples were used to cross check the measurements made by infrared camera. The Williamson pyrometer was a dual-wavelength instrument that self-calibrates for emissivity based on measurement at two adjacent wavelengths. Subsequent to calibration of power, these additional measurements would relate $T_{\text{actual}} = f(T_{\text{Lugano}})$ to get a better idea of the correct temperatures under which the reactor was operated. This temperature mapping is not a part of the extraction of the operating heat in the Lugano experiment, but rather just supplemental information.

The HotCat replica was comprised of alumina ceramic tubing, wound with a single-phase heating coil, and with an over molded triangular fin surface having similar geometry and dimension as the Lugano device. Figure 1 shows the design dimensions. The fins described in the original report were cast over the core tube using a purpose-made two-part mold.

The fins are made with Cotronics RTC-60 castable alumina. Figure 2 shows the two reactors side by side, the Lugano apparatus and MFMP's replica, each on a scale. The weight of the replica is 20 g (4.4%) more than the original Lugano reactor.

Compared to the original experiment, the main variation was the heating element. The maximum design power of 1.9 kW and 1400°C peak temperature was inferred in the Report, but the metallic composition of the heater coil was not described. The MFMP replica (aka “Dogbone”) used Kanthal A1 wire, rated to 1400°C for short intervals. Since the aim of this experiment was not to create excess energy but rather to verify the thermal measurements, only a source of Joule heating was provided. Therefore, no attempt was made to duplicate the triple coil winding and three-phase power used in the Lugano apparatus. While this sounds like a big difference, the close wound heater coil is an internal heat source that can be modeled in either case as a distributed cylindrical sheet of heat emission. The primary vector for heat loss from the apparatus is the finned exterior surface of the central tube. Particularly at lower temperatures, the finned exterior of the reactor can be modeled as having a thermal resistance to ambient and the temperature of the



Figure 2. Photos of the original reactor and its replica.

finned surface is determined by how much heat traverses this path, not by how the power was created. Some error can be attributed to the unknown differences in radiation between the Lugano apparatus and the MFMP replica caused by possibly different temperatures inside the body and possible differences in spectral transparency of the cast alumina. Figure 3 shows the schematics of the heater coil geometry.

Thermal measurements were made up to 900 W power input – commensurate with the power given in the Lugano Report for the first part of that experiment. The thermocouples showed a maximum temperature of 843°C, compare to 975°C given by the Williamson pyrometer and an average of 971°C by the Optris infrared camera with emissivity set to 0.95.

Further measurements showed significant temperature gradient on the tube circumference and along the surface profile of the outer fins. This surface temperature variation, combined with the limited contact patch of the thermocouple beads, was probably the cause of the lower thermocouple readings compared to the pyrometer. Figure 4 shows the thermocouple attachment to the fin structure. The yellow spot was from the pyrometer aiming laser.

While this temperature gradient vertically across the finned central tube would present a problem for attempted calculation of emitted heat, the Optris camera was setup to measure an average from top to bottom and left to right in square regions along the tube. As long as the replications matched the average temperatures recorded by the Optris camera in these regions, a thermal state match between the replica and the Lugano experiment would be assumed.

The team evaluated the calibration setting of the Optris infrared camera on a paint spot with known emissivity. A value of $\varepsilon = 0.95$ was then derived iteratively for the cast material by temperature correlation between the painted spot and the immediate close proximity bare alumina. The Williamson pyrometer confirmed this emissivity within a 2% range. This also agreed with the suggested value in the Optris manual for alumina.

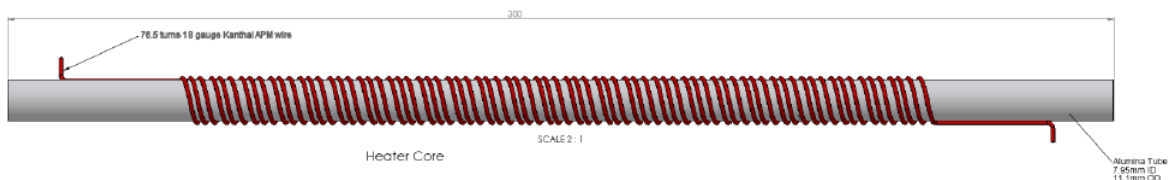


Figure 3. Schematics of the heater coil geometry.

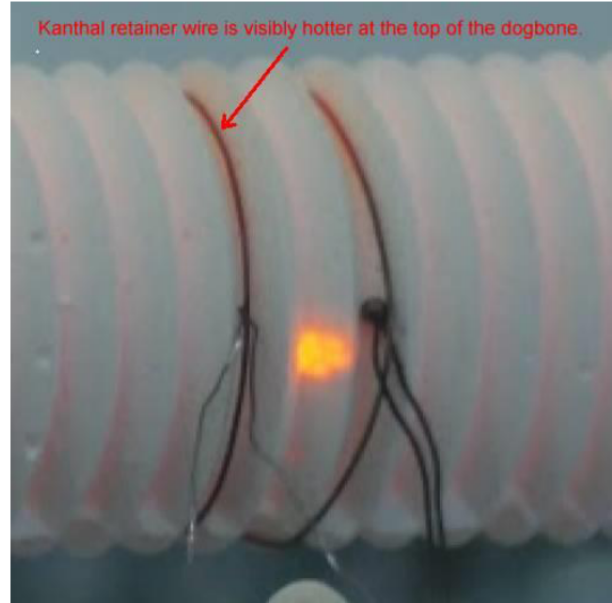


Figure 4. Thermocouple attachment to MFMP replica. Type-B on left, type-K on right.

Since alumina changes transparency in this temperature region [3], the radiant heat emitted by the heater coil through the semi-transparent material would not have had a blackbody spectrum. It would be difficult (perhaps impossible) to determine the actual thermal emission without measurement of the emitted spectrum over an optical band extending from UV to far infrared. This spectral data was not supplied in the Lugano report.

The Lugano report also did not provide $T_{\text{surface}} = f(P)$ calibration data over the entire range of power that was used during the fueled test. So the replication strategy was to create a dummy experiment to acquire the missing $T_{\text{Lugano}} = f(P)$ data to provide a means to extract how much power would have been required to reach each “Lugano thermal state”. By testing with the Optris camera, it was found that if the camera remained set with an emissivity of 0.95 for data gathering, the temperature at any other emissivity could be calculated as

$$T' = T_{0.95} \sqrt[3]{\frac{0.95}{\epsilon'}}.$$

The relation above was verified with a data point taken with the Optris camera having the emissivity manually set to $\epsilon = 0.95$, and then to $\epsilon = 0.45$. Thus, these temperatures were calculated in the same manner as used in Lugano report – iterated for consistency with the emissivity curve [1] (Plot 1) used in the Lugano analyses.

With a means to obtain the thermal state for the MFMP replica in direct correspondence with the Lugano data, the MFMP replica heater input power was swept while Optris thermal data was acquired. This data would provide a means to directly extract the power needed for each of the reported Lugano reaction thermal states, as if the Lugano experiment had first been run with a widely ranging power sweep in its dummy run.

Having such $T = f(P)$ data completely obviates the need for calculation of emitted heat via convection and radiation (which were found likely in error for not having included the alumina’s spectral transparency). For this paper, the swept $T = f(P)$ curve of the MFMP replica was used to directly assess possible excess power in the Lugano experiment.

Unfortunately, while taking readings at 900 W input, the MFMP Optris camera was damaged by an accidental electrical short circuit. Because of this, data for input powers above 900 W are estimated via analytic curve fit extrapolations. These analyses are described in Section 2.

2. Analysis and Interpretation of the Replication Against the Lugano Test

The Lugano experimenters used an average temperature for each zone defined along the length of the ceramic apparatus. To match these values with the MFMP replica, it is necessary to match values of identical zones from both data sets. Using zones 5–9 of each apparatus allowed a very close match of both average and standard deviation values of the original Lugano calibrations. Hence, the average of these zone temperatures is used as a common thermal state to compare the values measured for the MFMP replica to those measured for the Lugano reactor. Figure 5 shows a plot of the MFMP replica data using the average from zone 5 to 9 to calculate the temperature, along with a curve fit for the data, and the corresponding iteratively calculated temperature as would have been recorded by the Lugano researchers for this experiment.

The Lugano experimenters reported their results as “Files” for sample data sets. An example for the first phase of excess heat production is File-4 reactor temperature of 1257.21°C ([1], Table 6), at an input power of 790.69 W ([1], Table 7). Using interpolation in the MFMP replica curve of Fig. 5, direct heater electrical input would have produced this same Lugano thermal state with a power input of 893.6 W. Since the fueled Lugano reactor reached this thermal state with an input of only 790.69 W, an apparent excess heat of 102.9 W is indicated from the reaction. The corresponding “actual” surface temperature for this reaction is estimated as 944°C and the apparent coefficient of performance (COP) is 1.13.

After running the experiment at this input power for 10 days, the Lugano experimenters increased the input power

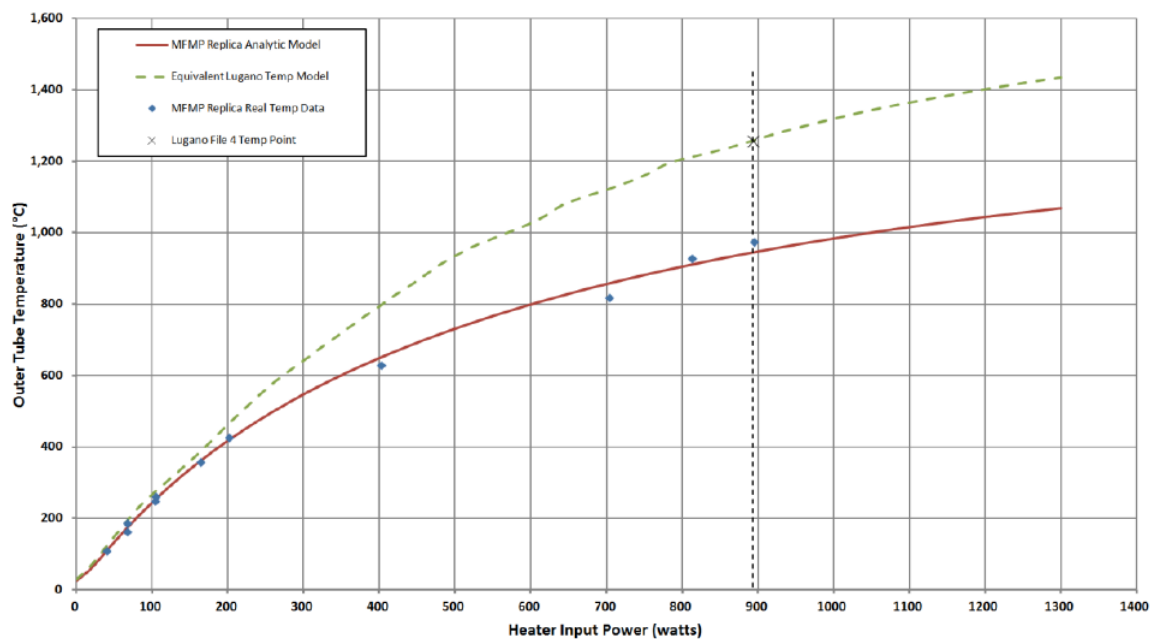


Figure 5. Graphical extrapolation of our measurement.

for a new, higher temperature reaction state. The data from this state was examined in a similar manner. In the Lugano File-8 data, the reactor surface temperature was reported as 1404.04°C using an input heater power of 918.24 W. Using extrapolation with the fitted curve in the MFMP replica, the replica would have reached this Lugano thermal state with a direct heater input of 1208 W. The apparent excess heat is estimated as 289.8 W with an apparent COP of 1.32, at an operating “actual” surface temperature of 1045°C. Complete calculations and original plots are available for public download^a.

Note that the temperatures reported are surface temperatures, and the core temperature is likely 150–200°C hotter. The apparent excess heats, COPs, corresponding “real” temperatures, and excess heat variation with temperature seem commensurate with reports from similar experiments [4,5]; and in the case of A. Parkhomov [4], excess heat was assessed via mass-flow calorimetry.

As an additional correlation, an attempt was made to apply the same analysis to the dummy run data from the Lugano report ([1], Section 5). The Lugano experimenters based the veracity of their analyses upon the dummy run data. With an electrical input of 479 W, the reported average temperature was 442.5°C. Interpolating Fig. 5 MFMP replica data, this Lugano thermal state should have been achieved with a heater input power of only 190.6 W. The dummy run data appears to be truly anomalous. According to the thermal response of the MFMP replica, the 479 W input should have produced an “actual” surface temperature of 715°C and a corresponding iterated Lugano-technique temperature of 914°C. How could the measured Lugano dummy run temperature have been so low? If the Optris temperature measurement was the same as subsequent fueled runs, the input heater power should have been 190.6 W, not 479 W (an error of 251%). If the electrical power for the dummy run was measured accurately, the Optris camera should have measured an iterated Lugano-technique temperature of 909°C instead of 442.5°C. Since the dummy run was conducted before fueling the reactor, the system would have been electrically disassembled, fueled, and then reassembled. It may be speculated that there was a mistake in the original dummy run electrical connection or measurement, that was unknowingly corrected during the reassembly, prior to making subsequent fueled runs.

Additional analyses of the MFMP replica data, as applied to the Lugano results, showed that if the single, hottest zone (8) of the MFMP replica was used as the basis for comparison, instead of the zones 5–9 average of Fig. 5, less excess power is estimated. Hottest zone analysis estimates the lowest excess heats File-4 excess heat of 63.3 W, and File-8 excess heat of 220.8 W.

In summary, based upon analyses using the MFMP replica “Dogbone” data, the Lugano experiment is estimated to have produced at least an order of magnitude lower excess heat than reported. However, excess heat is not ruled out commensurate with that seen by other experimenters using a similar LENR technology [4,5]. Also, the MFMP replica data suggests that an anomalous error occurred during measurement of the Lugano dummy run.

3. Introduction to the Glowstick Experiments

MFMP member, Alan Goldwater, further investigated the thermal behavior of Lugano-like systems. The new Glowstick design retains important features from the Lugano apparatus, but techniques were developed to allow reuse of the reactor over multiple experiments, and to provide a simultaneous experimental control. Several initial tests explored the operational range of power, temperature and refractory materials. A series of incremental experiments further refined the mechanical and control systems, yielding a robust and stable experimental platform built from readily available components, expanding further replications within the community.

^a“Dogbone Analysis of Excess Heat” <http://goo.gl/0rP40x>

4. Description of the Reactor Geometry and Materials

The fifth iteration of the Glowstick design used a mullite ceramic tube as the main reactor body. The fuel was loaded into a stainless steel capsule, then inserted into the reactor body. Figure 6 shows the geometry and dimensions of each element. Both ends of the reactor were tightly sealed on a polished surface of the mullite tube using Swagelok fittings with aluminum compression ferrules. This technique provided connection of the reactor to industry-standard gas and vacuum plumbing, with easy assembly.

The Swagelok sealing technique was repeatable and was proven to be hydrogen-tight at reactor core temperatures up to 1300°C. This was important because vacuum degassing and control of hydrogen pressure were thought to be necessary for loading of hydrogen into nickel, and for subsequent reaction processes.

The fuel was comprised of nickel (Hunter Chemical AH50, particle size $4.5 \approx 1.5 \mu\text{m}$), lithium tetra-hydro-aluminate (henceforth referred to as LAH or LiAlH_4 in formulae) (Sigma Aldrich, CAS 16853-85-3) and micro-encapsulated lithium (Nanoshel, CAS 7439-93-2) mixed under argon atmosphere with a mortar and pestle to reduce the LAH particle size and provide a homogeneous fuel mixture. The fuel mixture was then placed in a stainless steel capsule and closed with a vented set screw. The null capsule was identical to the fueled capsule but filled instead with alumina powder.

The heater element was a single phase coil made of Kanthal A1 wire (18 AWG = 1.02 mm). The coil was divided exactly in half, so that the active and null sides of the cell each receive one half of the applied Joule heating power. Each coil had an alumina cover tube to provide thermal insulation and support for identical type-K thermocouples.

A manifold enabled the inside chamber of the reactor to be vacuumed, vented and pressurized with hydrogen gas. To reduce the dead volume in the reactor chamber, the empty parts were filled with alumina or stainless steel rods. A two-stage vacuum pump (Welch Duo-Seal 1400) with Pirani gauge was used for initial degassing and bake-out of the reactor to 5 Pa or less (at the gauge). The micrometer metering valve was subsequently used to bleed excess hydrogen into a vacuum reservoir.

An alumina felt plug at the center of the reactor was used in an attempt to provide a physical barrier to liquid

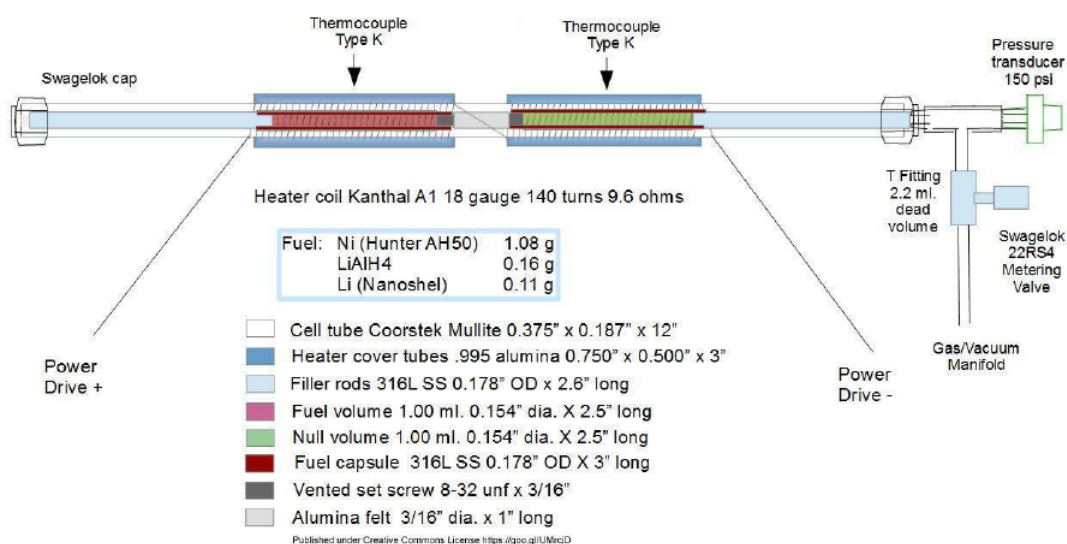


Figure 6. Details on the geometry of the Glowstick GS5 reactor.

lithium migration, while giving sufficient permeability to allow vacuum and hydrogen pressure to reach the active fuel capsule. This showed to be a partially effective barrier.

5. Description of the Control System

A closed loop design allowed the system temperature to be constantly controlled over the duration of the experiment. Control was provided by a PID controller (Dwyer model 16868) with type-K thermocouple in contact with the reactor on the fueled side, and an SCR proportional phase angle power controller (CCI model 1022). The heater power leads were fed through a Tektronix model PA1000 power analyzer, providing RMS power data stored at two samples per second intervals. The PID controller could be programmed for ramp/soak temperature sequence, or bypassed for manual control.

Two thermocouples (type-K) and a Honeywell 0–150 psia pressure sensor were connected to a 16 bit ADC DAQ (HUGnetLab model E) for collection and Internet broadcasting of temperature and pressure data in real-time.

A gamma spectrometer (Spectrum Techniques UCS-30, 38 × 38 mm cylindrical PAXON PX NaI+TI scintillator) monitored gamma radiation coming from the reactor, with a MCA range of ≈ 20 keV–1.5 MeV. The scintillator head was surrounded by ≈ 100 mm of lead on all sides (240 kg) to suppress background. A 50 × 50 mm aperture admitted radiation from the active fuel part of the reactor, over a solid angle of about one steradian. A Geiger-Muller counter (GQ Electronics model GMC-320+) provided cross-check in the 300 keV–3 MeV range.

It is important to note for future replications that the heater power must be transformer isolated from the mains supply. Additionally, a 5 mA triggered GFCI (ground fault circuit interrupter) should be used as shown in Fig. 7, to avoid damage to the DAQ equipment from heater electrical leakage through the hot ceramic reactor assembly. In earlier experiments it was found that at temperatures approaching 1000°C, Glowstick mullite and alumina reactor tubes became electrically conductive. As a result, heater power was causing common mode noise currents in thermocouple

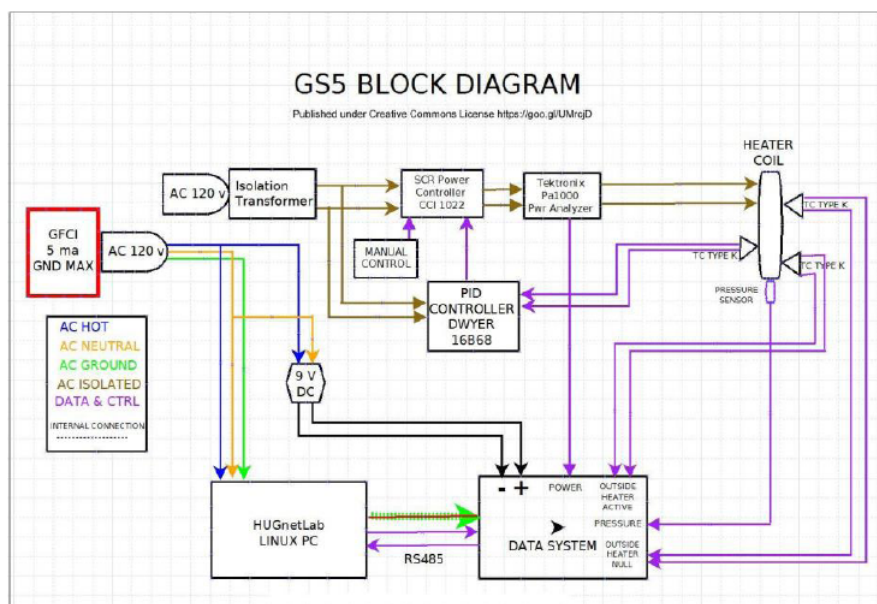


Figure 7. Schematic of the data acquisition and control system.

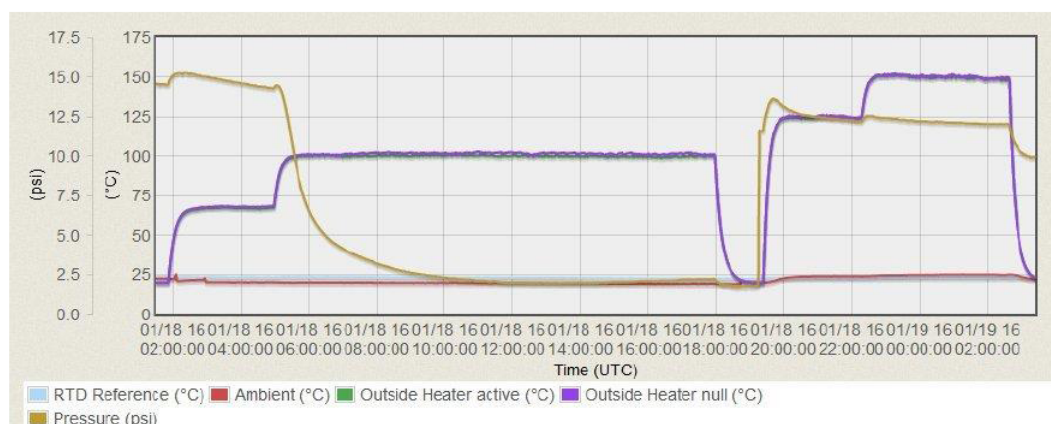


Figure 8. Evidence of hydrogen loading into the fuel.

junctions in contact with the ceramic. Changes to the experimental setup were then made to mitigate the effect of such induced current^b.

6. Pre-processing of the Nickel Powder

The nickel powder was baked before mixing the fuel together. The reasoning was that repeated thermal oxidation and reduction of the Ni particle surface may aid in creating cracks and increased surface area. The resulting micro-scale cavities and lattice flaws are thought essential for deep loading of hydrogen.

Consequently, two cycles of – baking the nickel powder at 200°C in a furnace were applied, followed by heating under continuous vacuum at 115°C for several hours to remove trace water vapor that might be adsorbed by the nickel and other cell contents.

A separate test run prior to adding other fuel components was done to evaluate loading of hydrogen following pre-processing. For this test, the baked nickel powder alone was placed in a stainless steel fuel capsule and installed in the reactor. After sealing, the reactor was evacuated and hydrogen was added from a gas cylinder to 1 bar absolute pressure.

As shown in in Fig. 8, the cell pressure (yellow trace) declined from 1 to 0.2 bar during five hours at just over the 100°C set point, corresponding to about 120°C in the fuel capsule.

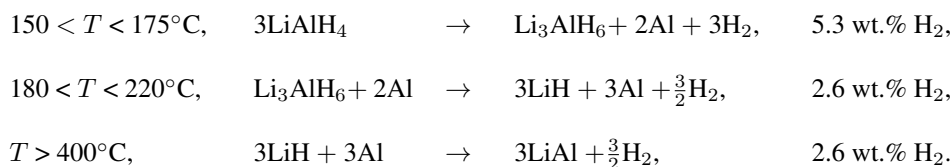
Following the loading test, the fuel capsule was removed from the reactor, sealed with tape and stored in ambient air for several days. The capsule was then placed in a glove bag along with other fuel components. The nickel was removed from the capsule under Argon cover gas and mixed with the other ingredients before loading back into the fuel capsule.

7. On LAH Breakdown and Interactions with Nickel

Because variations of hydrogen pressure is an important experimental evidence to support adsorption/absorption of hydrogen inside the metal lattice, it is proposed to recall some mainstream reference first, to draw the picture of LAH breakdown during the course of our experiments.

^b“Glowstick Thermocouple Ground Leakage” <http://goo.gl/V8gz6c>

Andreasen et al. [6] detail the first states of dehydrogenation of this compound as follow.



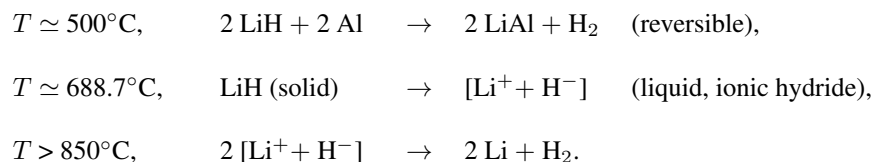
The first steps are interesting because it enables hydrogen exposure of nickel powder around its Debye temperature. Wiench et al. [7] showed evidence of multiple pathways during the thermal decomposition of the LAH compound using MAS and MNR spectroscopy, including the following.



Jain et al. [8] expanded his reviews to multiple complex hydride compounds and provided additional evidence to the diversity of breakdown paths these hydrides are able to follow.

Most of the studies were done for the purpose of hydrogen storage technology, hence limiting temperature range to 400°C . However Lin et al. [9] calculated from experimental evidence the solubility of hydrogen in lithium aluminum compounds up to 1200 K, showing a high value of solubility, increasing as lithium content increases.

Interesting behavior has been ascribed to the interaction of the electronic shells of nickel and hydrogen anions (H^-), also called protide. Descriptions of the involvement of this less common state of hydrogen are provided in these publications [10,11].



While very little is available in the literature on this particular state of hydrogen, it is interesting to observe that liquid LiH is an ionic hydride and the hydrogen exists in solution as hydrogen anions. In addition, Kasagi et al. [12] showed cross section capture of low energy proton or deuterons on lithium is greater when Lithium is in a dense ionic state.

Scanning Electron Micrographs (SEMs) and corresponding EDS-X analyses provided by Edmund Storms from Kiva-Labs and Sangho Bok from University of Missouri aided in understanding the behavior of this chemical system at high temperature. Note the similarity of the micrograph of Fig. 9 to the one of the ash produced for the Lugano report ([1], Appendix 3, Fig. 2). Figure 9 suggests that, once molten, the Li–Al–H alloy wets to the oxide-free Ni powder.

However, the surface of the spiky Mond process Ni particles (obtained from nickel tetracarbonyl) is complex on both the micro-scale and the nano-scale. In some places the molten Li–Al–H (an ionic hydride) may be in direct contact with the Ni surface. In other places, due to the surface tension of the liquid metal, surface complexity may be “skinned over”, leaving micro-scale and nano-scale voids. If the Ni+LAH system proves to be LENR active, this

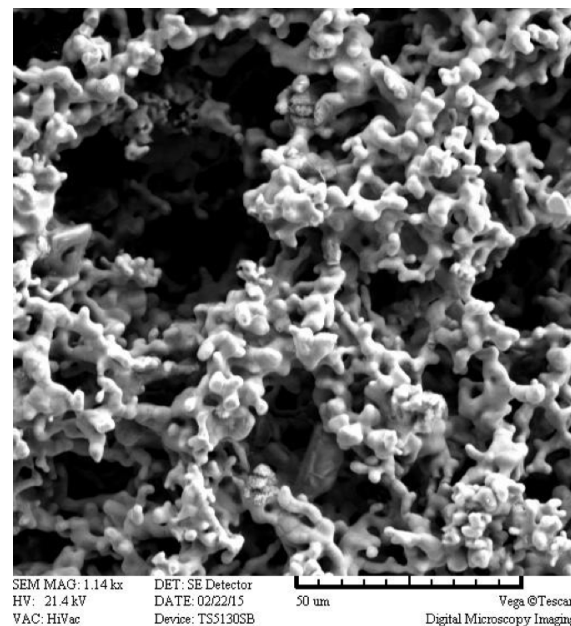


Figure 9. SEM picture of the powder wetted by the LAH after high temperature migration (courtesy of Kiva-Labs).

Li–Al–H ionic hydride interface to the Ni should be the subject of extended study. References possibly pertinent to such a study have been included [13–15].

8. Operating Parameters

After the experimental setup was assembled and all instruments connected and calibrated, the reactor tube was vacuumed for two hours and left overnight. Temperature was increased to just over 100°C. The partial dissociation of the LAH compound slowly produced an increase of pressure. The flux of hydrogen generated by this increase of temperature would have reduced any remaining nickel oxides, leaving a clean surface on the metal particles. Further vacuum to under 100 Pa absolute pressure was then applied to remove resulting trace water vapor.

The in-situ oxide removal was followed by raising the core temperature to 122°C, deliberately below the lowest known Debye temperature (132.85°C) [16] of nickel where it was held for over 6 h before raising the temperature to comfortably below the nickel Curie temperature (358°C). During this entire period hydrogen evolved from the LAH, so a bleeder valve was adjusted manually to keep the reactor pressure at 1 bar or less.

Next, the reactor core was slowly cooled down to a temperature comfortably above the maximum Debye temperature of nickel (204°C). Afterward, the temperature was quickly increased to 400°C (above the nickel Curie temperature).

Following an extended dwell to allow completion of the first phase of LAH decomposition, the temperature was increased in several steps to $\simeq 700^\circ\text{C}$, where additional phase change was expected to occur. A further increase to above 900°C put the LAH into a state of reversible release of hydrogen.

After additional dwell time to watch pressure behavior, thermal cycling was started, alternating between 600 and 1000 W RMS input (yielding from $\simeq 900^\circ\text{C}$ to $\simeq 1200^\circ\text{C}$) at 30 min intervals, and continuing for several hours. During this period, an apparent increase in temperature differential between the active and control sections to $\simeq 50^\circ\text{C}$ was

observed as shown in Fig. 10. Compared against calibrations, the power difference was assessed to about 70 W greater heat from the fueled section, corresponding to a COP of 1.09. This COP is small, and when compared to possible thermocouple aging and other sources of measurement error, may prove to be borderline for a claim of excess heat.

9. Radiation Measurements and Analysis

As previously mentioned, this experiment was monitored with an NaI-Tl scintillator attached to a UCS-30 spectrometer with the scintillator placed 33 cm away from the fuel and shielded within a lead cave. Integrations were started manually back-to-back, but over somewhat irregular period lengths. Overall, 24 integrations were made over the course of the experiment from cold reactor to cold reactor. During one 4-hour integration period highlighted in Fig. 10 as “Spectrum 7”), a broadband X-ray/gamma emission (10–400 keV) was recorded.

The curve shape of Spectrum 7 was consistent with Bremsstrahlung radiation as shown in Fig. 11. This spectrum is the longest of the series (a 4 h integration). The signal captured has nearly an order of magnitude amplitude above average levels seen in the other spectra.

Figure 12 shows a photometric background spectrum that was extracted from Spectrum 1 and Spectrum 24 ; cases where no reaction should be present.

When the background spectrum of Fig. 12 is applied to Spectrum 6, a case also expected to be null, the residual shown in Fig. 13 is obtained. As can be seen in this linear plot, the residual is zero mean over the bulk of the valid spectrum. The noise increase seen below 200 keV is due to the Poisson noise characteristic of a random source (similar to noise in astronomical photometry), wherein the noise increases as the square root of signal strength.

Photometric reduction of the actual data comprised energy resampling of the source data spectrum to a calibrated 1 keV per sample energy scale, and subtraction of a background scaled by the total length of live time of the source spectrum data.

Figure 14 shows the radiation signal spectrum for Spectrum 7 with photometric calibration.

This data was intensely analyzed by the crowd (internet observers), to see if it could be an artifact of measurement error or contamination. Possibilities including a cosmic ray burst, radon concentration and radio-frequency interference were proposed, tested and disproved. Figure 15 shows the results of radon investigation.

Replication and further experimental evidence is necessary with complementary equipment to define the origin of this signal. The complete analysis is available for further study [17].

No radiation signal above background was detected by the GMC320+ Geiger-Muller counter during this time.

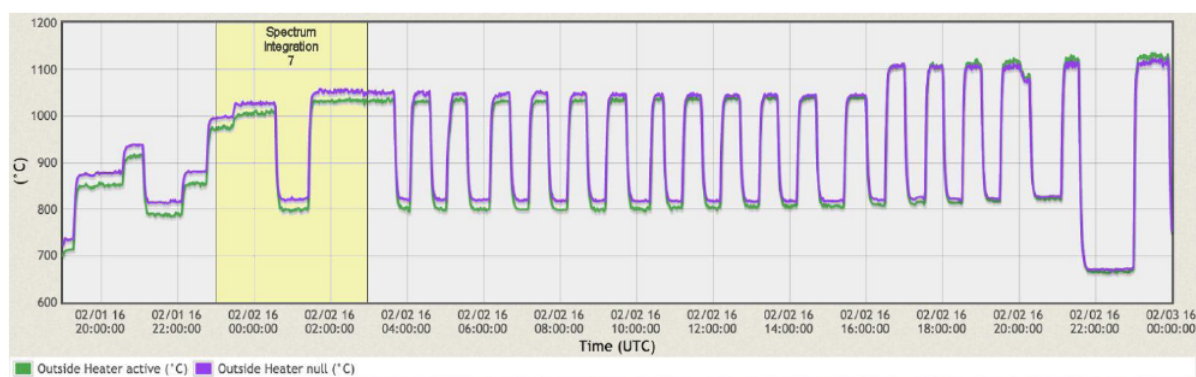


Figure 10. Increase of temperature on the fueled side.

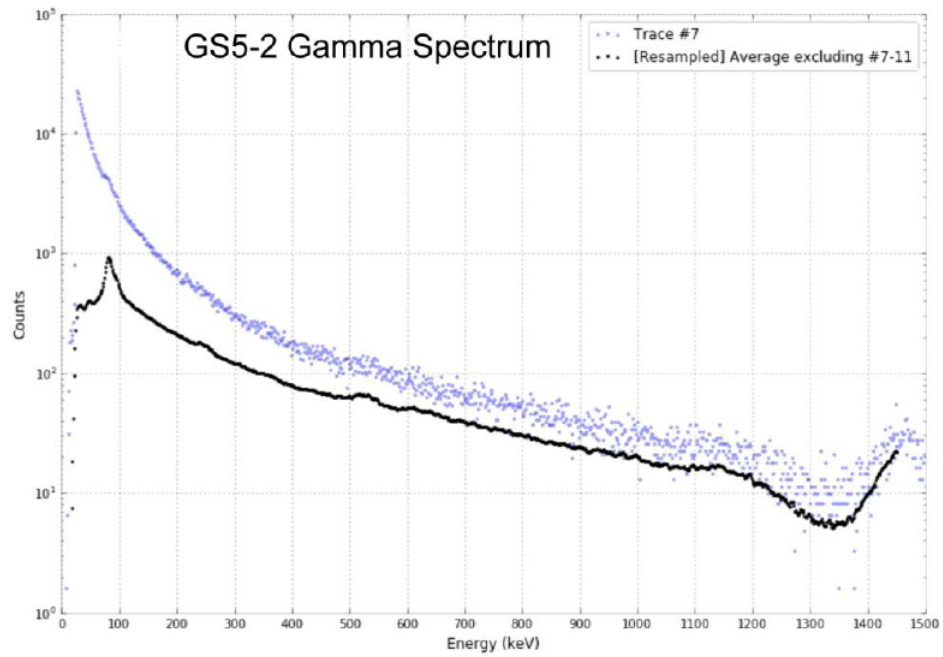


Figure 11. Gamma radiation at the beginning of the anomalous heat period compared to normalized background.

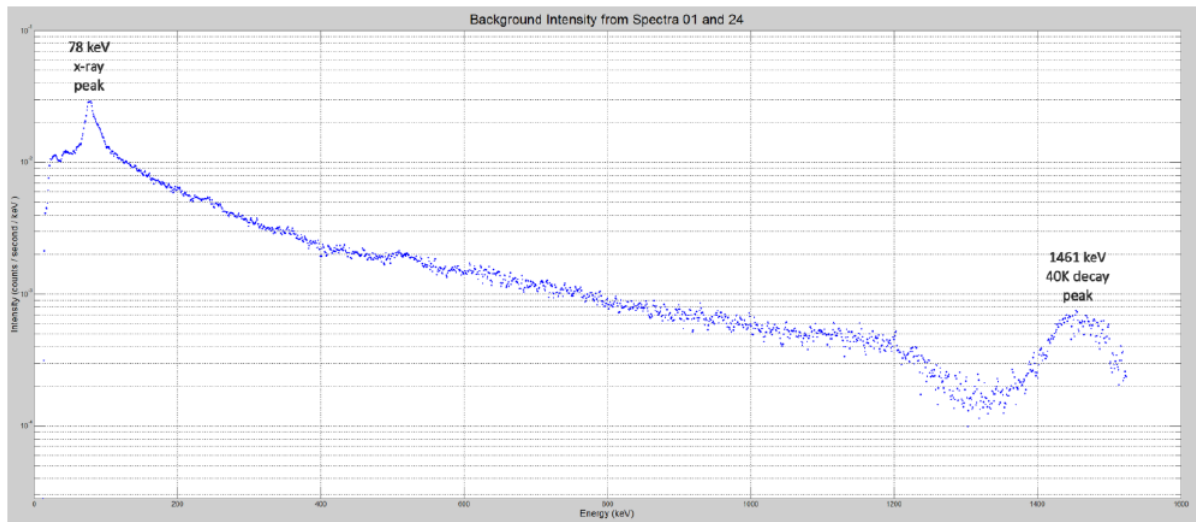


Figure 12. Photometrically calibrated background spectrum.

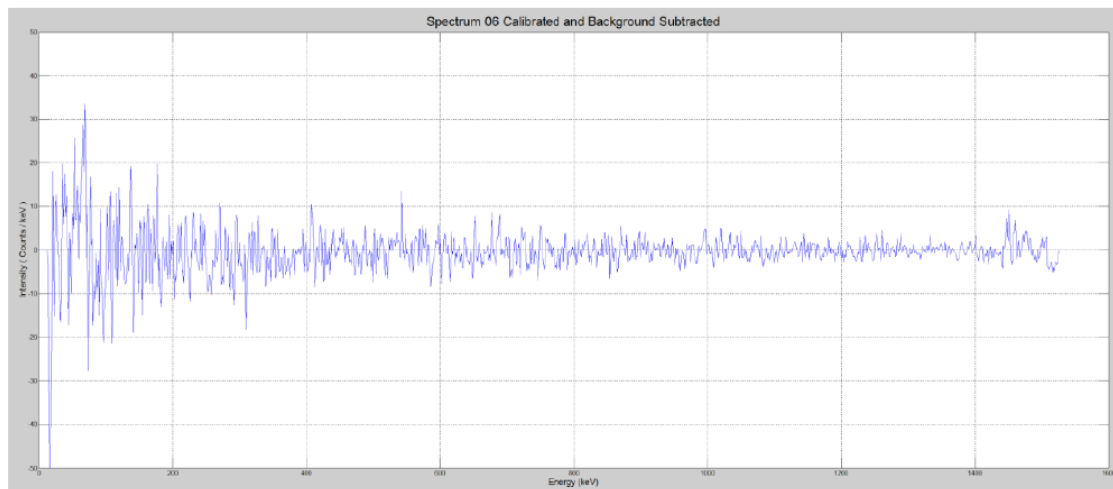


Figure 13. Null Spectrum #06 residual from background subtraction.

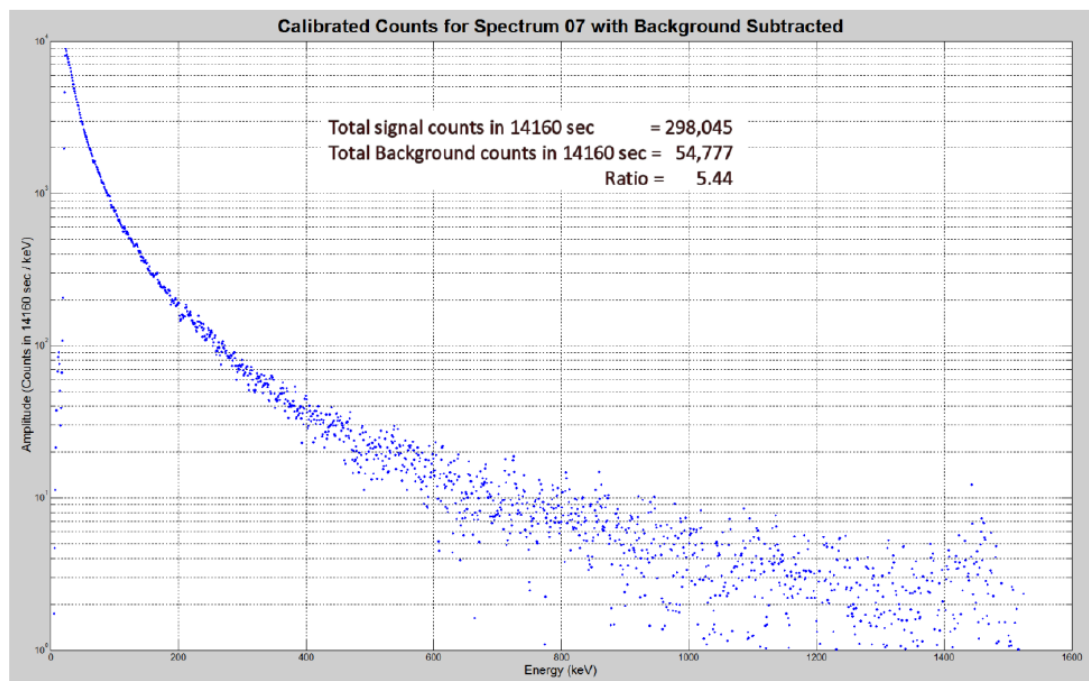


Figure 14. Calibrated counts for the broad-band Spectrum #07 signal with subtracted background.

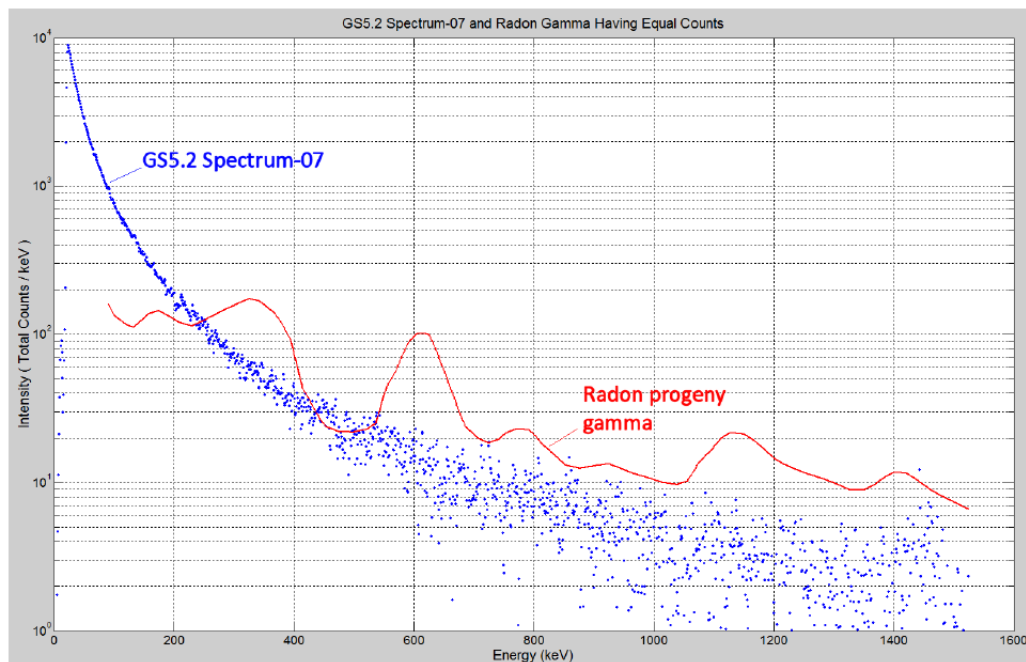


Figure 15. Broadband spectrum compared to typical radon spectrum.

It should be noted that this is an inexpensive instrument with poor sensitivity, especially to low-energy (<100 keV) gamma radiation. Post experiment testing of the GMC320+ and modeling with the spectrum detected by the scintillator suggested the GMC320+ should only have seen a small number of counts above background. Depending upon the unknown time spread of the scintillator detected signal (up to 4 h), this may not have been discernable above the background counts in the GMC320+.

10. Conclusion

With a diligent scientific study of claims made for Rossi's HotCat reactor, the MFMP team has provided evidence of an overestimation of the results in the Lugano report.

The incorrect setting of the emissivity parameter by a large margin shows how the Lugano team overestimated the thermal output of the HotCat reactor in analyses subsequent to the Lugano test. However, the added MFMP replica data and its co-analysis with the Lugano data cannot disprove a smaller effect, as interpolated/extrapolated in this paper.

Using the Glowstick reactor in its 5.2 iteration, MFMP showed in Live Open Science, that a small amount of excess thermal energy and a gamma photon spectrum were generated by a system using heated nickel, lithium and hydrogen. Additional iterations are being developed by the MFMP group to provide improved evidence of results and increased performance.

The lack of information disclosed by Leonardo Corporation make the replication task difficult. However, MFMP has gathered enough know-how and data from public domain reports to search for evidence of a genuine effect. Even though the nature of the phenomenon is still open to debate, the results compel additional efforts.

From an industrialist point of view, the (currently) small effect provides little hope for short term commercial emergence of this new phenomenon. However, this rather small effect should be a priority for public scientific investigation. It is important to assess the nature of the phenomenon and determine its possible future impact to the world's energy portfolio.

Acknowledgements

This work is dedicated in memoriam to Pr. Martin Fleischmann. It has been enabled by the generous financial, workforce and support help that was provided over the years by the contributors of the Martin Fleischmann Memorial Project. We offer them our best thanks.

All figures are published with permission under Creative Commons License.

References

- [1] G. Levi, F. Evelyn, H. Bo, P. Roland, T. Lars and E. Hanno, Observation of abundant heat production from a reactor device and of isotopic changes in the fuel, <http://ecat.com/wp-content/uploads/2014/10/ECAT-test-report-2014.pdf>, October 2014.
- [2] Bob Higgins, Making sense of alumina spectral emissivity (2015). Download link <http://goo.gl/a91xbm>.
- [3] O. Rozenbaum et al., A spectroscopic method to measure the spectral emissivity of semi-transparent materials up to high temperature, *Rev. Sci. Instr.* **70**(10) (1999) 4020–4025.
- [4] A.G. Parkhomov, Long- term tests of the nickel – hydrogen reactor with flow calorimeter, in *the proc. 23rd Russian Conf. on Cold Nuclear Transmutation of Chemical Elements and Ball Lightning* (2016), submitted.
- [5] Zhang Hang, Test of abnormal heat in hydrogen loaded metal – Report 2 (2016). Download link <http://goo.gl/VjXaNf>.
- [6] A. Andreasen, T. Vegge and Allan Schröder Pedersen, Dehydrogenation kinetics of as-received and ball-milled LiAlH₄, *J. Solid State Chem.* **178**(12) (2005) 3672–3678.
- [7] J.W. Wiench, V.P. Balema, V.K. Pecharsky and M. Pruskia, Solid-state ²⁷Al NMR investigation of thermal decomposition of LiAlH₄, *J. Solid State Chem.* **177**(3) (2004) 648–653.
- [8] I.P. Jain, Pragma Jain and Ankur Jain, Novel hydrogen storage materials a review of lightweight complex hydrides, *J. Alloys Compounds* **503**(2) (2010) 303–339.
- [9] R.Y. Lin and M. Hoch, The solubility of hydrogen in molten aluminum alloys, *Metallurgical Trans. A* **20**(9) (1989) 1785–1791.
- [10] Z.P. Li, B.H. Liu, K. Arai, N. Morigazaki and S. Suda, Protide compounds in hydrogen storage systems, *J. Alloys Compounds* **356** (2003) 469–474.
- [11] Çakanyıldırım, Çetin, and Metin Gürü, Hydrogen cycle with sodium borohydride, *Int. J. Hydrogen Energy* **33**(17) (2008) 4634–4639.
- [12] J. Kasagi and H. Yonemura, Ionic Debye screening in dense liquid plasmas observed for Li+ p, d reactions with liquid Li target, *Nucl. Phys. Rev.* **26** (Suppl) (2009) 44–48.
- [13] S. Focardi, R. Habel and F. Piantelli, Anomalous heat production in Ni–H systems, *Il Nuovo Cimento A* (1971–1996) **107**(1) (1994) 163–167.
- [14] E.G. Campari, S. Focardi, V. Gabbani, V. Montalbano, F. Piantelli and S. Veronesi, Overview of H–Ni systems old experiments and new setup, *5th Asti Workshop on Anomalies in Hydrogen/Deuterium loaded Metals* (2004).
- [15] J.J. Dufour, X.J.C. Dufour and J.D. Vinko, Pico-chemistry the possibility of new phases in some hydrogen/metal systems, *Int. J. Modern Phys. B* **27**(15) (2013) 1362038.
- [16] Yu M. Kagan and I.S. Lyubutin, *Applications of the Mössbauer Effect Applications in other Fields*, Vol. 5, CRC Press, Tokyo, 1985, p. 1394.
- [17] Bob Higgins, Iceberg in the Glowstick 5.2 Data (2016). Download link <http://goo.gl/DOiXYe>.